Thermo-Economic Analysis of Gas Turbine Power Plants Hybridization Using PTSC Technology

THERMO-ECONOMIC ANALYSIS OF GAS TURBINE POWER PLANTS HYBRIDIZATION USING PTSC TECHNOLOGY

by

Muad Mohamed Elgriw

A Thesis presented to the Faculty of the
American University of Sharjah
College of Engineering
In Partial Fulfillment
of the Requirements
for the Degree of

Master of Science in
Mechanical Engineering

Sharjah, United Arab Emirates

July 2020

Declaration of Authorship

I declare that this thesis is my own work and, to the best of my knowledge and belief, it does not contain material published or written by a third party, except where permission has been obtained and/or appropriately cited through full and accurate referencing.

Signed: Muad Mohamed Elgriw

Date: 15/07/2020

Approval Signatures

We, the undersigned, approve the master's Thesis of Muad Mohamed M Elgriw.

Thesis Title: Thermo-Economic Analysis of Gas Turbine Power Plants Hybridization Using PTSC Technology.

Date of defence: 15th of July 2020

Name, Title and Affiliation	Signature
Dr. Mohamed Gadalla Professor, Department of Mechanical Engineering Thesis Advisor	
Dr. Mohammad Omar Hamdan Associate Professor, Department of Mechanical Engineering Thesis Committee Member	
Dr. Zarook Shareefdeen Professor, Department of Chemical Engineering Thesis Committee Member	
Dr. Mamoun F. Abdel-Hafez Head, Department of Mechanical Engineering	
Dr. Lotfi Romdhane Associate Dean for Graduate Studies and Research College of Engineering	
Dr. Sirin Tekinay Dean, College of Engineering	
Dr. Mohamed El-Tarhuni Vice Provost for Graduate Studies Office of Graduate Studies	

Acknowledgement

Firstly, I would like to express the deepest appreciation to my advisor Dr. Mohamed Gadalla for his ongoing patience, support, guidance, encouragement and motivation throughout my research stages and during my thesis completion. I'm immensely grateful for his valuable discussions, suggestions, and assistance during my proposal period.

Secondly, I would like to express my gratitude to the American university of Sharjah for providing me with a research environment and for their unwavering support throughout the research procedure.

Finally, I am grateful for being provided with a Graduate Teaching Assistant offer to complete my Master of science program.

Dedication

I would like to thank my parents for their unlimited sacrifice and support to help me reach this stage. Also, I would like to thank my brother and sister who encouraged and supported me during these stages. To my Uncles, who continue to believe in me and support me every step of the way. To my grandparents, for their infinite Duaa and love. To my friends, who always provided me with happiness and guidance. At last but not least, I would like to dedicate this thesis to my brother's pure spirit who passed away.

Abstract

The effects of environmental change due to ozone depleting waste products are amongst the critical issues facing humanity. Therefore, searching for feasible and naturally well-disposed methods for producing electricity is vital. Among the increasing alternatives available is the concentrated solar power (CSP) which includes the use of parabolic trough solar collector (PTSC) technology. Nevertheless, conventional CSP plants that are based on stream-turbine cycles, which consume large amounts of water, are not preferable in the gulf region. In order to increase the efficiency of the cycle and still maintain a low water consumption, Air bottoming Hybrid gas turbine (ABHGT) is used as an alternative to the recovery of the waste heat with steam-turbines. This thesis will focus on Energy analysis of gas turbine power plants hybridization using PTSC technology. Thermo-economic and environmental analyses are done to four models to illustrate the optimum parameters and performance of power plants. The sensitivity analysis is applied to the ABHGT power plant to study its economic value and indicate the most sensitive parameters that have a dominant effect on the economic analysis. ABHGT running with LPG is analyzed at the sensitivity analysis. Although the natural gas is cheaper than LPG, it is not recommended to be used in the upcoming years due to the depletion effect. The levelized cost of electricity (LCOE) of ABHGT at an optimal annual solar share of 22% is 58.35 (USD/MWh) whereas the LCOE of HGT at an optimal annual solar share of 22% is 65.37(USD/MWh). Reducing the CO_2 emissions is one of the main objectives in the current thesis. An advanced adiabatic CAES is integrated with power plants to enhance the annual optimal solar share with reasonable LCOE. The Performance of Air bottoming Hybrid gas turbine with advanced adiabatic compressed air energy storage (CAES_ABHGT) is evaluated at 1, 3 and 7.5 hours of storage capacity. Thus, it can be seen that Mode C with a 7.5 hour storage capacity is the most promising model since it has the highest optimal annual solar share of 87% with reasonable LCOE of 94.5(USD/MWh) and a reduction of CO_2 emissions by 83%.

Keywords: Air bottoming cycle, solar power, hybridization, CSP, LCOE, PTSC.

Table of Contents

List of Figures

List of Tables

Nomenclature

List of Abbreviations

A	Surface Area
ABC	Air bottoming cycle
ABHGT	Air-based bottoming cycle of hybrid gas turbine power plant
AHX	Air heat exchanger
Am	Air mass
C	Specific heat capacity
C	Cost
CAES	Compressed Air Energy Storage
CAES_ABHGT	Air-based bottoming cycle of hybrid gas turbine power plant with advanced adiabatic compressed air energy storage.
CAES_HGT	Simple hybrid gas turbine power plant with advanced adiabatic compressed air energy storage.
C-C	Combined cycle
CCC	Conventional combined cycle
C_p	Isobaric specific heat capacity
CSP	Concentrated Solar Power
DNI	Direct Normal Irradiance
DNR	Direct normal radiation
E	Electrical power
f_{C02}	Specific carbon dioxide emission content
f_{H2O}	Specific water consumption content
f_{solar}	Specific solar share content
GBC	Gas bottoming cycle
GTIT	Gas turbine inlet temperature
h	Enthalpy
H	Hight
HGT	Simple hybrid gas turbine power plant
HP	High Pressure
HR	Heat waste Recovery

I	Flux intensity
IC	Intercooler
ISO	International Standard Organization
LCOE	Levelized cost of electricity
LCOEN	Levelized cost of energy
$\dot{m}_{air}$	Air mass flow rate
MOEA	Multi Objective Evolutionary Algorithm
MOP	Multi Objective Problem
NDS	Non-Dominant set
N_{PTSC}	Number of parabolic trough Units
NPV	Net Present Value
NREL	National Renewable Energy Laboratory
POF	Pareto Optimal Front
PTSC	Parabolic trough solar collector
PV	Photovoltaic
QMOO	Queuing Multi Objective Optimizer
R	Gas constant
RC	Recuperator
S	Enthalpy
SEG	Solar electric generating system
SGT	Siemens Gas Turbine
t	Thickness
T	Temperature
TES	Thermal Energy storage
U	Overall heat transfer rate
USD	US Dollar
X	Exergy

List of Symbols and Greek letters

i	interest rate
Δ	Change
ε	Heat exchanger of the material effectiveness
η	Efficiency
ξ	Void of air fraction
ρ	Density
μ	Dynamic viscosity
δ	Angle of deflection
γ	Heat capacity ratio
α	Capital recovery factor
Δhi^{0}	Lower heating value
Δk^{0}	Exergy content
θ_s	Solar elevation angle
θ_z	Solar zenith angle
θ	Incident angle [
α_s	Solar altitude angle
ΔP	Pressure drop
ΔR	Radial increment
ΔT	Temperature difference

Chapter 1. Introduction

1.1. Overview

Access to energy is presently like never before at the core of basic monetary, natural, and social issues confronting the world. On one perspective, world development and the high request of developing countries to extend their energy resources lead to an inescapable energy demand. On another perspective, 61 percent of green gases come from energy generating processes, making the energy sector the biggest contributing factor to environmental change [1]. Moreover, rising concerns of shortage of non-renewable energy sources, land acidification, and urban air contamination pose real issues. Therefore, the look for a sustainable, feasible and clean well-disposed supply of energy illustrate vital challenges to humanity. Hence, the advancement of finding other solutions for electrical energy is essentially significant. Solar power production stands out amongst the most encouraging alternatives for various nations with adequate insolation and distinctive innovations that use solar radiation into generating power and is considered as a development in technology. In spite of the current quick falls in the cost of photovoltaics (PV), concentrated solar power (CSP) stands out amongst the greatest alternatives and innovative solutions [11]. Despite the present rivalry between the two advancements, it is likely that they will contribute together to the future worldwide energy production [2].

The real promising advantage of CSP lies in the dispatchability and stability of power generation which was made conceivable by the incorporation of fuel-solar hybridization with storage systems. Hybridization is a short term objective technology that uses solar energy coupled with other sources of energy such as methane (Ch_4) which reduce the green gases emitted to the environment. CSP has a lower environmental impact in comparison to other sustainable power source technologies [3]. In addition to that, CSP has a low cost of power production and can be accomplished particularly when introduced in high-temperature zones. Desert areas such as UAE contain large available areas that are continuously exposed to potentially useful sunrays. However, since there little to no rain, installing conventional CSP plants based on steam-turbine cycles will not be efficient since steam turbines require a lot of water for many purposes such as cleaning of mirror surfaces, cooling of the condensers and replacement of powerplant cycles.

Thus, new ideas must be explored keeping in mind the end goal to find a solution for the reliance on water in future CSP plants [4]. The advancement of high temperature parabolic trough solar collectors paves the way for the utilization of gas-turbines with -natural gas hybrid configurations leading to a decrease in reliance of water and the usage of air as working fluid. Nevertheless, in order to compensate for the high cost of solar hardware and the utilization of natural gas, the heat provided by the topping gas-turbine cycle is reused through the heat exchanger to generate more electricity by the bottoming cycle [5]. The conventional combined cycle configuration with steam-turbines must be avoided to limit the water utilization and alternative arrangements of powerplant cycles need to be explored [6]. One promising solution is to utilize air-based bottoming cycle of hybrid gas turbine power plant (ABHGT) to recover the waste heat. Thermo-economic analysis of gas turbine power plants hybridization using PTSC technology is performed on this thesis [1].

1.2. Thesis Objectives

The focus of this master thesis is placed on the thermo-economic analysis of gas turbine power plants hybridization using PTSC technology. Thermodynamic performance, economic and environmental analysis are done for four models. Therefore, all these aspects need to be taken into consideration to create environmentally friendly energy.

1.3. Research Contribution

The global energy system, responsible for most of the greenhouse gases emissions, is therefore at the heart of global concerns. In particular, the search for a reliable, sustainable and environmentally friendly means of generating electricity is a crucial matter with the growing worries of the scarcity of fossil resources, air pollution and water acidification. For these reasons, the research contributes to overcome the energy problem through using PTSC technology and save as much natural resources as possible. The expected outcome considers thermodynamic performance with an optimum power output in ABHGT, higher efficiency, economic viability, and lower environmental impact. ABHGT fuel such as Ch4 and liquefied petroleum gas (LPG) will be illustrated at the sensitivity analysis.

1.4. Thesis Organization

The thesis is structured to chapters, sections and sub-sections. Chapter 1 discusses the introduction, thesis objective and research contribution. Chapter 2 provides background about solar energy and concentrated solar power technology. Moreover, literature review about using solar technology in UAE and a couple of old power plant configurations is discussed. Chapter 3 discusses the methodology and the mathematical model of the system. Chapter 4 presents the steady state and transient results coupled with thermo economic optimisation. Lastly but not least, Chapter 5 concludes the thesis and outlines the recommended future work.

Chapter 2. Background and Literature Review

2.1. Sun Energy

The advantage of the Sun energy is illustrated in this section 2.1.1, while the solar radiation and its theoretical are presented in sections 2.1.2 and 2.1.3. In addition**,** Selection criteria of CSP projects based on the geographical location is illustrated in section 2.1.4.

2.1.1. Solar energy. The energy obtainable on Earth is provided from a lot of different sources. Over 99.9% of this obtainable energy is provided by the Sun. As shown in Figure 1, the mean solar flux reaching the Earth´s atmosphere is approximately around 170’200 (TW), but only 10.3 (TW) obtained from geothermal energy and about 3.2 (TW) are obtained by gravitational energy. On the other hand, only 47% of the mean solar flux is accessible at the Earth´s surface (80’000 TW). The atmosphere will either reflect or absorb the rest.

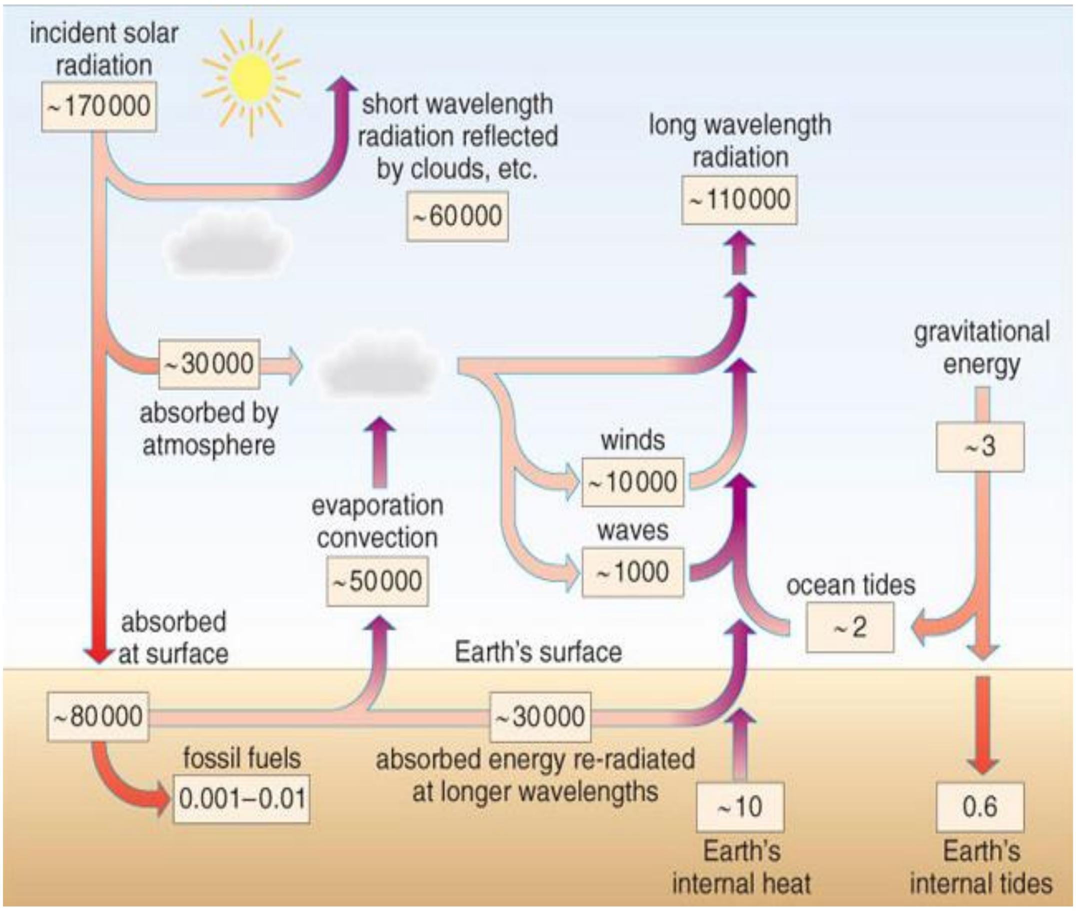

Figure 1: Earth's Natural Energy Systems and power exchange (TW) [1]

The world's Total Primary Energy Supply (TPES) was 12'029 Mtoe in 2007 [2]. Which in turn is equivalent to a continuous power consumption of 16.0 TW. The mean solar power accessible at Earth's surface therefor exceeds by 6'000 times our basic energy needs. Although, this information suggests the abundance of solar energy, it must be regarded carefully as energy supply and demand are depending on time and location and their matching remains an ongoing challenge. Solar radiation particularly is a predominant intermittent source of energy and its conversion into electrical power can only be done under confined conditions [3].

2.1.2. Solar radiation. The emitted flux by the sun is defined as Solar radiation, provided by internal fusion reactions. The Sun is a spherical shape that contains hot gaseous matter (hydrogen and helium mostly) with an average distance from Earth Lf_s and a diameter ds [6]:

$$Lf_s = 1.495 \times 10^{11}\ [m] = 1[UA] \quad and \quad d_s = 1.39 \times 10^{9}\ \ [m] \tag{1}$$

The structure of the sun is not homogeneous. Whereas the suns core is the hottest, most dense region. The photosphere, regarded as the solar surface, is the source of most of the solar radiation and has a temperature that's varies from 6'600 K (bottom) to 4'400 K (top). The black body effective temperature is about T_s = 5778 $[K]$ (the temperature of a blackbody is approximately equal to the sun temperature) [4].
"The intensity of solar radiation is defined as the energy from the Sun per unit of time received on a unit area perpendicular to the direction of solar beam" [1]. The radiation amount decreases with the double of the distance travelled (heat losses are not considered). The intensity of solar at distance of 1 UA from the Sun, it is also recognized as the solar constant Gsc, expressed by [5]:

$$G_{sc} = \frac{I_s \pi {d_s}^2}{\pi(2I_{es})^2} = 1376 \qquad [\frac{W}{m^2}] \tag{2}$$

The average radiant flux of the Sun I_s =63.5∗106 $[Wm2/]$ obtained from the Boltzmann's law of Sun potent blackbody temperature T_s.

Due to the Earth's orbit being slightly eccentric, the Sun-Earth distance variation is about 2% during the year. This leads to alterations of exoatmospheric radiation G_{on} "(radiation incident on a plane normal to the radiation outside the atmosphere) in the range of ±3.3%" [1]. An approximate resembling expression for G_{on} is illustrated by [4]:

$$\mathrm{G_{on}}\mathrm{G_{on}} = \left(1 + 0.33\cos\left(\frac{360\mathrm{n}}{365}\right)\right) \tag{3}$$

where n is the number of days. The alterations of $\mathrm{G_{on}}$ across the year is illustrated in Figure 2. The minimum $\mathrm{G_{on}}$ is in July whereas the maximum is in January [2].

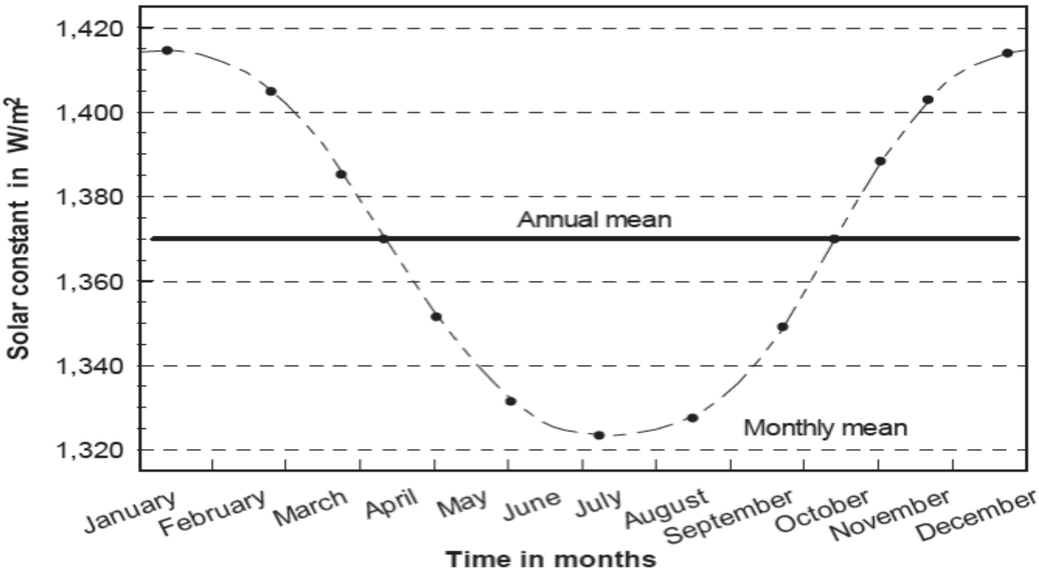

Figure 2: Exoatmospheric radiation change during the time of year [2]

2.1.3. Solar radiation availability. Solar radiation arrives the Earth's surface in a weakened form, as shown in section 2.1. This is because of two leading mechanisms known as atmospheric absorption and atmospheric scattering. Figure 3 illustrates an example of solar radiation attenuation effect. Absorption predominantly happens because of the presence of water vapor and ozone in the atmosphere and on a lesser extent due to other gaseous substances such as (O_2, CH_4, CO, CO_2, NO_2) [6].

The concentration of water vaper and O_3 and other compounds differ in location and time. The ozone absorbs almost all of the radiation with wavelengths below 290 nm at the upper atmosphere. A peak in the ozone absorption is found at around 600 nm. Water vapor primarily absorbs bands in the infrared range, "centered at 1100, 1400 and 1900 nm and in thin bands below 1000 nm." Water and carbon dioxide on the other hand absorb almost all the radiation over 2500[1]. Scattering is caused by the interaction between radiation and air molecules, dust and water vapor. The ferocity scattering is dependent on the number of particles pumped into by the radiation and the ratio of particles size to wavelength of the radiation. The particles' number in which radiation passes through is dependent on consternation of moisture and dust in the atmospheric surrounding and radiation optical path length [6].

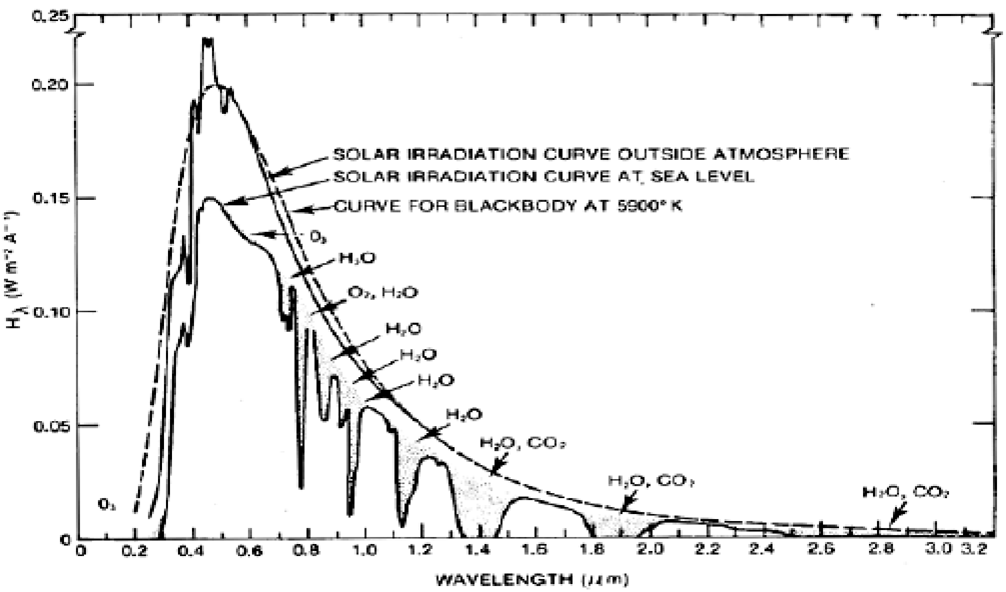

Figure 3: Solar radiation attenuation effect [2]

The radiation's path length is portrayed by the notion of air mass m, which is the path length in respect to that at the zenith at sea level. An estimation for m, for the zenith angles that range between 0 and 70°, is expressed by [6]:

$$m = \frac{1}{\cos(\theta_z)} \tag{4}$$

where the zenith angle denoted as θz (angle of incidence of beam radiation on a horizontal surface). On that account, m=1 at zenith and see level. For m=2 and θ_z=60°. The exoatmospheric region by definition, is expressed to be equal to zero. Moreover, the mass of the air can be lower than one for higher altitudes above the sea level.

Furthermore, the concentration of moisture and dust in the atmosphere, and air pollution, is a quantity dependent on time and location. The scattered radiation is dispersed in all directions, some of which reaches the Earth's surface while the rest goes back into space. Accordingly, the overall solar radiation must be differentiated between this dispersed fraction and the fraction that directly reached the surface. The beam radiation, also known as direct radiation, indicates the solar radiation received directly from the Sun without it being scattered by the atmosphere, While the diffuse radiation, also known as sky radiation, resembles the radiation received after its direction being changed due to the scattering of the atmosphere. The sum of these two constituents is referred to as total solar radiation. This differentiation is vital for CSP systems because they can only tackle the direct radiation. A necessary indicator is the Direct Normal Irradiance (DNI), that measures the normal constituent of the direct radiation reaching the Earth's surface which can be calculated as following :

$$\mathrm{DNI} = \mathrm{G_{on}} \cos(\theta_z)\, \tau_s \tau_{gas} \tau_{ozone} \tau_{wv} \tau_{ae} \tau_{cl} \tag{5}$$

It is detected from the above DNI equation that the scattering attenuation transmission coefficients is donated by τ_s, distributed gases by absorption (predominantly CO_2 and O_2) is expressed as τ_{gas}, where ozone absorption is donated by τ_{ozone} and water vapor τ_{wv} , aerosol and cloud extinctions are donated by τ_{ae} , τ_{cl} [7].

2.1.4. Concentrating solar power suitable locations. The aptness of sites for the production of solar energy can be evaluated by taking the average of historical data. The Direct Normal Irradiance (DNI) is an appropriate indicator to indicate the location of the best sites for the generation of solar power. (DNI) is unified over the course of a year and indicates the total amount of energy collected by direct normal radiation. A map of the world DNI combined over the course of a year is shown in Figure 4.

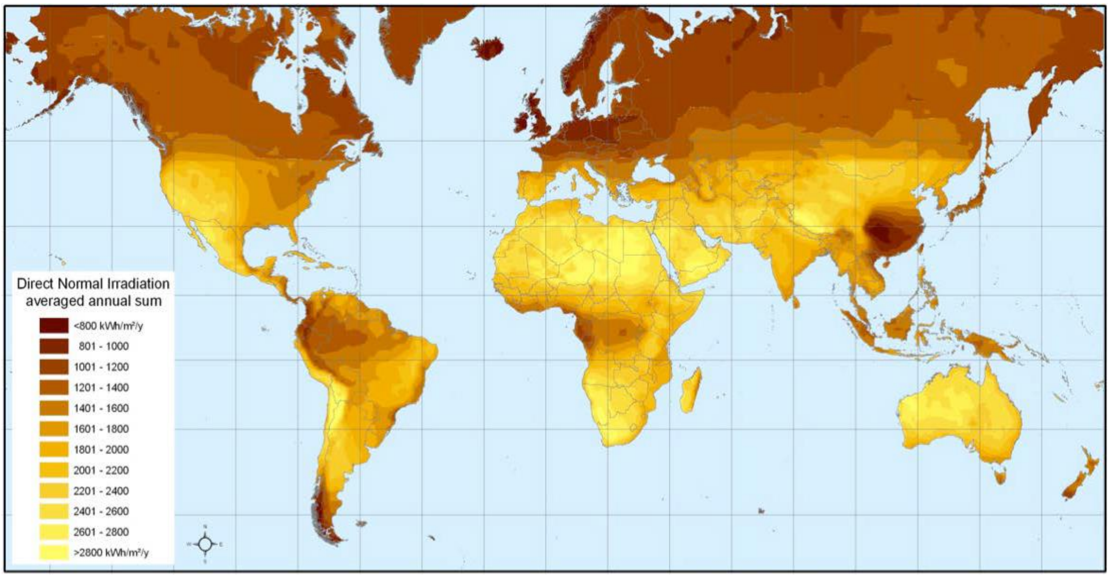

Figure 4: Annual Direct Normal Irradiation of the world [2]

It has been revealed that a minimum of 2’000 [kWh/m2. y] is vital for the installation of CSP plants, 2’500 [kWh/m2. y] being more likely to support competitiveness [7]. The areas shaded in yellow account for the largest possibility for the installation of Concentrated Solar Power plants. These areas include Australia, the Middle East, South Western USA, some parts of South America, Mexico, North Africa, South Africa and central Asian countries [8].Land factors have to also be taken into consideration when selecting suitable areas for CSP plants [9]. This is performed by ruling out all areas that are not suitable due to the structure of the ground, slope, agriculture, water bodies, shifting sand, areas restricted or protected, forests, etc. The global exclusion map found below in Figure 5 displays remaining large suitable areas, particularly in developing countries.

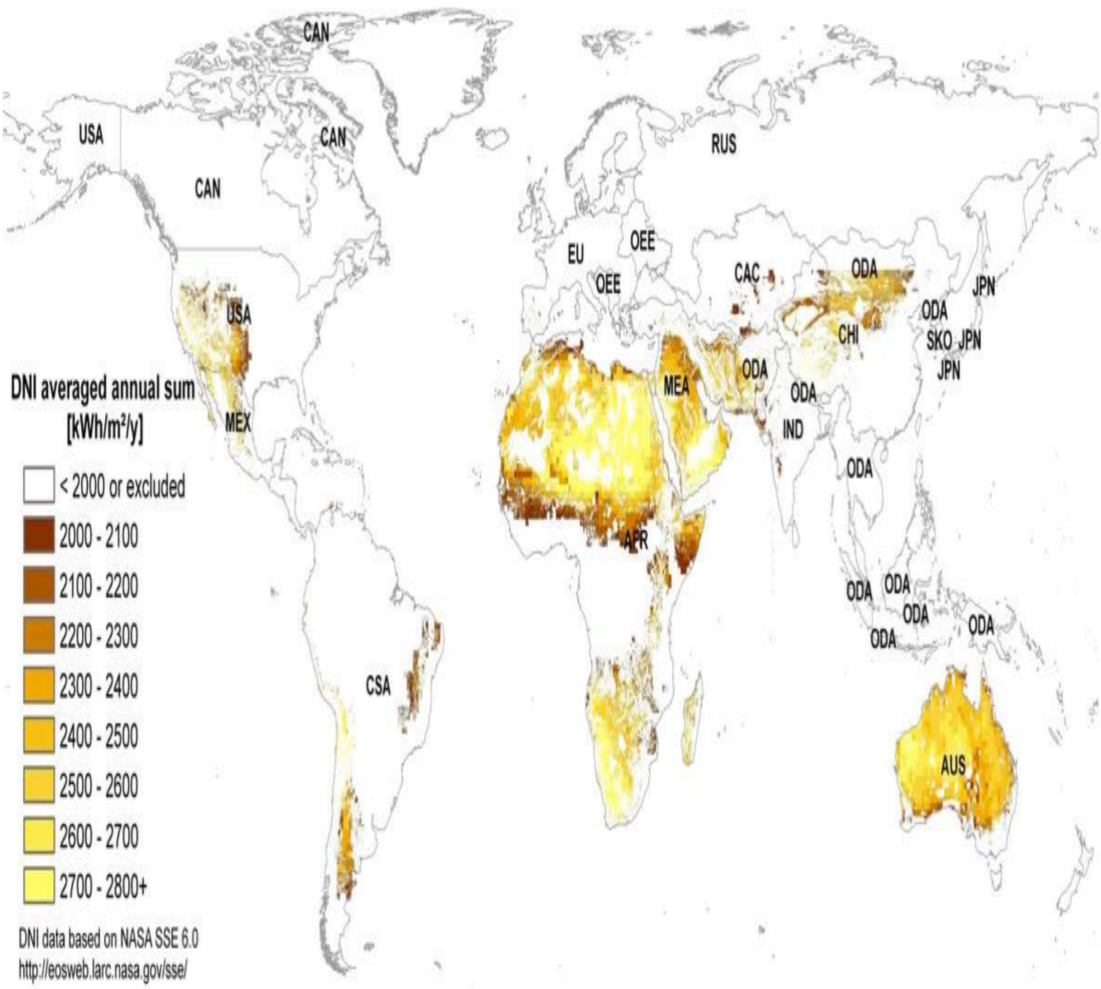

Figure 5: Recommended sites for construction of CSP Plants [1]

It is not possible to foretell data for rapid future beam radiation, which would be the greatest way to evaluate the accomplishment of a CSP system. Therefor, data incorporated from historical records are very convenient tools. The typical meteorological year (TMY) group of data is a great example. It is a gathering of historical meteorological data for a specific site over the course of. The strategy used includes selecting, for each month of the year separately, the most average month amid the set of months obtainable. The product is a collection of sets of hour-by-hour DNI indicating the representative meteorological contrasts and the average DNI combined over the course of a year [4].

2.2. Abu Dhabi and UAE

Abu Dhabi is chosen for the plant implementation due to its outstanding suitability for the collection of solar thermal energy. Consequently, it is vital to discuss and present all the considerable factors leading to its suitability for solar thermal power generation. That will include its solar radiation and climate. In the following section we will be presenting Abu Dhabi's dry bulb temperature, Rate of DNI received every year and the Abu Dhabi's relative humidity. In this section: Air temperature, relative humidity, direct normal radiation, water scarcity, electricity consumption, of Abu Dhabi, carbon dioxide emissions and concentrated solar power projects in the UAE are exposed in subsection 2.2.1- 2.2.6 and 2.1.7, respectively[10].

2.2.1. Abu Dhabi air temperature. Table 1 illustrates the mean dry bulb temperature in Abu Dhabi during the day of each month [29]. It is very clear that the average temperature reaches its peak during noon with August having recorded the highest average temperature. Air temperature has a notable effect on the gas cycle thermal performance; hence it must be considered for creating a combined power plant with a topping gas turbine cycle.

Poullikkas [8] revealed that the plant's performance is highly influenced by the increase the inlet air temperature. In order to improve the plant's function, an inlet air cooling system can be installed. The authors proposed a novel inlet air cooling system integrating desiccant cooler systems and Maisotsenko cooling [2], [11].

2.2.2. Abu Dhabi relative humidity. Relative humidity is another crucial factor that highly influences the cycle performance. Poullikkas studied the cycle performance affect by relative humidity [8], and the results demonstrated that the thermal performance of the plant's is diminished due to humidity [12].

In addition, it is noted that even the smallest decrease of power is taken into consideration nowadays due to that increase in the size of the gas turbine and establishment of steam injection in gas turbines. Other studies concerning inlet air humidity ratio growth denote a development for gas turbine power output and efficiency. Furthermore, the chief purpose behind the difference between the acquired results can be due to the size of the gas turbine that has been evaluated for investigation. Nevertheless, it can be asserted that humid climates highly reduce the performance of humid air turbine cycles [8]. Table 2 illustrates the hourly relative humidity for the whole year of Abu Dhabi. This data was provided by the National Renewable Energy Laboratory (NREL) database [2].

2.2.3. Abu Dhabi direct normal radiation. The most vital component that must be considered for CSP analysis and solar thermal power generation is the rate of DNI obtainable within the appointed site's location. Table 3 shows the the mean rate of DNI available in Abu Dhabi during the day of each month. Therefore, it can be noted that the Rate of DNI supplied reaches its peak at noon [1].

2.2.4. Abu Dhabi electricity consumption. The highest electricity demand in the UAE goes to Abu Dhabi [13]. "It is reported that Abu Dhabi's peak load demand in August 2008 was 5516 (MWe) whilst 6255 (MWe) was recorded in August 2009" [2]. It can be seen that the electricity demand within UAE reflects the electricity consumption which is significantly increasing in Abu Dhabi.

Consequently, more power plants and higher electricity production are in high demand and is the subject of extensive research. Figure 6 illustrates the growth in electricity consumption in Abu Dhabi which clearly demonstrates the rising demand for electricity in the coming years. ADWEC predicts the highest electricity consumption for 2015 will reach 11200 (MWe) in comparison to 6,885 (MWe) in 2010 [14]. Moreover, Figure 7 portrays the peak load demand and electricity capacity for Abu Dhabi.

Table 1: Temperature during a day in Abu Dhabi [1].

Time	JAN Temp. (°C)	FEB Temp. (°C)	MAR Temp. (°C)	APR Temp. (°C)	MAY Temp. (°C)	JUN Temp. (°C)	JUL Temp. (°C)	AUG Temp. (°C)	SEP Temp. (°C)	OCT Temp. (°C)	NOV Temp. (°C)	DEC Temp. (°C)
0	15.651	16.928	19.771	23.336	26.509	28.956	30.754	31.564	29.49	25.535	21.88	17.735
1	15.212	16.314	19.393	22.836	26.067	28.203	30.274	31.248	28.903	25.006	21.193	17.212
2	14.771	15.867	18.977	22.51	25.696	27.843	29.729	30.290	28.45	24.293	20.67	16.725
3	14.154	15.735	18.787	21.976	25.077	27.303	29.348	29.832	27.896	23.693	20.11	16.561
4	13.803	15.035	18.487	21.83	24.919	27.143	29.274	29.564	27.63	23.277	19.57	16.103
5	13.654	14.464	18.141	21.34	24.687	26.803	28.945	29.148	27.303	22.909	19.443	15.767
6	13.267	14.267	17.890	21.71	25.477	28.02	29.319	29.222	27.53	23.132	19.136	15.548
7	14.106	15.407	19.167	24.2	29.106	30.89	31.880	31.661	29.736	25.616	20.853	16.174
8	16.187	17.825	21.145	26.803	32.458	33.743	34.351	34.654	31.91	28.767	23.05	18.241
9	18.277	20.342	23.103	29.03	34.632	35.846	36.780	36.767	33.803	30.758	25.88	20.709
10	20.632	22.789	25.106	30.836	36.471	37.943	38.829	39.129	36.52	33.151	27.873	23.119
11	21.806	24.546	26.396	31.763	37.471	38.846	40.158	40.641	38.196	34.741	29.03	24.616
12	22.58	25.760	26.958	32.7	37.335	39.216	40.693	40.874	38.816	34.683	29.796	25.045
13	22.945	26.196	27.125	32.046	37.054	39.13	40.854	41.354	39.243	34.764	29.89	25.203
14	23.116	25.957	26.851	31.466	36.364	38.966	40.651	40.790	38.6	34.283	29.53	25.054
15	22.661	25.7	26.590	30.886	35.909	37.906	39.567	39.941	37.583	33.158	29.086	24.671
16	22.058	24.596	25.858	29.636	35.048	37.023	38.235	38.571	36	32.129	27.933	23.922
17	20.783	23.253	24.774	28.573	33.629	35.6	36.951	37.290	34.55	30.764	26.726	22.603
18	19.516	21.960	23.367	27.313	31.732	33.856	35.812	36.112	33.516	29.535	25.513	21.377
19	18.751	20.917	22.403	26.456	30.416	32.44	34.516	34.896	32.486	28.371	24.753	20.535
20	17.983	19.878	21.983	25.716	29.635	31.576	33.509	33.9	31.76	27.803	23.833	19.893
21	17.403	18.960	21.074	25.273	28.696	30.753	32.748	33.306	31.006	27.129	23.5	19.212
22	16.7	18.146	20.425	24.626	27.916	30.016	32.138	32.480	30.426	26.412	22.816	18.5
23	16.1	17.664	20.054	23.99	27.212	29.493	31.432	31.980	29.86	25.806	22.403	17.887

Table 2: Relative humidity during a day in Abu Dhabi [1].

Time	Jan (%)	Feb (%)	Mar (%)	Apr (%)	May (%)	Jun (%)	Jul (%)	Aug (%)	Sep (%)	Oct (%)	Nov (%)	Dec (%)
0	81	79.03	77.87	69.1	65.93	69.06	70.80	67.96	79.86	72.80	83.43	76.45
1	82.12	80.14	79.77	69.2	66.35	71.03	71.16	67.48	81.76	74.70	84.73	77.64
2	81.80	80.92	80.12	70.66	65.67	70.03	72.70	69.70	82.93	75.25	85.3	78.51
3	83.35	80.42	80.51	73.03	67.80	70.96	72.58	69.58	84.73	76.58	86.23	77.93
4	83.54	81.10	81.58	72.36	67.35	69.3	71.54	68	82.8	75.70	86.96	77.83
5	84.03	82.32	82.87	72.4	67.96	68.43	72.19	68.38	82.46	74.77	86.16	79.19
6	84.51	81.57	83.45	72.4	64.90	64.06	70.58	68.22	80.63	74.16	85.36	80.29
7	82.80	76.03	78.58	61.2	52.06	55.2	62.51	58.96	68.6	64.38	79.1	76.03
8	77	69.75	70.58	51.96	40.74	47.43	51.38	45.96	56.83	54.06	71.93	68.67
9	70.70	61.96	65.32	44.56	32.41	40.6	41.87	38.70	48.93	47.90	63.33	60.77
10	61.41	51.64	56.29	35.3	26.83	32.3	35.38	31.77	37.63	38.32	56.6	52.67
11	54.70	44.25	51.96	32.3	24.61	30.06	32.45	28.22	32.63	32.45	51.3	48.06
12	50.61	40.85	51.35	30.56	26.32	27.53	30.74	28.32	30.8	34.32	48.03	47.06
13	47.80	38.21	51.38	33.13	28.93	29.1	30.22	29.22	31.4	36.25	47.86	46.06
14	47.16	40.57	51.09	35	30.12	30.6	31.29	32.77	35.06	38.64	48.9	47.38
15	49.51	42.78	53.25	38.83	32	34.7	35.38	36.29	39.73	42.70	50.3	49.38
16	53.54	46.78	54.51	43.16	34.64	37.36	40.74	40.74	47.36	48.16	55.1	52.48
17	61.32	53.32	61.29	47.2	41.06	43.76	46.22	47.58	55.63	55.58	63.5	60.06
18	68.87	61.32	67.64	52.23	50.87	51.1	51.51	52.32	61.36	61.77	71.53	65.12
19	72.80	65.39	72	56.93	57.74	58.33	58.58	59.19	66.56	66.93	74.3	69.19
20	76.19	70.07	73.32	60.9	59.90	61.8	63.25	62.90	69.63	68.35	77.83	70.51
21	77.77	73.78	75.41	64.16	64.48	64.43	66.29	65.41	73.86	70.67	79.4	72.25
22	78.32	76.35	77.80	66.03	64.12	67.16	68.35	67.77	76.2	71.48	81.06	74.45
23	79.74	77.46	78.06	67.8	65.22	68.4	70.06	68.32	77.83	71.80	82.63	75.67

The economic crisis in 2008 did not restrain the sustained increase in electricity demand in the UAE, and the country’s supply of the natural gas therefor was inadequate to generate the required electricity demand those years [15]. Consequently, UAE officials are investigating multiple solutions to decrease natural gas and fossil fuel consumption in electricity generation. As a result, the solar thermal power plant is a prosperous solution to the previous concerns.

Table 3: Average DNI during a day in Abu Dhabi [1].

Time	JAN DNI W/m^2	FEB DNI W/m^2	MAR DNI W/m^2	APR DNI W/m^2	MAY DNI W/m^2	JUN DNI W/m^2	JUL DNI W/m^2	AUG DNI W/m^2	SEP DNI W/m^2	OCT DNI W/m^2	NOV DNI W/m^2	DEC DNI W/m^2
0	0	0	0	0	0	0	0	0	0	0	0	0
1	0	0	0	0	0	0	0	0	0	0	0	0
2	0	0	0	0	0	0	0	0	0	0	0	0
3	0	0	0	0	0	0	0	0	0	0	0	0
4	0	0	0	0	0	0	0	0	0	0	0	0
5	0	0	0	0	0	0	0	0	0	0	0	0
6	0	0	0	19.6	70.7	66.1	23.5	0	0	0	0	0
7	96.0	141.3	182.3	277.2	332.4	323.5	237.9	222.8	188.3	197.0	211.3	102.9
8	234.5	416.6	371.1	475.6	572.6	576.6	471.2	477.0	507.9	541.9	485.4	367.6
9	543.5	639.9	502.0	596.7	688.2	703.0	611.1	650.6	687.4	728.0	679.9	582.3
10	659.4	726.9	552.5	629.2	771.1	793.7	710.4	749.4	794.1	819.6	754.1	657.6
11	674.6	789.6	577.8	661.7	813.6	854.6	780.7	816.6	856.8	848.4	751.8	670.7
12	722.0	821.0	585.6	648.9	836.5	859.6	794.6	830.4	867.5	833.6	735.8	660.0
13	709.5	809.1	580.8	648.3	834.4	855.1	791.3	825.6	843.6	814.6	735.8	660.7
14	669.0	765.5	583.6	607.8	802.0	816.2	735.8	777.8	779.1	761.4	694.1	617.7
15	605.5	700.2	561.5	546.8	714.8	728.8	644.6	686.0	668.6	634.8	562.2	531.1
16	443.2	583.1	470.3	452.1	574.7	582.5	508.7	506.2	417.6	365.5	308.0	341.0
17	102.0	253.8	234.1	217.7	282.4	288.2	232.9	201.3	101.5	10.8	0	0
18	0	0	0	0	0	10.6	2.8	0	0	0	0	0
19	0	0	0	0	0	0	0	0	0	0	0	0
20	0	0	0	0	0	0	0	0	0	0	0	0
21	0	0	0	0	0	0	0	0	0	0	0	0
22	0	0	0	0	0	0	0	0	0	0	0	0
23	0	0	0	0	0	0	0	0	0	0	0	0

2.2.5. UAE carbon dioxide emission. In the UAE, CO2 emission is escalating. During the last three years, it was revealed that CO_2 emissions have increased dramatically from 26.4 ton/pop to 32.2 ton/pop [16]. Figure 8 demonstrates the escalating increase in the UAE's CO_2 emission. It can be noticed that the CO_2 emission is increasing rapidly. This means UAE relies more on fossil fuel with the increase of electricity demand. Investing more on the CSP technology will be one of the solutions to reduce the CO_2 emission.

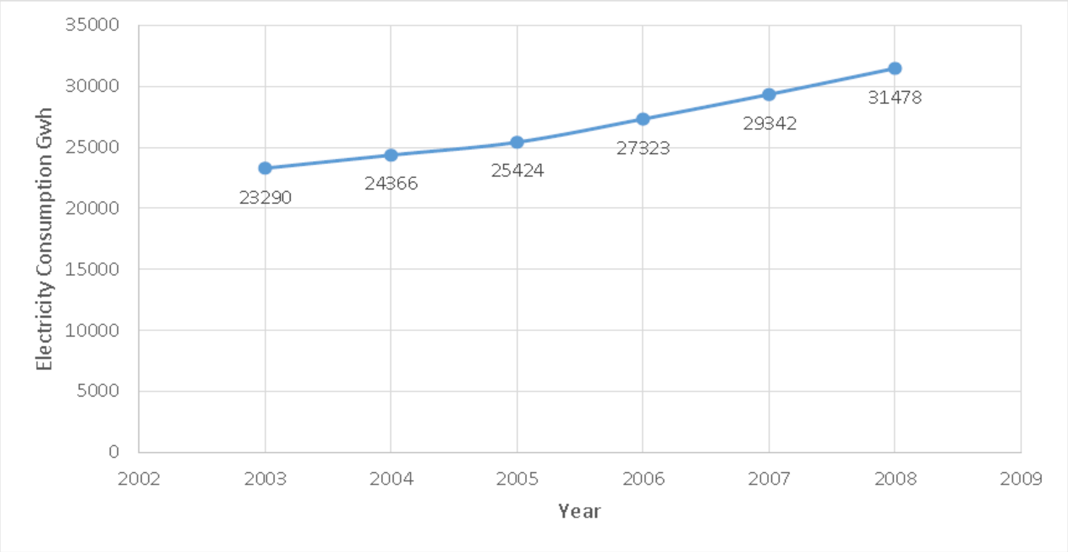

Figure 6 : Abu Dhabi Electrical consumption Growth [1].

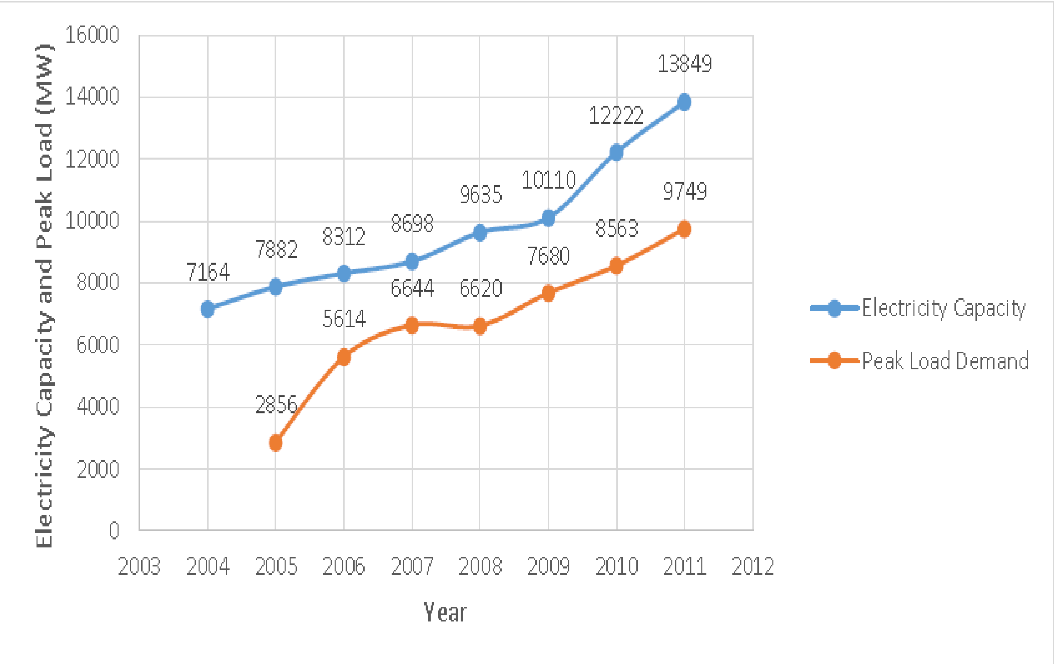

Figure 7: Abu Dhabi peak load demand and and electrical capaciy [1].

Moreover, the dispersal of CO2 emission from fuel consumption by different sectors of industry in the UAE is illustrated in Figure 9. Note that 39% of the CO2 emission is correlated with electricity and thermal energy generation. This amount can be decreased immensely by establishing renewable energy for heat and electricity applications [17].

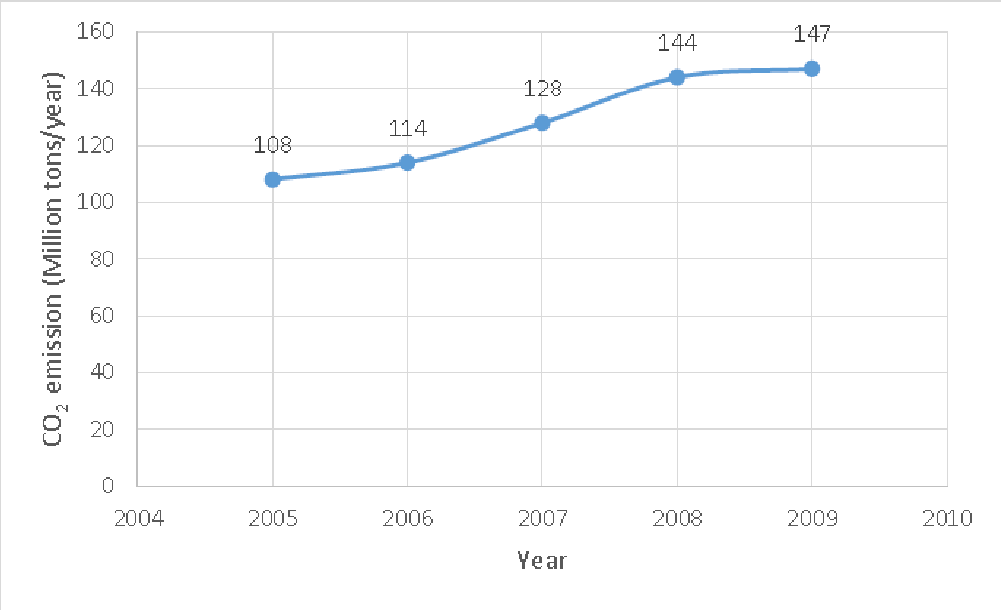

Figure 8: UAE CO2 emission Growth [1].

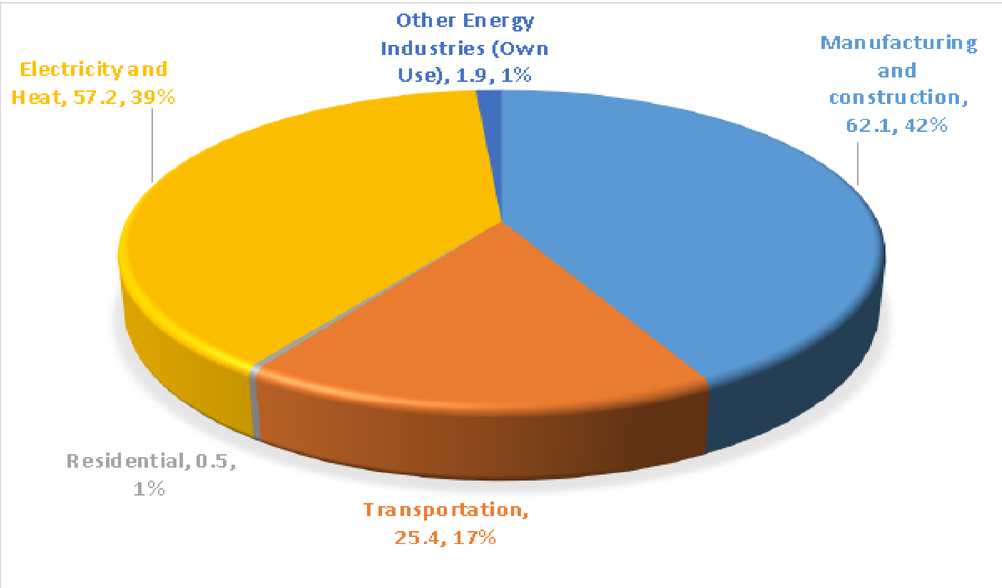

Figure 9: UAE CO2 emission by different industrial sectors [1].

2.2.6. Water scarcity. Shortage of water is another obstacle that has to be taken into account in power plant designing. Water treatment facilities highly affect the cost of power plant capital and operating systems. UAE's annual water consumptions exceeds the annual rain fall significantly.It is therefor important to build CSP plants with lower specific water consumption [18].

2.2.7. Implementation of CSP projects in the UAE. There are various studies centered on CSP and solar thermal technologies incorporated within the UAE. Shams 1 being the first solar thermal power plant that harnesses CSP technologies in the UAE. A power plant of 120 MW power output was designed by Shams 1 which is considered the biggest "single unit CSP integrated solar thermal power plant in the world" [19], located at Madinat Zayed. This power plant uses 768 solar collector assemblies which is around (258,048 mirrors) to heat up the oil inside the tube receivers [20]. With oil temperature varying from 293℃ to 393℃ inside the tubes. The heated oil is utilized in the steam generator to provide the desired thermal input for the plant's operation [21]. Moreover, the first thermal power plant integrated with CSP tocology was done by Shams 1 to reduce the reliance on water consumption by implementing dry cooling techniques [22]. In order to superheat steam temperature from 380℃ to 540℃ it uses a supplementary heater enhancing the plant overall efficiency. The supplementary heater that works by employing fossil fuels generates approximately 45% of the power. Another ongoing project in the UAE is Beam-Down Solar tower. It is exploring new designs for heliostat field collectors and solar towers [23]. This project includes Masdar Institute of Science and Technology, Japan Cosmo Oil, and Tokyo Institute of Science and Technology. In fact, A preliminary plant with a 100 KWe capacity has already been built near Masdar City [24]. The submitted arrangement appoints a set of secondary mirrors that shares the solar radiation through receiver on the ground [25]. Thirty-three mirrors on the ground are employed in the pilot plant alongside two axis tracking systems [26].

2.3. Concentrating Solar Power

In this section, a description of general and distinctive features of CSP technologies is given alongside a comparison with other solar technologies (2.3.1), followed by a presentation of the different CSP technologies available (2.3.2). A history about the parabolic trough solar collector (PTSC) technology will be illustrated at (2.3.3). Moreover, power and related work configurations will demonstrated at (2.3.4) and (2.3.5).

2.3.1. Concentrating solar power features. In the current time period, Various technologies are accessible to change solar radiation into electrical power.

They can be categorized into two groups photovoltaics (PV) and solar thermal power technologies. Photovoltaics transforms solar radiation into DC electricity based on semiconductors displaying the photovoltaic effect. Solar thermal power technologies on the other hand convert solar radiation into thermal energy. This heat is thereafter transformed into mechanical energy by a thermal engine. Which is then converted into electrical power using a generator. Recently, both of the technologies rapidly developed and there are attempts to decrease their cost. Even though there is a clear competition between the two technologies, there is no doubt that both technologies will be used more in the future in order to take further steps in decreasing CO2 emissions and our dependence on fossil fuels [27].

Solar Thermal Power Technology is portrayed by a variety of concepts. These concepts are divided into non-concentrating and concentrating solar power systems (CSP). The non-concentrating systems refer fundamentally to solar combined plants and solar updraft tower which are still on demonstration stages. CSP Systems on the other hand are more mature systems. The method of generating electricity by CSP systems are comprised of the following vital steps:

- concentrator solar power systems are used to store the direct normal irradiance (DNI).
- concentrator solar power receivers are used to increase the flux density radiation and convert it into thermal energy [28].
- Turbine engines are used to convert thermal energy to mechanical energy [29].
- Generators are used to transfer mechanical energy into electricity energy.

In order to collect high energy density on the receiver, concentration of solar radiation is needed. High operating temperatures, which are necessary to reach high thermal efficiencies of the power generation cycle, are therefore obtained by this technique. By reducing the area in which thermal energy is lost, these high temperatures can be acquired. That is achieved by introducing an optical device between the source of radiation and the receiver. The concentration ratio can be defined as the ratio of concentrator aperture area to the receiver area which illustrates a good estimate of the factor by which radiation flux is heightened on the receiver. It is demonstrated by the following [2]:

$$C = \frac{A_a}{A_{rec}} \tag{6}$$

where the aperture area of the concentrator is donated by A_a and area of the receiver by A_{rec}.

Based on the type of receiver and concentrator, the power cycles can be categorized as Stirling or gas/steam turbine cycle. As mentioned in this section, the DNI concentration is the main factor to allocate the suitable locations for CSP. Additionally, conventional power cycles using concentrating solar power plants (hybridation) are more dispatchable, either by supporting solar power input by burning certain fuels or by producing thermal energy in order to convert it to electricity and deliver it at peak load [30].

2.3.2. Concentrating solar power configurations. Concentrating solar power systems are usually differentiated by some type of concentrator. In the current times, there are mainly four types of CSP technologies [9], as displayed in Figure 10:

a. Parabolic Trough Solar Collectors (PTSC)

b. Linear Fresnel Reflectors (LFR)

c. Heliostat Field Collector (HFC)

d. Parabolic Dish Collectors (PDC)

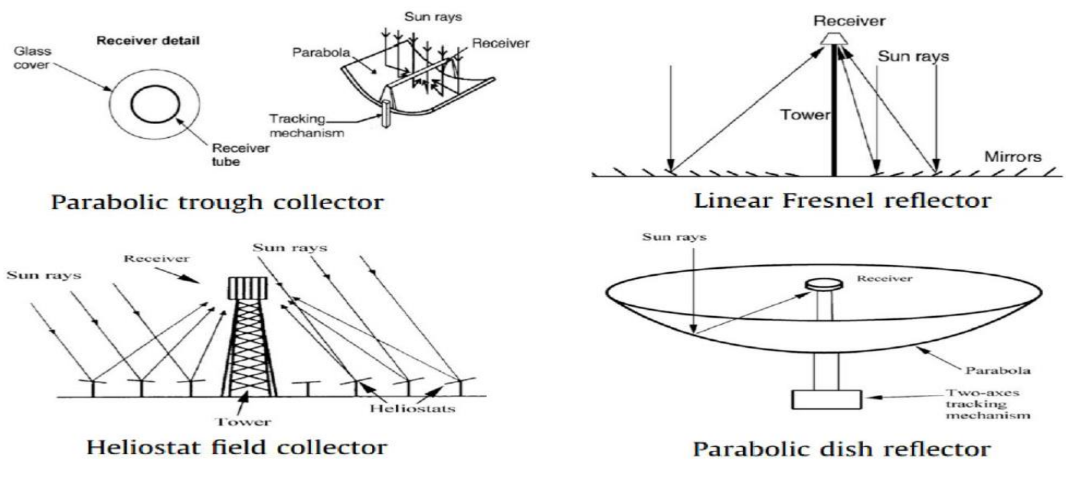

Figure 10: The Four Types of CSP Configurations [1].

This project's scope is limited to parabolic trough. However, there is a vital difference between towers/dishes and parabolic troughs/Fresnel reflectors that allows a greater comprehension of central receiver systems. The difference exists in the way they concentrate solar radiation. Fresnel reflectors and Parabolic troughs undergo concentration of solar beams on a linear receiver. Since they are two-dimensional then they can be rotated around a single axis of rotation. Conversely, towers and dishes must be able to move around two axes since they are there dimensional. They focus solar beam on a central receiver [2]:

$$C_{ideal,2D} = \frac{1}{sin\,\theta_s} \tag{7}$$

$$C_{ideal,3D} = \frac{1}{\sin \theta_s{}^2} \tag{8}$$

where the half angle substended by the sun $\theta_s = 0.027°$. Based on the second law of thermodynamics and granted that the receiver temperature T_{rec} is equal to the Sun blackbody temperature T_s [6], the maximum concentration ratios for two-dimensional concentrators $C_{ideal,2D}$ (Fresnel/parabolice) and three-dimensional concentrators $C_{ideal,3D}$ (dishes/tower) are acquired [31].

Therefore, parabolic troughs and Fresnel reflectors' maximum concentration ratio is $C_{ideal,2D=}212$, whilst the one for dishes and towers is $C_{ideal,3D}$ =45000.In practice, there must be an increase in the acceptance angle of the concentrator which in turn leads to a decrease in achievable concentration ratios. Nonetheless, as portrayed in Table 1, the concentration ratio range for dishes and towers continues to be more significant than parabolic troughs and Fresnel reflectors [32].

These greater concentration ratios allow higher operating temperatures which lead to more efficient power cycles. To be able to achieve high concentration ratios, the collectors must be aligned to track the Sun in order for the direct radiation to be reflected onto the receiver surface, hence sun-seeking or programmed systems are a necessity. As mentioned earlier, single tracking system is needed for parabolic troughs and Fresnel reflectors, while two-axis tracking systems is needed for towers and dishes [33]. Table 4 will illustrate the Specification Comparison of the Four CSP Technologies.

Table 4: Specification Comparison of the Four CSP Technologies [4].

CSP Type	PTSC	LFR	HFC	PDC
Concentration ratio	50-90	25-50	600-2000	Up to 3000
Operating temperature (C°)	200-1000	450	500-1000	600-800

2.3.3. Parabolic trough solar collector. The parabolic trough solar collector (PTSC) is one of the most developed concentrated solar power innovations around the world which broadly utilizes the thermal energy as the main source of power. For example, Solar Energy Generating Systems (SEGS) in California is a pure solar energy power plant to generate electricity built in 1984. SEGG power plant, which is located in Mojave Desert, California consists of nine solar power plants with total capacity output of 354 MW.

It is considered as the second largest solar power plant in the world. The PTSC main parts are the collector, receiver (absorber tube) and glass cover. The collector has a parabola shape manufactured by reflective material (mostly Aluminum) which plays as reflective surface for parallel rays to be reflected on to the receiver. The receiver consists of a black meal tube that is painted on black to absorb more heat than it reflects. To be able to reduce the heat losses through radiation and convection glass cover is used to cover the receiver and reduce these losses. The operating temperature of the PTC starts from 50℃ and goes to temperatures as high as 1000℃. This temperature range is suitable for the Brayton cycles applications which leads to a relatively decent thermal performance and moderate efficiency. Nevertheless, a higher operating temperature is needed for integration the gas turbine power plants with CSP technology. The heat transfer fluid (HTF) is the fluid which passes through the receiver and collect the thermal energy obtained from solar and deliver it to the gas turbine engine. The heat transfer fluid flowing through the receiver conveys the thermal energy acquired from solar radiation to operate a heat engine. Synthetic oil and Pressurized water are the most commonly used HTF in PTC collectors. Table 5 shows variety of HTF can be used on PTSC such as Therminol VP-1, molten Nitrate salt, air and Helium [34]. Moreover, Table 5 illustrates the HTF with its corresponding optimal mass flow rate and operation temperature ranges. Air is selected as HTF since the cycle is operating at higher temperature and the arability of air without additional costs. The approach method is to utilize air to directly generate thermal heat within the receiver. This method is referred to as direct heat generation (DHG). It can be noticed that the optimal mass flow rate of air is about 0.2 kg/s which is smaller compared to other HTFs. The reason behind is that the heat capacity and thermal conductivity of air is smaller than the other most commonly used HTFs. Increasing the mass flow rate of air will lead to higher pressure losses and therefore decreasing the exergy efficiency of the collector. The reason behind the significant drop of pressure while increasing the mass flow rate is that air has lower density compared to other HTFs. However, using the recommended optimal mass flow rate has showed a good thermal energy and exergy efficiencies compared to the other HTFs [34].

Table 5: Heat transfer fluid used on PTSC [34].

Working fluid	m_{optim} (kg/s)	Temperature range (K)
Pressurized Water	2	300 - 550
Therminol VP-1	2	300 - 650
Molten Nitrate Salt	4	550 - 800
Sodium Liquid	2	400 - 1100
Air	0.20	300 - 1300
CO_2	0.20	300 - 1300
He	0.03	300 - 1300

Figure 11 shows the thermal energy efficiency of air at different mass flow rates. It can be noticed that mass flow rate ranges from 0.2 kg/s to 0.5 kg/s have acceptable thermal energy efficiencies. Moreover, Figure 12 illustrates the exergetic efficiency of air at different mass flow rates. It can be shown that the optimal mass flow rate is 0.2 kg/s to obtain a maximum exergetic efficiency. Furthermore, an air mass flow rate of 0.1kg/s can be an alternative solution, although this solution is eliminated due to its lower thermal performance [35].

2.3.4. Power generation configurations. It is important to recall that Figure 4 shows that UAE deserts are the most suitable places for implementing CSP technology, these locations are suffering water scarcity [36].

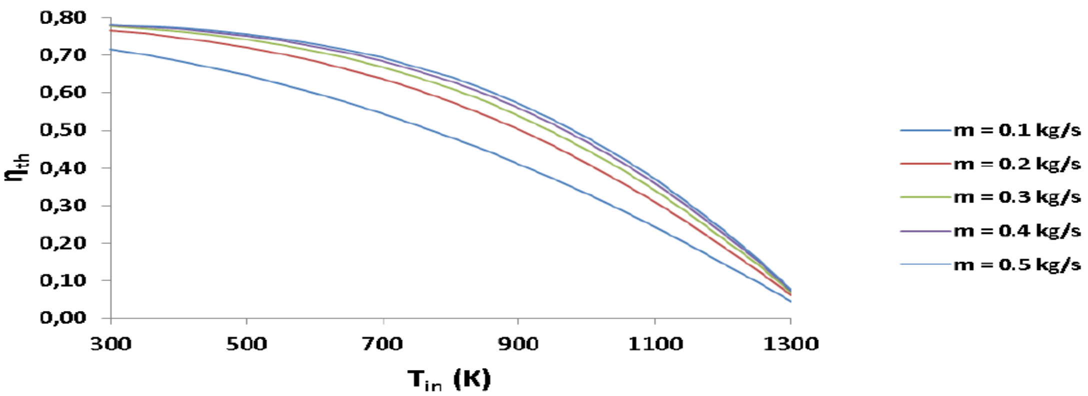

Figure 11: Thermal energy efficiency of air at different mass flow rates [34].

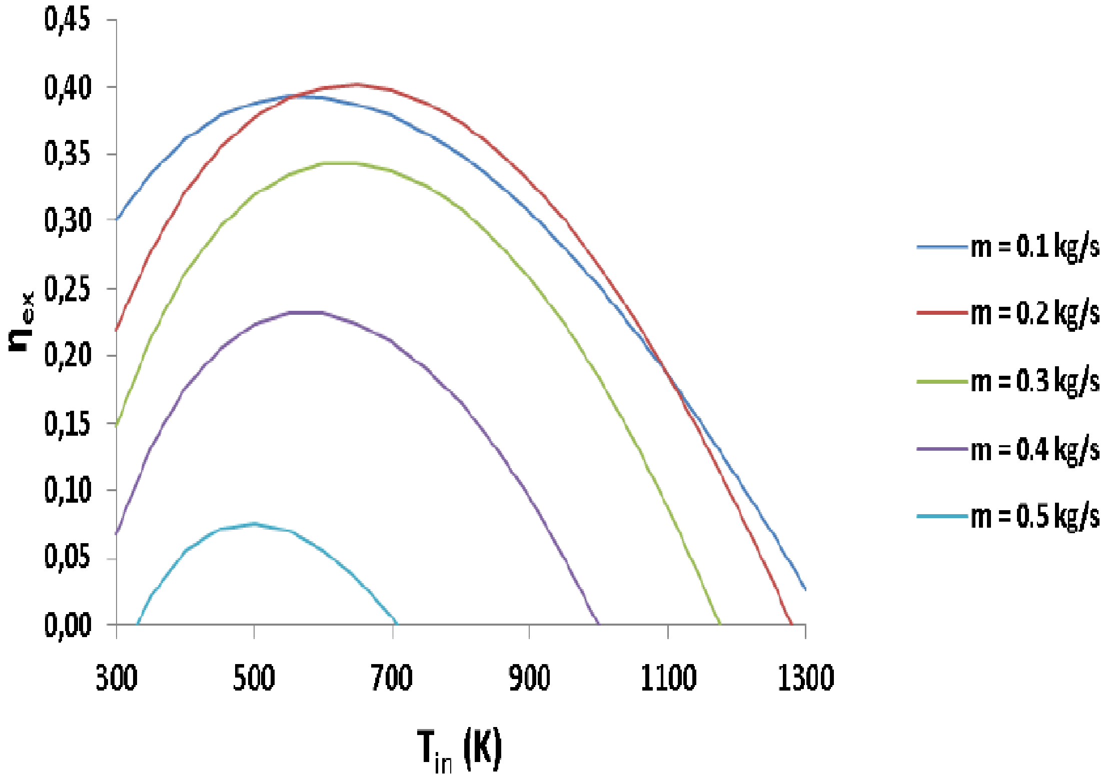

Figure 12: Exergetic efficiency of air at different mass flow rates [34].

The drawback of integrating PTSC with Rankine cycles, is that these configurations rely on water for a number of purposes. Firstly, a lot of water is lost at the blow- down of steam drum. Moreover, the condenser needs regular cooling, particularly at the evaporative cooling systems. Furthermore, cleaning the mirrors of PTSC technology requires water to maintain a high reflective surface. To overcome these problems, Brayton cycle configurations are introduced to reduce the reliance on water. For example, gas turbine cycle with intercooler and recuperator was introduced by Sandoz [37].

The configuration diagram of the proposed cycle was illustrated in Figure 13 [2]. This solution was not feasible long time ago since complication were countered in designing and manufacturing heat recovery, and intercooled recuperator that can sustain high temperatures. The heat exchanger that was used in the introduced configuration is air to air flat plate heat exchanger. Thus, building models similar to these configurations will lead to reduce the dependency on water resources where limited water is needed to be used for compressors washing and mirrors cleaning [38,39,40].

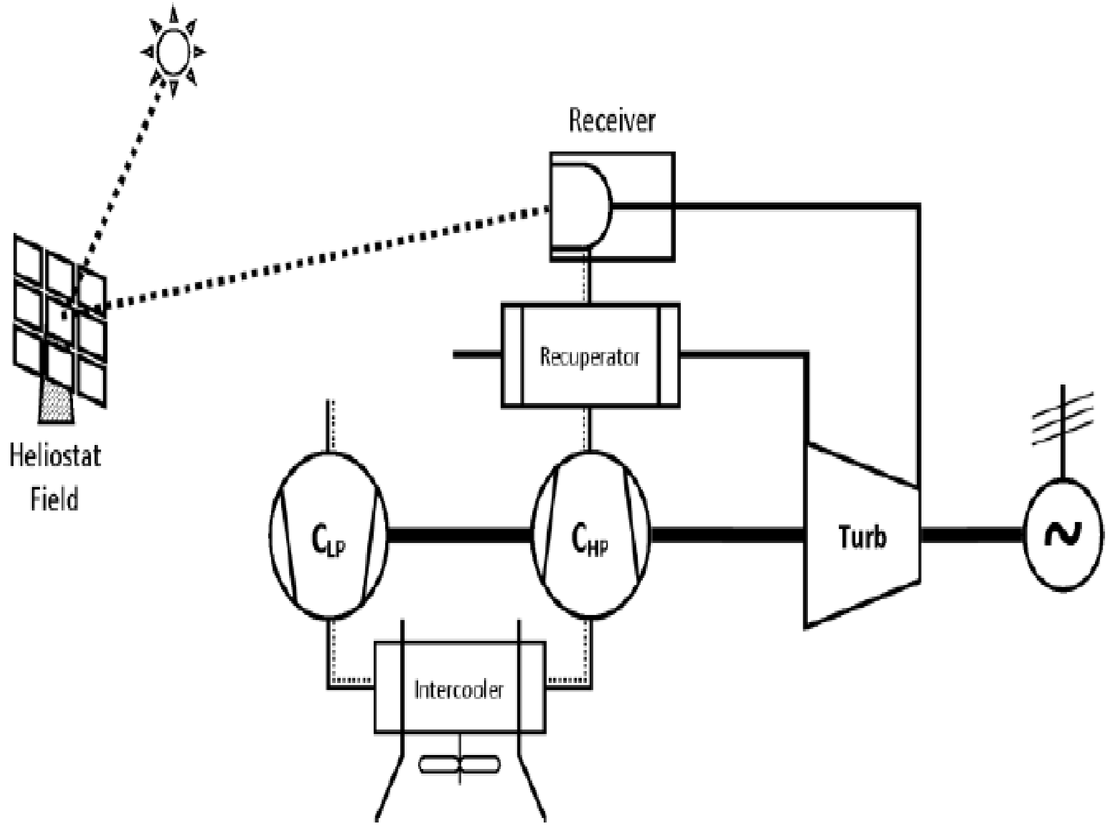

Figure 13: Intercooled-Recuperated Solar gas turbine Configuration [2].

2.3.5. Related work configurations. Three models from literature will be presented and brief tabulated results of these models will be illustrated. Furthermore, a proposed model for the project will be demonstrated on the upcoming chapter. Thermodynamic results related to the cycle performance, for the three literature bottoming cycles, are illustrated in Table 6.

The steam bottoming cycle (SBC) and steam air bottoming cycle (S-ABC) generate almost the same power output. Where SBC generate around 44120 kW and (S-ABC) generate around 44686 kW, whereas the conventical air bottoming cycle (C-ABC) delivers 41106 kW. Nevertheless, the S-ABC is the less efficient cycle in terms of energy and exergy. S-ABC topping cycle improves the cycle power by 28%, but it reduces the cycle efficiency from 36.56% to 31.87%. On the other hand, the more efficient cycle in terms of energy and exergy goes to SBC, where its energy efficiency is about 46.78%, SBC topping cycle energy increased by 10.21 % with the addition of the bottoming cycle. Where the topping SBC cycle efficiency is about 41.60%, the addition of bottoming cycle based on the SBC improved the energy efficiency by 5%.

Moving to the exergy efficiency effect, the addition of bottoming cycle to the SBC and C-ABC increase their cycle exergy efficiency from 34.36% to 44.66% and 41.60%, respectively. Whereas the S-ABC exergy efficiency slightly decreased to 33.82% by the addition of air bottoming cycle. Furthermore, it can be noticed that the S-ABC exergy efficiency is greater than its energy efficiency. Figure 14 and 15 represents the configuration cycle of SBC and C-ABC [13].

Table 6: Summary of the parameter of the three-bottoming cycle [13]

Parameters	S-ABC [13]	C-ABC [13]	SBC [13]
Net power output (KW)	44686	41106	44120
Energy Efficiency (%)	31.87	43.63	46.78
Exergy efficiency (%)	33.82	41.60	44.66

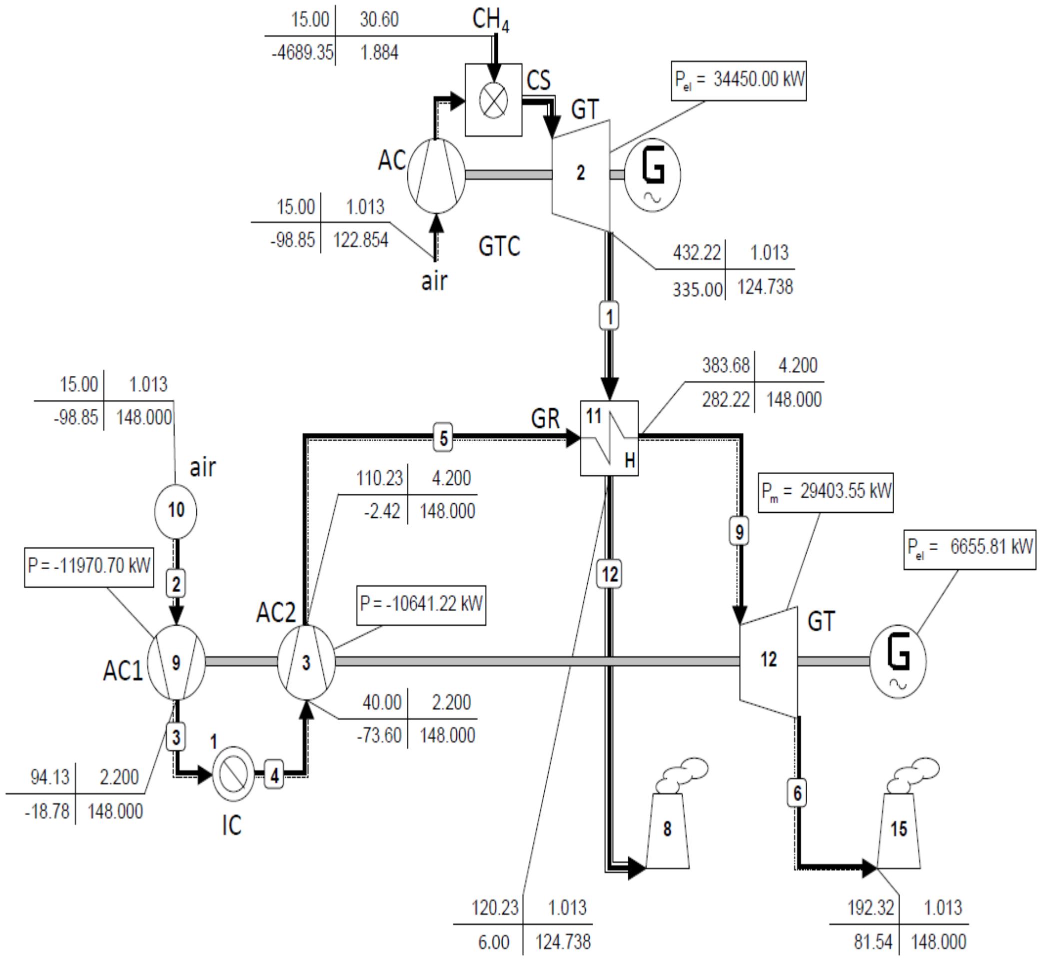

Figure 14: The conventional air bottoming gas turbine cycle without solar energy (C-ABC) [13].

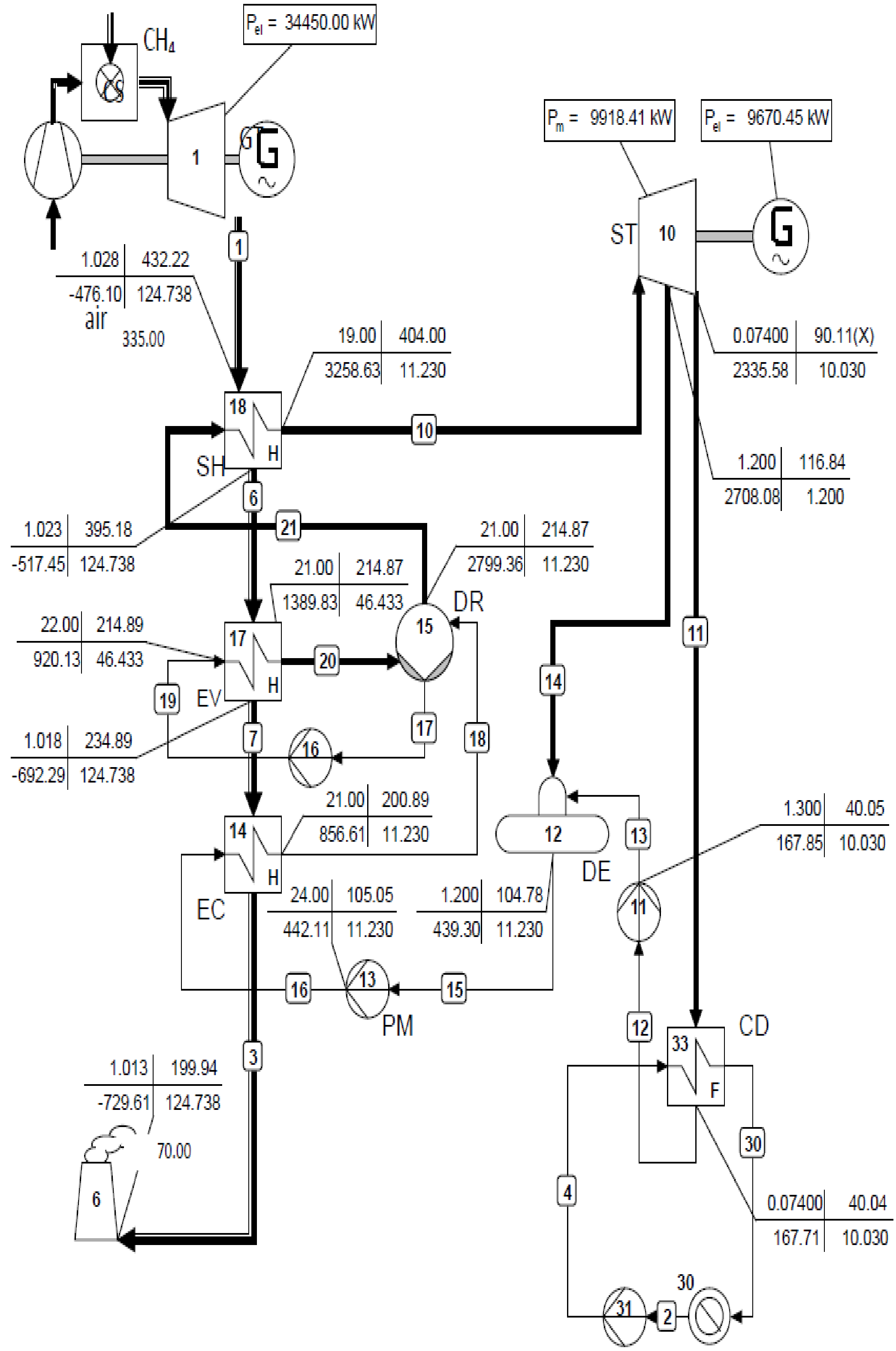

Figure 15: Steam Turbine based on SBC cycle [13]

Chapter 3. Methodology (Model Configurations and Mathematical Model)

Two models without compressed air energy storage (CAES) technology are presented with the mathematical model of each component. Another two models with (CAES) technology are presented at chapter 4 to improve the performance of the system.

3.1. Proposed Configurations

Figure 16 displays the first model which is a simple hybrid gas turbine cycle configuration (HGT) with integration of PTSC technology for air preheating in the topping gas turbine cycle. Ambient air is drawn into the topping cycle compressor (1) where it is compressed adiabatically (1-2). After compression, air enters the parabolic trough where it is preheated with the available solar flux at the receiver (2-3). Next, air goes through the combustion chamber and heat is added to the air fuel mixture in an isobaric process (3-4). In the next stage, flue gases departing the combustion chamber are expanded adiabatically in the gas turbine for power generation through generators.

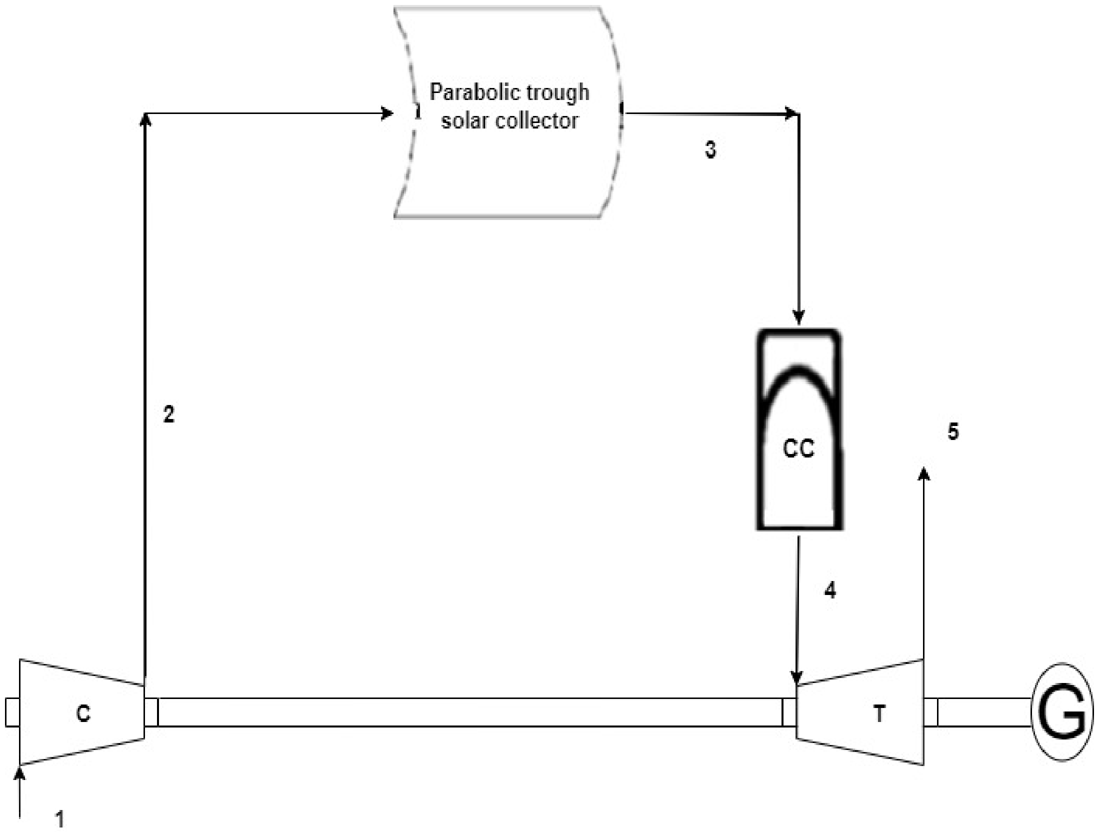

Figure 16: Simple hybrid gas turbine cycle configuration (HGT)

The second model concept shown in Figure 17, conceived for hybrid-solar applications, integrates an air-based bottoming cycle (ABHGT). A process flow diagram of this cycle is shown in Figure 17. The top Brayton cycle and the solar system in this model are similar to those of the hybrid solar gas-turbine power plant with a combined cycle. The bottoming cycle on the other hand, is replaced by a low-temperature intercooled-recuperated gas-turbine cycle similar to the one described in Figure 13. For this reason, the concept is called air-based bottoming cycle for hybrid gas-turbine power plant (ABHGT). In the top cycle, Ambient air is drawn into the topping cycle compressor (1) where it is compressed adiabatically (1-2). After compression, air enters the parabolic trough where it is preheated with the available solar flux at the receiver (2-3). Next, air goes through the combustion chamber and heat is added to the air fuel mixture in an isobaric process (3-4). In the next stage, flue gases departing the combustion chamber are expanded adiabatically in the gas turbine for power generation (4-5). Exhaust gases from the topping gas turbine go through the air heat exchanger where a portion of the available waste heat is recovered by the bottoming cycle air flow (5-6). In the bottoming cycle, ambient air is drawn into the bottoming cycle compressor (7) and it is compressed adiabatically (7-8). It is then intercooled through an intercooler and enters the high-pressure compressor (9-10). Afterwards, it is heated up successively by heat exchanged with exhaust air from the topping and bottoming turbines through waste heat recovery and recuperator respectively (10-11). It is finally expanded in the turbine and cooled down in the recuperator (11-12).

3.2. Mathematical Model

3.2.1 Parabolic trough solar collector (PTSC). In this section, the Parabolic trough solar collector (PTSC) mathematical modeling will be illustrated based on energy and exergy analysis. The PTSC main parts as shown in Figure 18 are the collector, receiver (absorber tube) and glass cover. The collector has a parabola shape which plays as reflective surface for parallel rays to be reflected on to the receiver.

The receiver consists of a black meal tube that is painted on black to absorb more heat than it reflects. To be able to reduce the heat loss through radiation and convection glass cover is used to cover the receiver and overcome these losses [41].

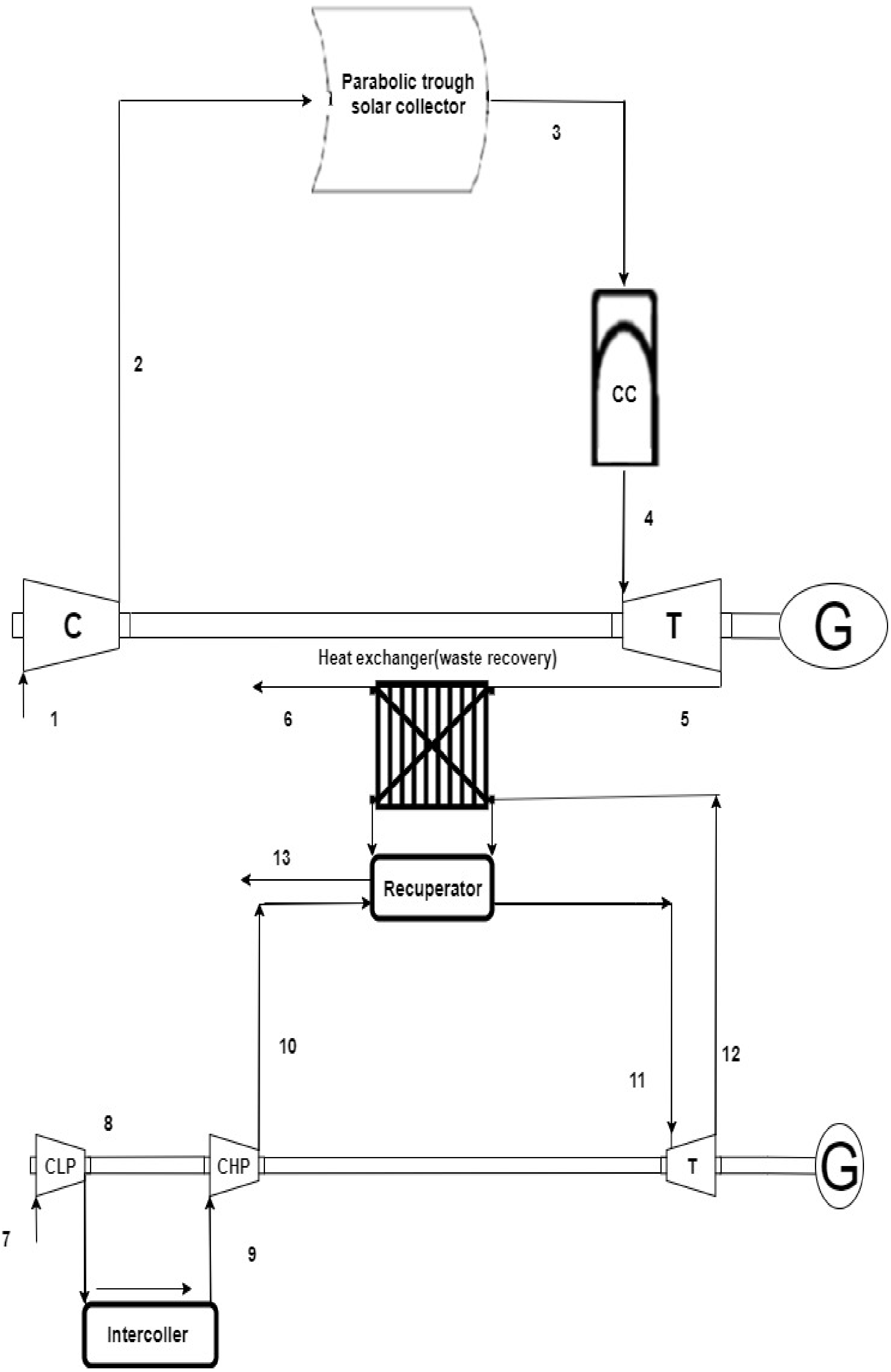

Figure 17: Model of gas Turbine using low temperature intercooled recuperated air bottoming cycle (ABHGT)

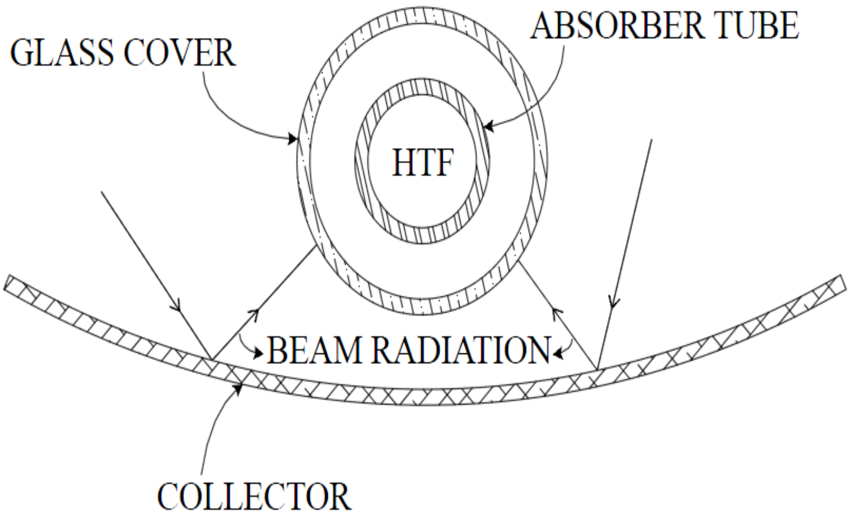

Figure 18: Parabolic trough solar collector schematic diagram [42]

Starting with modelling the collector output which is the useful energy output that is collected from the collector. It can be noticed that the radiation reflected by the collector surface had some losses since the receiver (absorber tube) is located away from it, which leads to a decrease on the radiation concentration. Thus, the difference between heat absorbed by heat transfer fluid and the indirect or direct loses represent the useful energy rate $\dot{Q}_u$ in (W) that is produced by the parabolic trough solar collector (PTSC). The useful energy rate $\dot{Q}_u$ can be Calculated [3].

$$\dot{Q}_u = F_r(I_b A_a - A_r U_l(T_i - T_{amb})) \tag{9}$$

where (T_{amb}) is the ambient temperature of the surrounding in K, (T_i) is the inlet temperature in K ,(Fr) is the heat removal factor, (A_a) is the aperture area in (m^2), (I_b) is the beam radiation in (W/m^2) , (A_r) is the receiver surface area in (m^2), and (U_l) is the overall heat loss coefficient [43].

To be able to calculate this useful energy rate ($\dot{Q}_u$), All useful energy rate variables needed to be known. Therefore, analysing each variable is needed to be able to calculate $\dot{Q}_u$. The aperture area, the receiver area and the beam radiation can be calculated by the below equation [3]:

$$\mathrm{A_a} = (\mathrm{w} - \mathrm{D_{co}})\mathrm{L_{para}} \tag{10}$$

$$\mathrm{A_r} = \pi(\mathrm{D_{ro}}\mathrm{L_{para}}) \tag{11}$$

$$I_b = I_d \eta_r \tag{12}$$

where (w) is the collector width, (D_{co}) is the outer diameter of the glass cover in (m), (L) is collector length in (m), (D_{ro}) is the outer diameter of the pipe receiver in (m), (I_d) is the direct radiation in (W/m^2) and (η_r) is the efficiency of the receiver[44].

Moving on to other variable, which is the overall heat loss coefficient (U_l) in ($w/m^2.k$) that depends on several variables listed on the below equation [3]:

$$U_l = \left[\frac{A_r}{(h_{cca}+h_{rca})A_c} + \frac{1}{h_{rcr}}\right]^{-1} \tag{13}$$

where (A_c) is the glass cover area in (m^2), (h_{cca}) is the convection heat transfer coefficient in ($w/m^2.k$), (h_{rca}) is the radiation heat transfer coefficient between the ambient and the glass cover in ($w/m^2.k$) and (h_{rcr}) is the radiation heat transfer coefficient between the receiver and the glass cover in ($w/m^2.k$)[45]. To be able to calculate the overall heat loss coefficient (A_c), (h_{cca}), (h_{rca}) and (h_{rcr}) need to be calculated. These variables can be computed using the below equations [3]:

$$h_{cca} = \frac{Nu_c k_{air}}{D_{co}} \tag{14}$$

$$A_c = \pi(D_{co} L_{para}) \tag{15}$$

where (Nu_c) is the Nusselt number, (k_{air}) is the thermal conductivity of air in $\left(\frac{W}{m\,K}\right)$

$$h_{rca} = \varepsilon_c \sigma (T_c + T_{amb})\left({T_c}^2 + {T_{amb}}^2\right) \tag{16}$$

where, (σ) is the Stefan-Boltzmann constant in $\left(\frac{W}{m^2\,K^4}\right)$,(ε_c) is the glass cover emissivity, (T_c) is the glass cover temperature in (K)[3]:

$$h_{rcr} = \frac{\sigma(T_c+T_r)+\left({T_c}^2+{T_r}^2\right)}{\left(\frac{1}{\varepsilon_r}+\frac{A_r}{A_c}\right)+\left(\frac{1}{\varepsilon_c}-1\right)} \tag{17}$$

where (Tr) is the receiver temperature in K and (ε_r) is the emissivity of the receiver. The Nusselt number (Nu_c) is computed using the below equation which depends on the (Re) Reynolds number as the air around solar collector could be laminar or turbulent. knowing the Reynolds number is essential to be able to calculate $\dot{Q}_u$ [3]:

$$Nu_c = 0.4 + 0.54(Re)^{0.6} \tag{18}$$

where the Re is computed using the following equation [3].

$$Re = \frac{V_{wind} D_{co}}{v_{air}} \tag{19}$$

where (V_{wind}) is the wind velocity in (m/s) and (v_{air}) in (m^2/s) is the kinematic viscosity of the air.

Knowing the properties of air at a mean temperature which is found using $T_m = \frac{T_{amb}+T_c}{2}$, the Reynolds number is calculated, and the flow is computed to be turbulent as Re>4000. After finding the Reynolds number the nusselt number (Nu_c) is easily computed. By getting the (Nu_c), the (h_{cca}) is calculated. By getting all these values the overall heat loss coefficient is computed [3].

To continue computing ($\dot{Q}_u$), one variable is left to calculate which is the (F_r). To be able to calculate (Fr) the following equation is used [3]:

$$F_r = \dot{m}_{air} \frac{C_{pair}}{A_r U_l} \left[1 - e^{\left(-\frac{A_r U_l F}{\dot{m}_{air} C_{pair}} \right)} \right] \tag{20}$$

where ($\dot{m}_{air}$) is the mass flow rate of air in the receiver tube, (C_{pair}) is the heat capacity of the air and (F) is the collector efficiency factor [3,46].The collector efficiency factor can be computed using the following equation:

$$F = \frac{U_o}{U_l} \tag{21}$$

where (U_o) is the overall heat coefficient in (W/m^2.k), which is calculated by the equation below [3]:

$$U_o = \left[\left(\frac{1}{U_l} + \frac{D_{ro}}{h_{crin} D_{ri}} + \frac{D_{ro}}{2K_r} \right) ln \left(\frac{D_{ro}}{D_{ri}} \right) \right]^{-1} \tag{22}$$

where (Kr) is the receiver thermal conductivity, (h_{crin}) is the convection heat transfer coefficient that occurs inside the receiver tube and the (D_{ri}) is inside diameter of the receiver [3,47].

The (h_{crin}) in (W/m^2.k) is computed using the general equation below.

$$h_{crin} = \frac{Nu_{sr} K_r}{D_{ri}} \tag{23}$$

The Nusselt number in the overall heat coefficient formula for turbulent flow is computed as shown below [3,48]:

$$Nu_{sr} = 0.023 {Re_r}^{0.8} {Pr_r}^{0.4} \tag{24}$$

where Prandtl number (Pr_r= 0.687) and to be able to compute the Nusselt number, Reynolds number (Re_r) need to be calculated first which is given by following equation [3]:

$$Re_r = \frac{\rho_{air} V_{wind} D_{ri}}{\mu_{air}} \tag{25}$$

where (μ_{air}) which is the dynamic viscosity of air in (kg/m.s) and the (ρ_{air}) which is the air density in (kg/m^3), (V_{wind}) is the wind velocity in (m/s).

Finally, by obtaining all the required variables for F, the collector efficiency factor (F) can be computed. As the last variable (F) is known the useful energy ($\dot{Q}_u$) can be calculated. After computing $\dot{Q}_u$, the overall efficiency of the parabolic trough solar collector (η_{PTSC}) can be computed by the ratio of the useful energy rate to the total energy received from the sun as shown for the equation below [3,49].

$$\eta_{PTSC} = \frac{\dot{Q}_u}{\mathrm{A_a I_b}} \tag{26}$$

The outlet temperature ($\mathrm{T_0}$) in (K) at the end of the tube can be also computed by the equation below [3]:

$$\mathrm{T_0} = T_\mathrm{i} + \frac{\dot{Q}_u}{(\dot{\mathrm{m}}_{air}) C_{pair}} \tag{27}$$

to calculate the useful energy rate ($\dot{Q}_{utotal}$) needed, the number of parabolic troughs (N_{PTSC}) is essential to be considered [3,50].

$$N_{PTSC} = \frac{134}{\dot{\mathrm{m}}_{air}} \tag{28}$$

$$\dot{Q}_{utotal} = N_{PTSC} \dot{Q}_u \tag{29}$$

The exergy efficiency is defined as the ratio of the output exergy to the input exergy. In case of the parabolic trough solar collector, the exergy output ($\dot{X}_{out,PTSC}$) is the exergy that is stored by the heat transfer fluid (air) that passes through the receiver tube, while the exergy input ($\dot{X}_{in,PTSC}$) is the exergy of the solar radiation absorbed by collector inside the PTSC [3,51].

$$\eta_{ec,PTSC} = \frac{\dot{X}_{out,PTSC}}{\dot{X}_{in,PTSC}} \tag{30}$$

$$\dot{X}_{out,PTSC} = \dot{Q}_{utotal} \left(1 - \frac{\mathrm{T}_{amb}}{\mathrm{T}_r}\right) \tag{31}$$

$$\dot{X}_{in,PTSC} = I_b A_a \left[1 + \frac{1}{3}\left(\frac{\mathrm{T}_{amb}}{\mathrm{T}_S}\right)^4 - \frac{4}{3}\left(\frac{\mathrm{T}_{amb}}{\mathrm{T}_S}\right)\right] \tag{32}$$

where exergy destruction $\dot{X}_{des,PTSC}$ is the difference between $(\dot{X}_{in,PTSC})$ and $(\dot{X}_{out,PTSC})$.

Exergy destruction can be calculated by the following equation.

$$\dot{X}_{des,PTSC} = (\dot{X}_{in,PTSC}) - (\dot{X}_{out,PTSC}) \quad (33)$$

3.2.2. Gas turbine models for ABHGT and HGT.

3.2.2.1. Compressor. For the Proposed configurations, the first model includes one compressor for the topping cycle and the other model include three compressors for topping and bottoming cycles. The working fluid on these compressors is air. Their pressure ratios rely on the specified topping and bottoming cycle compression ratios. The compressor's specific work and outlet temperature are calculated based on these equations [1,52]:

$$s_{c,o} = s_{c,i} + Rln(r_c) \quad (34)$$

$$s_{c,o} \rightarrow T_{sc,o} \quad (35)$$

$$T_{c,o} = T_{c,i} + \frac{T_{sc,o} - T_{c,i}}{\eta_{c}} \quad (36)$$

$$W_c = \frac{C_{p,avg}(T_{c,o} - T_{c,i})}{\eta_M} \quad (37)$$

where $s_{c,o}$ and $s_{c,i}$ represent the isentropic outlet and inlet entropies of the compressor in kJ/kg.K, r_c is the compressor pressure ratio. $T_{c,i}$ is the compressor air inlet temperature in K, $T_{c,o}$ and $T_{sc,o}$ and are the outlet actual and isentropic air temperature at the compressor in K, $C_{p,avg}$ is the compressor specific heat capacity for average temperatures in kJ/kg.K, η_{c} is the isentropic efficiency of the compressor , η_M is the mechanical efficiency, and W_c is the compressor required specific work input in kJ/kg.

3.2.2.2. Turbine. For the Proposed configurations, the first model includes one Turbine for the topping cycle.

The other model include two turbines for topping and bottoming cycles with different gas pressure ratios. Accordingly, full attention should be given to different specific and working fluid properties calculation. A turbine's specific work output and outlet temperature are calculated based on these equations [1,53].

$$s_{t,o} = s_{t,i} + Rln(r_t) \quad (38)$$

$$s_{t,o} \rightarrow T_{st,o} \quad (39)$$

$$T_{t,o} = T_{t,i} + \eta_t(T_{t,i} - T_{st,o}) \quad (40)$$

$$w_t = \frac{C_{pavg}(T_{t,i} - T_{t,o})}{\eta_M} \quad (41)$$

where $s_{t,o}$ and $s_{t,i}$ represent the isentropic outlet `and inlet entropies of the turbine in kJ/kg.K, r_t is the turbine pressure ratio. $T_{t,i}$ is the turbine air inlet temperature in K, $T_{t,o}$ and $T_{st,o}$ and are the outlet actual and isentropic air temperature at the turbine in K, $C_{p,avg}$ is the turbine specific heat capacity for average temperatures in kJ/kg.K, η_t is the isentropic efficiency of the turbine , η_M is the mechanical efficiency, and W_t is the turbine work output in kJ/kg[1].

3.2.2.3. Combustion chamber. In the combustion chamber, different fuels can be used for combustion purposes. The aiming turbine inlet temperature (TIT) can be achieved through the required fuel and exhaust gases mass flow rates, and the heat rate supplied to the combustion chamber through the below equations [1,54].

$$\dot{m}_f = \frac{\dot{m}_a c_{pg,avg}(T_{o,cc} - T_{ref}) - \dot{m}_a c_{pa,avg}(-T_{ref})}{\eta_{cc}\Delta hi^{\circ}_{fuel} - c_{pg,avg}(T_{o,cc} - T_{ref})} \quad (42)$$

$$\dot{m}_g = \dot{m}_a + \dot{m}_f \quad (43)$$

$$\dot{Q}_{comb}{}^{+} = \dot{m}_f \Delta hi^{\circ}_{fuel} \quad (44)$$

The exergy rate ($\dot{E}_{q,fuel}{}^{+}$) from the fuel can be obtained from the equation below [2]:

$$\dot{E}_{q,fuel}{}^{+} = \dot{m}_f \Delta k^{\circ}_{fuel} \quad (45)$$

where $\dot{m}_a$, $\dot{m}_f$, and $\dot{m}_g$, are air mass , fuel, and exhaust gases flow rates respectively in kg/s, $c_{pg,avg}$ and $c_{pa,avg}$ are gas and air average specific heat capacities, $T_{o,cc}$ and $T_{i,cc}$ are outlet and inlet temperatures at the combustion chamber in K , $Tref$ illustrates the reference temperature state that is associated with the LHV of the fuel in K , η_{cc} is the combustion chamber efficiency, Δhi°_{fuel} is the specific lower heating value of the fuel in kJ/kg, $\dot{Q}_{comb}{}^{+}$ is the heat rate supplied to the combustion chamber and, Δk°_{fuel} is the specif exergy of the fuel in kJ/kg .

3.2.2.4. Heat Exchanger and intercooler fan. ABHGT model has an air to air heat exchanger. It consists from three main parts which are waste heat recovery, intercooler, and recuperator.

Heat waste recovery and recuperator are responsible for heat transfer (exhaust gasses) from topping cycle to the bottoming cycle. The most significant design factors in heat exchanger are low pressure drop and heat exchanger effectiveness [55]. Low density and high temperature of gases complicate the design procedure. As the heat exchanger effectiveness (ε) is selected, the outlet heat exchanger temperature of cold and hot sides can be calculated. In order to maximize the heat exchanger heat transfer with minimum exergy loses, the temperature variance between cold and hot fluids should be constant equal to a constant value point. This point is called the pinch point, where $\Delta T_{\min} = \Delta T_{\text{pinch}}$. The air heat exchanger can be modeled by the below equations [2]:

$$\varepsilon = 1 - \frac{\Delta T_{\min}}{(T_{i,H} - T_{i,L})} \tag{46}$$

$$T_{o,L} = T_{i,H} \pm \Delta T_{\text{pinch}} \tag{47}$$

$$T_{o,H} = T_{i,H} - \frac{\dot{m}c_{p,L}(T_{o,L} - T_{i,L})}{\dot{m}c_{p,H}} \tag{48}$$

where (ε) is the heat exchanger effectiveness. $T_{o,L}$ and $T_{i,L}$ are the lower heat capacity stream outlet and inlet temperatures on the heat exchanger in K, $T_{o,H}$, and $T_{i,H}$ are the higher heat capacity stream outlet and inlet temperatures on the heat exchanger in K, $\dot{m}c_{p,L}$ and $\dot{m}c_{p,H}$ are lower and higher stream heat capacities in kJ/K, and $\Delta Tpinch$ is the pinch temperature which is the minimum difference temperature between the hot and cold streams in K. By reducing ΔT_{pinch} , exergy losses are reduced however the area (A) and the cost of the heat exchanger will increase. The heat exchanger pressure loss can be expressed by the output pressure equation and an electric fan is needed for the intercooler to blow the air and cool it down [2]:

$$p_{out} = p_{in}\left(1 - f_{\Delta P_{he}}\right) \tag{49}$$

$$e_{fan}^{+} = \frac{f_{\Delta P_{IC}} p_{atm}}{\rho_{air} \eta_{fan} \eta_{ele}} \tag{50}$$

where e_{fan}^{+} is the specific power of the intercooler fan in kw/kg, $f_{\Delta P_{he}}$and p_{in} are specific pressure drop and inlet pressure in the heat exchanger, $f_{\Delta P_{IC}}$ is specific pressure drop in the intercooler, p_{atm} is the atmospheric pressure, ρ_{air} is the air density, η_{ele} , and η_{fan} are the electric and fan efficiencies respectively.

3.2.2.5. Plant performance for ABHGT and HGT. plant performance of ABHGT can be calculated by connecting the bottoming to topping cycle. New parameter is called mass flow ratio which is referred to the bottoming cycle mass flow rate over the topping cycle flow rate [1]:

$$MFRR = \frac{\dot{m}_{a,B}}{\dot{m}_{a,T}} \tag{51}$$

where $\dot{m}_{a,B}$, $\dot{m}_{a,T}$ are the botting and topping cycles mass flow rate in kg/s.

Net power output and overall energy and exergy efficiencies of the HGT model:

$$\dot{W}_{net,HGT} = \left[\eta_{M,G}(\dot{m}_g w_{tT}) - \frac{(\dot{m}_{aT} w_{cT})}{\eta_{M,G}}\right]\eta_{ele,G} \tag{52}$$

$$\varepsilon_{HGT} = \frac{\dot{W}_{net,HGT}}{\dot{Q}_{comb}{}^{+} + \dot{Q}_{sol}} \tag{53}$$

$$\eta_{HGT} = \frac{\dot{W}_{net,HGT}}{\dot{E}_{q,fuel}{}^{+} + \dot{X}_{des,PTSC}} \tag{54}$$

Net power output and overall energy and exergy efficiencies of the ABHGT model:

$$\dot{W}_{net,ABHGT} = \left[\eta_{\mathbf{M,G}}(\dot{m}_g w_{tT} + \dot{m}_{aB} w_{tB}) - \frac{(\dot{m}_{aT} w_{cT} + \dot{m}_{aB} w_{1cB} + \dot{m}_{aB} w_{2cB})}{\eta_{M,G}}\right]\eta_{ele,G} \tag{55}$$

$$\varepsilon_{ABHGT} = \frac{\dot{W}_{net,ABHGT}}{\dot{Q}_{comb}{}^{+} + \dot{Q}_{sol}} \tag{56}$$

$$\eta_{ABHGT} = \frac{\dot{W}_{net,ABGHT}}{\dot{E}_{q,fuel}{}^{+} + \dot{X}_{des,PTSC}} \tag{57}$$

where w_{cT} and w_{tT} are the topping cycle compressor and turbine specific work in kJ/kg, likewise, w_{1cB}, w_{2cB}, and w_{tB} are the bottoming cycle first compressor ,second corepressor and turbine specific works in kJ/kg, $\eta_{M,G}$, and $\eta_{ele,G}$, are the mechanical and electrical efficiencies, $\dot{Q}_{sol}$ is the solar thermal rate input (useful power) in kW,$\dot{Q}_{comb}$ is the heat rate supplied to the combustion chamber in KW $\dot{E}_{q,fuel}{}^{+}$ is the fuel exergy rate in KW, $\dot{X}_{des,PTSC}$ is the PTSC distraction exergy rate in KW , $\dot{W}_{net,HGT}$ and $\dot{W}_{net,ABHGT}$ are the ABHGT and HGT total net power output in kW, ε and η are the overall energy and exergy efficiency of the plant.

3.3. Economic Model

Economic model analysis gives a better overview of ABHGT and HGT power plants. The most efficient power plant design isn't really the most cost competitor. Hence, cost evaluation and economic analysis are demonstrated. A mathematical model for economic analysis of each component on ABHGT and HGT is illustrated on this section. Given that the mathematical model for economic are gotten from different publishers with different publication dates. To improve the accuracy of the economic model, chemical engineering plant cost index (CEPCI) is used to account for inflation on equipment cost. Each component is multiplied by this index factor which is illustrated by the below equation below [1].

$$f_{CEPCI} = \frac{CEPCI_{2018}}{CEPCI_{ref}} \tag{58}$$

3.3.1. Compressor. The economic mathematical model for the air compressors that is used in the gas turbine topping and bottoming cycle [1]:

$$Z_c = \left(\frac{39.5\dot{m}_{a,c} r_c}{0.9-\eta_c}\right) ln(r_c) \tag{59}$$

where $\dot{m}_{a,c}$ is the air mass flow rate of the compressor in (kg/s), r_c is the compressor pressure ratio, η_c is the isentropic efficiency of the compressor and Z_c is the compressor capital cost in US $.

3.3.2. Turbine. The economic mathematical model for the gas Turbine that is used in the gas turbine topping and bottoming cycle [1]:

$$Z_{Gt} = \left(\frac{266.3\dot{m}_t}{0.92-\eta_t}\right) ln\left(\frac{1}{r_t}\right)\left[1 + exp\left(0.036T_{t,i} - 54.4\right)\right] \tag{60}$$

where $\dot{m}_t$ is the mass flow rate passing through the Turbine in (kg/s), r_t is the turbine pressure ratio.

η_t is the isentropic efficiency of the turbine, $T_{t,i}$ is the turbine inlet temperature and $Z_{G,t}$ is the gas turbine capital cost in US $.

3.3.3. Combustion chamber. The economic mathematical model for the Combustion chamber that is used in the gas turbine topping cycle [1]:

$$Z_{cc} = \left(\frac{25.6\dot{m}_{a,T}}{0.995 - \frac{P_{o,cc}}{P_{i,cc}}}\right)\left[1 + exp\left(0.018T_{o,cc} - 26.4\right)\right] \tag{61}$$

where $\dot{m}_{a,T}$ are the topping cycle mass flow rate in (kg/s), $P_{o,cc}$, $P_{i,cc}$ are the exhaust gases pressure at the combustion chamber exit and the air pressure at the combustion chamber entry in (KPa), Z_{cc} is the combustion chamber capital cost in US \$.

3.3.4. Air heat exchanger. The economic mathematical model for the air heat exchanger that is used in the gas turbine topping and bottoming cycle [2]:

$$Z_{AHX} = f_{BM}\left(10^{K_1 + K_2 \log(A) + K_3 (logA)^2}\right) \tag{62}$$

where f_{BM} is instillation of equipment bare module factor, A is the area of air heat exchanger in m^2, K_1,K_2,K_3 are heat exchanger constants.

The bare module factor can be illustrated by the below equation [2]:

$$f_{BM} = B_1 + \left(B_2 f_m f_p\right) \tag{63}$$

where f_p is the pressure factor, f_m is the material factor, B_1,and B_2 are heat exchanger constant coefficients.

The pressure factor can be determined by the following equation [2]:

$$f_p = 10^{C_1 + C_2 \log(P - P_a) + C_3 (\log(P - P_a))^2} \tag{64}$$

where $(P - P_a)$ is the operating pressure change of the heat exchanger,C_1, C_2, C_3 are heat exchanger constant coefficients.

The material factor can be expressed by the below equation [2]:

$$f_m = \left(\frac{T_{h_i}}{623}\right)^{2.4} \tag{65}$$

where T_{h_i} is the hot fluid inlet temperature in (K) of the heat exchanger. It can be noticed from Table 7 that waste heat and recuperate are modeled as Flat plate heat exchanger whereas the intercooler is modeled as Air cooler.

Table 7: Heat exchanger constant coefficients [2].

Exchanger Type	K_1	K_2	K_3	C_1	C_2	C_3	B_1	B_2
Air cooler	3.6418	0.4053	0	-0.06154	0.0473	0	1.53	1.27
Flat plate	3.8528	0.4242	0	0	0	0	1.53	1.27

Hence, evaluating constant coefficients to the main economic mathematical model for air heat exchanger lead to the simplified expression below [2].

$$Z_{AHX} = 1.53 + 1.27\left(\frac{T_{h_i}}{623}\right)^{2.4}\left(10^{3.8528+0.4242\log(A)}\right) \tag{66}$$

3.3.5. Intercooler fan. The economic mathematical model for the Intercooler fan that is used in the gas turbine bottoming cycle [2].

$$Z_{IC} = f_{BM}\left(10^{K_1+K_2\log(\dot{V}_{IC})+K_3(log\dot{V}_{IC})^2}\right) \tag{67}$$

Where $\dot{V}_{IC}$ is the volumetric flow rate of the intercooler fan in (m^3/s).

$$f_{BM} = f_m f_p \tag{68}$$

Therefore, evaluating constant coefficients, shown in Table 8, to the main economic mathematical model for Intercooler fan lead to the simplified expression below [2].

$$Z_{AHX} = 2.86\left(\frac{T_{h_i}}{623}\right)^{2.4}\left(10^{2.9471+0.3302\log(\dot{V}_{IC})+0.1969(log\dot{V}_{IC})^2}\right) \tag{69}$$

Table 8: Intercooler fan constant coefficients [2].

Fan Type	K_1	K_2	K_3	f_m	f_p
Axial Vane	2.9471	0.3302	0.1969	2.2	1.3

3.3.6. PTSC field. The economic mathematical model for the PTSC field that is used as a solar power at the gas turbine bottoming cycle, is divided to three parts which are PTSC solar field cost, thermal energy storage system and heat transfer fluid (HTF) cost.

However, the ABHGT and HGT models don’t have energy storage systems and the HTF cost is neglected since air is used as heat transfer fluid. The economic mathematical model for the PTSC is obtained from the National Renewable Energy Laboratory [3].

$$Z_{PTSC} = A_{SA}C_{PTSC} + \dot{Q}_{tank}C_{TES} + A_{SA}C_{HTF} \tag{70}$$

The simplified economic mathematical model form after neglecting the energy storage systems and HTF cost [3].

$$Z_{PTSC} = A_{SA}C_{PTSC} \tag{71}$$

Where A_{SA} , is the PTSC aperture area in (m^2) and C_{PTSC} is the PTSC fixed cost that equal to 245 $\left(\frac{\text{US \$}}{\text{m2}}\right)$.

3.3.7. Generator and auxiliary equipment. The economic mathematical model for the generator and its auxiliary equipment's that are used in the gas turbine topping and bottoming cycle [1,55].

$$Z_G = 6 \times 10^6 \left(\frac{\dot{W}_{net}}{\dot{W}_{net,ref}}\right)^{0.7} + Z_{G,aux} \tag{72}$$

$$Z_{G,aux=} 4 \times 10^6 \left(\frac{\dot{W}_{net}}{\dot{W}_{net,ref}}\right)^{0.7} \tag{73}$$

Where Z_G, $Z_{G,aux}$ are the capital cost of the generator and its auxiliary equipment in US \$, $\dot{W}_{net}$ is the net power output of the cycle in (MW). $\dot{W}_{net,ref}$ is the reference nominal power output which is equal to 160 (MW). Hence, the simplified economic mathematical model of the generator and its auxiliary equipment can be defined as:

$$Z_G = 6 \times 10^6 \left(\frac{\dot{W}_{net}}{160}\right)^{0.7} + 4 \times 10^6 \left(\frac{\dot{W}_{net}}{160}\right)^{0.7} \tag{74}$$

3.3.8. Civil engineering. The capital project cost required for a new building and site infrastructure for ABHGT and HGT needed to be taken in consideration. Hence, the economic mathematical model for civil engineering can be calculated by the below equation [1,56]:

$$Z_{Civil} = 7.6 \times 10^6 \left(\frac{\dot{W}_{net}}{52.8}\right)^{0.8} \tag{75}$$

where $ZCivil$ is the civil engineering capital cost in US \$ and $\dot{W}_{net}$, net power output of the cycle in (MW). However, ABHGT civil engineering capital cost is doubled.

3.3.9. Fuel network branching. Natural gas or LPG is required to be carried out to the power plant by a new pipeline branch that connects the high-pressure gas network to the power plant. Therefore, the total capital cost of branch station needed for the fuel gas delivery to the combustor through the pipeline [1,57]:

$$Z_{Branch} = 1.3 \times 10^6 \left(\frac{\dot{m}_{fuel}}{14.4}\right)^{0.8} \tag{76}$$

where Z_{Branch} is the branch station capital cost in US \$ and $\dot{m}_{fuel}$ is fuel mass flow rate in kg/s.

3.3.10. Miscellaneous equipment. ABHGT and HGT power plants have miscellaneous equipment that consist of control systems, auxiliary equipment, and transforms. The cost function of miscellaneous equipment can be expressed by the below equation [1,58]:

$$Z_{mis} = 7.6 \times 10^6 \left(\frac{\dot{W}_{net}}{52.8}\right)^{0.7} \tag{77}$$

where Z_{mis} is the miscellaneous equipment capital cost in US \$.

3.3.11. Overall gas turbine cost. Topping and bottoming gas turbine cost can be calculated by the following equations:

$$Z_{GT,t} = Z_c + Z_{Gt} + Z_{cc} + Z_G \tag{78}$$

$$Z_{GT,b} = 2 \times Z_c + Z_{Gt} + Z_G \tag{79}$$

where $Z_{GT,t}$ and $Z_{GT,b}$ are the topping and bottoming overall gas turbine cost in US \$.

3.3.12. Total additional cost. The total additional cost of ABHGT and HGT can be calculated by the following equation:

$$Z_{add} = Z_{AHX} + Z_{IC} + Z_{Civil} + Z_{branch} + Z_{mis} \tag{80}$$

where Z_{add} is the total additional cost in US \$.

3.3.13. Project contingencies. Occurrence of unexpected technical difficulties during in the regulation of construction process could result in additional capital cost.

Additional costs associated with the aforementioned factors can be expressed by contingency factor $f_{cont} = 1.1$ [2].

3.3.14. Total capital cost. The total capital cost can be calculated by the addition of overall gas turbine cost, PTSC field cost, total additional cost multiplied by both the inflation and contingency factor. In conclusion, the total cost can be expressed by the following equation [2]:

$$Z_{TCC} = \left(Z_{GT,t} + Z_{GT,b} + Z_{PTSC} + Z_{add}\right) f_{cont} f_{\mathrm{CEPCI}} \quad (81)$$

where Z_{TCC} is the total capital cost in US $.

3.3.15. Decommissioning. Dismantling, replacing and restoring the site of the power plant by the end of its lifetime are the main concerns for a sustainable development. Hence, 5 percent of the total capital is counted as a decommissioning cost. Furthermore, decommissioning costs can be calculated by the following equation [1]:

$$Z_{dec} = 0.05(Z_{TCC}) \quad (82)$$

where Z_{dec} is the decommissioning cost in US $.

3.3.16. Operation and maintenance costs. Operation and maintenance costs are vital aspects in accounting for economic model of ABHGT and HGT.

Operation and maintenance costs consist of fuel and water consumption costs, repairs and spare parts costs, service contracts and labor costs [58].

3.3.16.1. Fuel and water consumption. Annual fuel cost can be expressed by the following equation [2]:

$$Z_{fuel} = c_{fuel} \dot{m}_f \Delta k^{\circ}{}_{fuel} \quad (83)$$

where c_{fuel} is the specific fuel cost in $\frac{\text{US \$}}{MWh}$ .The water consumption in ABHGT and HGT can be divvied to two main sources which are water consumption associated with mirror washing from the PTSC components and compressor washing. water consumption of mirror washing can be expressed by the following equation [2,59]:

$$V_{w,mw} = 0.05 A_{PTSC} N_{PTSC} \quad (84)$$

where $V_{w,mw}$ is water consumption of mirror washing in m^3. The water consumption of compressor washing can be calculated by the following equation [2]:

$$V_{w,cw} = 365\left[0.09 + 0.0005\dot{m}_{a,c}\right] \tag{85}$$

where $V_{w,cw}$ is the water consumption of compressor in m^3. The water annual cost of ABHGT plant can be expressed by the following equation [2,60]:

$$Z_{water} = c_{water}\left(V_{w,cw} + V_{w,mw} + 2 \times V_{w,cw}\right) \tag{86}$$

where Z_{water} is the annual cost of water consumption of ABHGT in US $, c_{water} is the specific water price which is about 1.2 $\frac{\text{US \$}}{m^3}$.

3.3.16.2. Repairs and spare parts. The repairs are spare parts need to be taken in account while calculating the power plant investment.

The turbomachinery components spare parts and repairs costs are assumed to be 2% of the total capital cost. Moreover, PTSC components spare parts and repairs costs are calculated to be 3% of the total capital cost. Furthermore, fuel network branching, and civil engineering cost are expressed by 1 % of the total capital cost [1,61].

3.3.16.3. Labor cost. To enhance the accuracy of the economic model, the power plant employees and managers need to be taken in consideration. The number of employees and managers with their corresponding salaries are shown in Table 9. The number of solar field technicians and control room operators can be calculated by the following equations (87,88). Three solar field technicians and two control room operators per 100000 m^2 of PTSC field are assumed [1,62]:

Table 9: Required labors with corresponding salaries [1]

Staff	**Salary US$/year**	**Required Employees**
Plant Manager	142000	0.25
Plant Engineer	92000	1
Maintenance supervisor	72000	1
Power block technician	60000	1
Solar field technician	50000	$Ntec$
Operation manager	125000	1
Control room operator	60000	$Nopr$

$$N_{tec} = \frac{3}{100000} A_{PTSC} N_{PTSC} \quad (87)$$

$$N_{opr} = \frac{2}{100000} A_{PTSC} N_{PTSC} \quad (88)$$

where N_{tec}, N_{opr} are the number of solar field technicians and control room operators.

3.3.16.4. Contracts services. The Contracts Services are essential factor to account for economic model of the power plant.

Three sets of contracts are needed for maintenance costs which are control system, mirror washing and ground keeping contracts. The control system contract fixed cost is 100000 $\frac{\text{US \$}}{year}$. The ground keeping and mirror washing contracts services costs can be calculated by the following equations [1,63]:

$$Z_{cs,gk} = 10^5 \left(\frac{A_{PTSC} N_{PTSC}}{854000}\right)^{0.5} \quad (89)$$

$$Z_{cs,mw} = 3.5 \times 10^5 \left(\frac{A_{PTSC} N_{PTSC}}{854000}\right)^{0.5} \quad (90)$$

where $Z_{cs,gk}$, $Z_{cs,mw}$ are the ground keeping and mirror washing contracts services costs in US $.

3.4. Plant Performance

Three indicators need to be taken in consideration to evaluate the plant performance, which are economic, environmental and thermodynamics indicators.

3.4.1. Economic indicators. One of the most popular economic indicators for power plants performance is the levelized cost of electricity (LCOE). LCOE is used to measure the cost of electricity produced. It can be also defined as the cost of electricity sale which makes the net present value (NPV) of the investment equal to zero. The investment of the project would be more profitable if the LCOE is lower. So, the LCOE of the power plant need to be less than the actual price of electricity sold to declare that the net present value is positive; and the investment is profitable.

Hence, there is clear internal relation between the LCOE and NPV. Nevertheless, electricity market is competitive and got affected by many factors such as fuel price and the power plant location. Levelized cost of electricity (LCOE) can be calculated by the following equation [1,2]:

$$LCOE = \frac{\alpha Z_{TCC} + \beta Z_{dec} + Z_{fuel} + Z_{O,M}}{\dot{W}_{net}} \tag{91}$$

where $Z_{TCC}, Z_{dec}, Z_{fuel}, Z_{O,M}$ are the total capital cost, decommissioning cost, fuel cost, and operation and maintenance cost in US \$. α and β are the capital cost and decommissioning recovery factors.

The total capital cost can be converted to a fixed cost by using the capital recovery cost α through using paid over the lifetime period of the investment [1,65]:

$$\alpha = \frac{r(1+r)^n}{(1+r)^n - 1} + r_{ins} \tag{92}$$

where r is the interest rate and r_{ins} is the annual insurance rate and n is life period of the investment.

The capital recovery cost α is used to transfer the decommissioning cost to fixed annual costs paid over the lifetime period of the investment [1].

$$\beta = \frac{r}{(1+r)^{n+1} - (1+r)} \tag{93}$$

Another popular economic indicator for power plants performance is the net present value (NPV). NPV is used to evaluate the investment potential by determining the investment growth over the lifetime period of the investment.

It can be also illustrated as the addition of all the cash flow over the lifetime period of the project. Accordingly, an investment is only profitable as long as the NPV is positive value, where positive cash flows (revenues) overcomes negative cash flows (investment total costs) [1].

Net present value (NPV) can expressed by the following equations [1,2].

$$NPV = -Z_{TCC}\left(1 + \frac{r_{ins}}{\alpha - r_{ins}}\right) - \frac{Z_{dec}}{(1+r)^{n+1}} + \sum_{t=1}^{n} \frac{R - Z_{O,M} - Z_{fuel}}{(1+r)^n} \tag{94}$$

Where R is the annual revenue obtained by the electricity sale.

The investment is worth taking if NPV is positive. Moreover, a zero NPV means that the investor not losing nor gaining revenue [2,67].

3.4.2. Environmental indicators. Reducing the CO_2 emissions is one of the main objectives in the current thesis. Reducing the CO_2 emission means less reliance on fossil fuel that has large impact on the climate change. The specific of $\mathrm{CO_2}$ amount per unit of electricity emitted by the plant $\left(f_{CO_2}\right)$ is one of the key factors to the environmental indicators.

The specific of $\mathrm{CO_2}$ amount per unit of electricity can be calculated by the following equation [2]:

$$f_{\mathrm{CO_2}} = \frac{44}{12}\left(\frac{c_c{}^{fuel}\dot{m}_f}{\dot{\mathrm{W}}_{\mathrm{net}}}\right) \tag{95}$$

where $c_c{}^{fuel}$ is the fuel carbon content, $\dot{m}_f$ is the fuel mass flow rate in (kg/s) and $\dot{\mathrm{W}}_{\mathrm{net}}$ is total power output of the plant in (MW).

One of the main objectives of using Brayton cycle combined with air bottoming cycle is that does not rely on water consumption. Hence, using ABHGT power plants requires less water consumption compared to other conventional power plants. One of the important factors is the specific water consumption per unit of electricity (f_{H_2O}) which can be illustrated by the below equation [2]:

$$f_{H_2O} = \frac{V_{water}}{\dot{\mathrm{W}}_{\mathrm{net}}} \tag{96}$$

where V_{water} is that total water consumption by the power plant in m^3.

3.4.3. Thermodynamic indicators. Overall energy and exergy efficiencies, PTSC solar share and the capacity factor of the power plant are the main core of the thermodynamic indicators [2].

Overall energy efficiencies of the power plant can be calculated by the below equation [1].

$$\varepsilon_{\mathrm{overall}} = \frac{\dot{\mathrm{W}}_{\mathrm{net}}}{\dot{Q}_{comb}{}^{+}+\dot{Q}_{sol}} \tag{97}$$

Overall exergy efficiencies of the power plant can be calculated by the below equation [1].

$$\eta_{\mathrm{overall}} = \frac{\dot{\mathrm{W}}_{\mathrm{net}}}{\dot{E}_{q,fuel}{}^{+}+\dot{X}_{des,PTSC}} \tag{98}$$

PTSC Solar share of the power plant can be calculated by the below equation [2].

$$f_{solar} = \frac{\dot{Q}_{u,solar}{}^{+}}{\dot{Q}_{comb}{}^{+} + \dot{Q}_{u,solar}{}^{+}} \tag{99}$$

The capacity factor (CF) of the power plant can be calculated by the below equation [1].

$$CF = \frac{\int_0^t \dot{W}_{\mathrm{net}}\, dt}{\dot{W}_{\mathrm{net}}\, t} \tag{100}$$

The capacity factor indicates the availability of the power plants to produce electricity during the day. It can be defined as the ratio between the actual working load of the power plant over the full working load of the power plant [3].

3.5 Model Optimization

Model optimization is an essential factor to determine the optimal characteristics and parameters of ABHGT and HGT. Moreover, it helps to estimate and compare the thermodynamic, economic and environmental performance of each model. Nevertheless, an optimal model can be determined by following certain optimization algorithm techniques. An optimization problem usually contains sets of design variables with aforementioned subjected constraints to optimize a certain given objective function. An optimization problem of power plants can have a distinctive objective function of minimizing the total capital cost, the levelized cost of electricity, CO_2 emissions. Moreover, typical sets of design variables can be number of PTSC units, aperture area of PTSC field, and minimum approach temperature on the heat exchanger. Optimization problems can be categorized based on the complexity of the system. A typical power plant system is classified as nonlinear and discontinuous model with real and mix of integer design variables. For instance, the number of PTSC units is classified as an integer design variable whereas compressor pressure ratio is real design variable. Therefore, optimization problems of power plants classified as a mixed integer nonlinear problem. Furthermore, the implemented algorithm that is used to fit these criteria's is multi-objective evolutionary algorithms. This algorithm is used since optimization process requires an analysis of multi objective functions [64,65].

3.5.1. Multi-objective evolutionary algorithm of ABHGT and HGT. The power plant models as disused are categorized as multi objective problems (MOP). The optimization algorithm that is used for ABHGT and HGT is multi-objective evolutionary algorithm [65].

3.5.1.1 Pareto optimal front algorithm. The multi objective algorithm method that is used in this project is the Pareto optimal front method shown in Figure 19.

This method has less draw backs over the other methods. The advantages of using this method as it gives clear sign of the tradeoff curve between the objective function in the objective space. For example, using Pareto optimal front method on ABHGT plant would illustrate clear indication of the tradeoff curve between total capital cost and cost of CO_2 emissions. Moreover, it gives multi-solutions which satisfy the convergence of the of the optimization problem. Pareto optimal front method defines a pareto optimal point when there are no better objective points on the objective space. Therefore, moving away from Pareto optimal point leads to worse ranking of the objective points [65,66].

Pareto Optimality of a vector at objective space can be defined as:

"A vector $u \in F \in R^m$ is said to be Pareto-optimal in F if $\nexists \boldsymbol{v} \in F$ such that:

$v_k \le u_k \;\; \forall k = 1, \ldots. m$ and $v_k < u_k$ for at least one k" [65,67].

Pareto Optimality of a Vector at search space can be defined as:

"Given a search space $S \in R^n$, an objective function space $F \in R^m$ and an objective function $f : S \rightarrow F = \{f(x : x \in S)\}$, a vector $x \in S$ is said to be Pareto-optimal in S and f if $\nexists$y$\in F$ such that $f_k(y) \le f_k(x) \;\; \forall k = 1, \ldots. m$ and $f_k(y) < f_k(x)$ for at least one k" [65,68].

Paetro dominance vector at the search space can be defined as:

"A vector $v = (v_1, \ldots, v_m)$ is said to dominate a vector u if *and only if*

$\forall k \in \{1, \ldots. m\} : v_k \le u_k \cap \exists\, k \in \{1, \ldots. m\}, v_k < u_k$ " [65,68].

It can be simplified as a given two individuals represented by x_1 and y_1 and their corresponding objective function values v_1 and u_1. It can be noticed that x_1 dominates y_1 if v_1 dominates u_1. By agreement, this is symbolized by $x < y$.

On the other hand, Paetro non-dominance vector can be defined as:

"An individual x* *is non-dominated in a population of I individuals if and only*

$If\ \forall i\ \in \{1, \dots .m\}: x^i \nprec x^*$ ''[65,69].

It can be simplified as for a given population of individuals; the non-dominance set (NDS) vector is the approximation of pareto optimal front (POF). It can be noticed from Figure 19 that the function (f) transforms the vector from search space (S) at the left to the objective space (F) at the right, ($S \rightarrow F$), where $S \in R^n$ and $F \in R^m$.The vector (x) in the search space transforms to the equivalent vector (u) in the objective function through multi objective function (f).Moreover, it can be said that the vector u is Pareto optimal vector if it lies on the POF line. Also, Paetro dominance vector at the search space can be illustrated as: x_2 is dominated by x_1 at the search space when the corresponding u_1 has lower value than u_2 on the objective space. Thus, the best individuals which are found in the search space will be lining on the non-dominance set (NDS) line [65, 70].

3.5.2. Queueing multi objective optimizer. Queueing multi objective optimizer (QMOO) is used as optimization method for this project. QMOO optimization uses the Pareto optimal front algorithm [65].

The fittest individuals of the population are selected by applying POF and NDS methods. The duration of the optimization problem depends on the number of iterations needed for convergence. More iterations at the optimization problem are needed for the NDS to achieve convergence towards the POF.

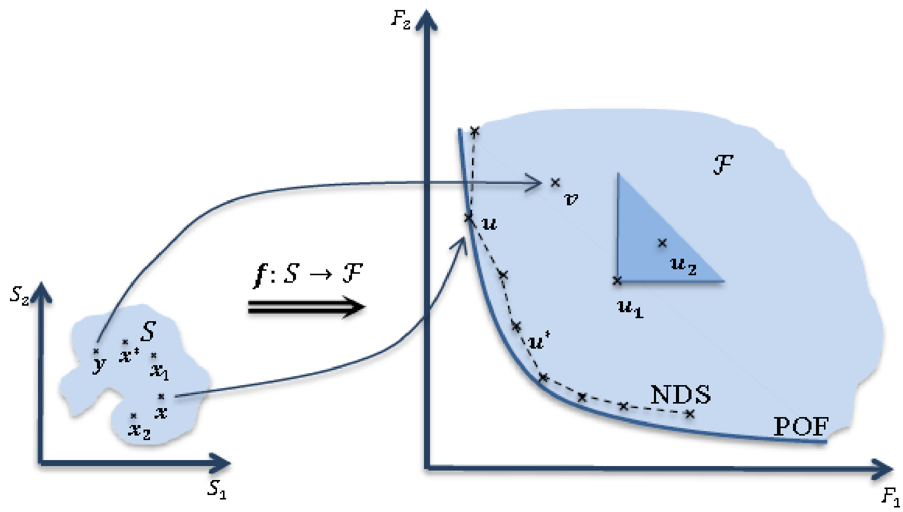

Figure 19: Pareto optimal front (POF) method: solution space (left) objective space (right) [65].

QMOO needs to be coupled with the model developed interface. Moreover, MATLAB optimization interface called OSMOSE is built to link the thermo-economic analysis of the model with QMOO in order to selects the suitable decision variable that satisfies the objective function problem. The optimization process of the model is illustrated by a flow chart shown in Figure 20.

The optimization setup process can be explained by simplified flow chart steps shown in Figure 20. The model interface collects the input data from the steady state results file (step 1), create an input file supported with weather data for the transient analysis which is done by TRNSYS (step 2), collects data from transient results file (step 3). Moreover, the model interface reads the transient analysis results and lunches an input file for the economic analysis (step 4) and collect the cost and model's performance indicators results analysis (step 5). The model interface sends all the results to MATLAB optimization interface called OSMOSE (step 6). The optimization problem is defined by an input file containing the objective functions, decision variables and optimization specifications. The optimization problem input file is sent to QMOO (step 7).

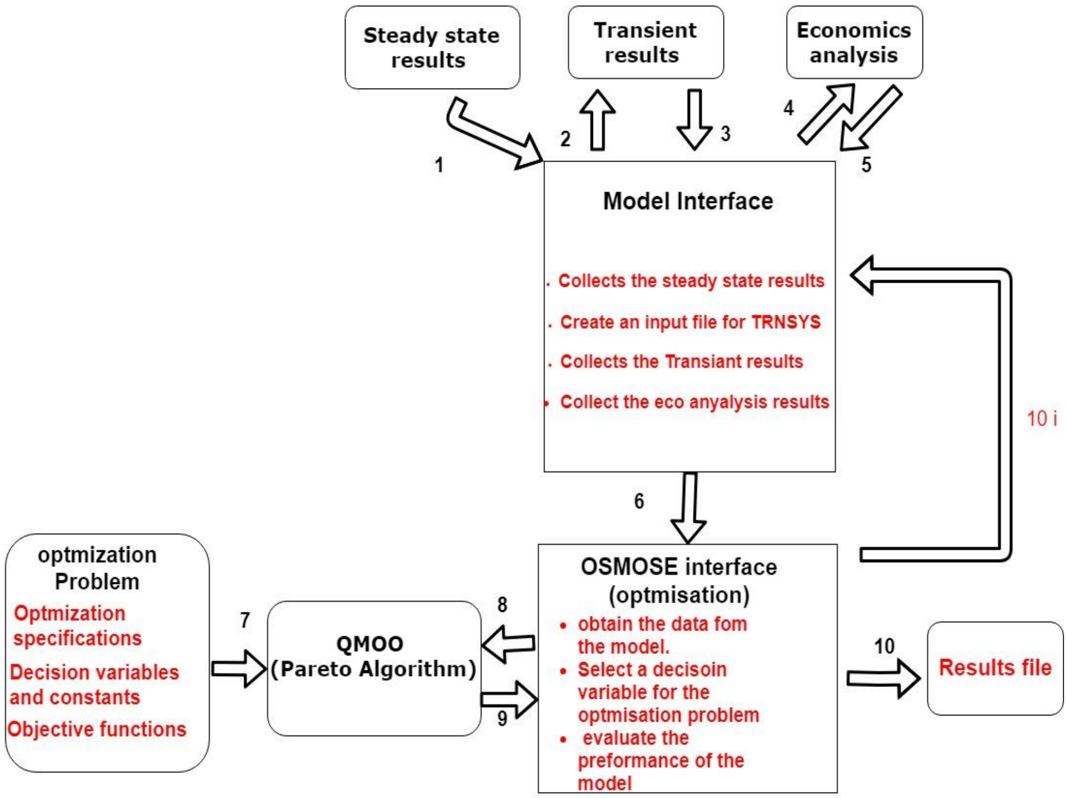

Figure 20: Flow chart of ABHGT and HGT optimization process.

OSMOSE interface sends the result file as input file to QMOO (step 8). QMOO selects an optimal decision variable according to the optimization problem by applying pareto optimal front (POF) algorithm method and send it back to OSMOSE interface (step 9). Finally, OSMOSE interface collects the results and send them as an external output result file (step 10). These procedures are repeated every computational iteration (step 10i) till the system achieve convergence or the simulation of the optimization model is stopped by applying a pre-restrained numbers of iterations.

3.5.3. Optimization setup. The optimization problem is evaluated based on an optimization setup of choosing an objective function, decision variables and constants

3.5.3.1 Objective functions. The selected objective functions in this thesis are conflicting to each other's as they give clear sign of the tradeoff. The objective functions are minimizing the total capital cost (Z_{TCC}) of the power plant and the specific amount of CO_2 per unit of electricity emitted by the plant $\left(f_{CO_2}\right)$. Accordingly, minimizing the specific of CO_2 amount requires more solar equipment to provide more solar share, which leads to an increase in the total capital cost.

3.5.3.2. Decision variables. The topping cycle parameters will be validated by Siemens SGT-800 and Siemens SGT-A45 so the data will be collected from the steady state analysis. However, the bottoming cycle paraments need to be optimized to obtain the optimal value. The heat exchanger minimum approach temperature needs to be optimized to acquire the optimal capital-energy trade off. The heat exchanger components in this model are heat waste, recuperator and intercooler. Table 10 illustrates the decision variables selected for the optimization problem with their corresponding validation ranges.

Table 10: Decision variables selected for the optimization problem.

Decision Variables	**Range**
Number of PTSCs (N_{PTSC}) (unit)	[100-1000]
Aperture area of PTSC A_{PTSC} (m^2)	[100-150]×10^3
Bottoming Compressor ratio	[1.5-3]
Heat waste Minimum approach Temperature (C°)	[5-40]
Recuperator Minimum approach Temperature (C°)	[5-40]
Intercooler Minimum approach Temperature (C°)	[5-40]

3.5.3.3. ABHGT and HGT operating mode. The ABHGT and HGT power plants are both flexible on operating mode since they are hybrid power plants. Therefore, running the system without thermal storage at night would increase the CO_2 emissions since the power plant will be running purely by fuel. Consequently, the LCOE will increase at night. In addition, the electricity demand of Abu Dhabi at night is lower than daytime. Hence, running the power plant during the day would be more efficient since the demand is high.

Furthermore, the price of electricity sale is higher when the demand on electricity is high. Therefore, running the power plant with partial load will improve the NPV of the investment. Accordingly, the ABHGT and HGT power plants will be working with partial load. The Gas turbine power plants will be working from 6:30 am till 9:30 pm and turned off from 9:30 pm to 6:30 am.

3.5.3.4. Economic parameters of the optimization. The economic parameters of the optimization problem is illustrated in Table 11. It can be noticed the fuel and water cost are fluctuating through the years. For simplicity, these values are assumed to be constants for the sake of the optimization problem. Moreover, the fluctuation in these permeates will be studied in the sensitivity analysis.

Table 11: Economic parameters of the optimization problem.

Economic parameter	Value
Annual insurance rate (r_{ins}) in %	1
Interest rate (r) in %	7
Water price in $\left(\frac{\text{US \$}}{m^3}\right)$	1
Natural gas price in $\left(\frac{\text{US \$}}{MWh}\right)$	10
Plant lifetime in (years)	25

Chapter 4: Results and Discussion

In this chapter, all the acquired results and discussions for the proposed configurations are presented and discussed. Initially, the steady state model is presented and validated with literature models. Then, dynamic models for transient operation are presented. Furthermore, optimization setup, results, and convergence are presented. Lastly, comparative thermo economic and environmental analyses are presented for the four proposed power plant configurations.

4.1 Steady State Analysis

4.1.1 parabolic trough solar collector. The parabolic trough solar collector heat transfer fluid (HTF) is air. Table 12 illustrates the parabolic trough solar collector nominal parameters and results. It can be noticed that 827 units of PTSCs is needed to achieve the required useful energy rate to be transferred to the turbine. These nominal values can be changed after the Thermo-economic optimization process to obtain the optimum values. All the thermal properties of air are selected from HTF literature shown in Table 13 [34]. Appendix A and B illustrate the steady analysis methodology.

Table 12: Parabolic trough solar collector nominal parameters and results

Parameters	Symbols	Values
Useful energy rate (MW)	$\dot{Q}_u$	65.12
Inlet Temperature (K)	T_{in}	723
Outlet Temperature (K)	T_{out}	1173
Total mass flow rate of air (kg/s)	$\dot{m}_{air,total}$	134
mass flow rate of air per PTSC (kg/s)	$\dot{m}_{air}$	0.1622
Number of PTSCs (N_{PTSC}) (unit)	N_{PTSC}	827
Aperture area A_{PTSC} (m^2)	A_{PTSC}	124050
Pipe receiver outside diameter (m)	D_{r_o}	0.05
Receiver inside diameter (m)	D_{r_i}	0.04
Glass cover outer diameter (m)	D_{c_o}	0.09
Collector width (m)	W	10
Collector length (m)	$Lpara$	15
Receiver thermal conductivity ($\frac{W}{m\,K}$)	kr	15
Receiver temperature (°C)	Tr	260
Receiver emissivity	ε_r	0.92
Receiver efficiency	η_r	0.75
Glass cover emissivity	ε_c	0.87
Stefan-Boltzmann constant ($\frac{W}{m^2\,K^4}$)	σ	5.67×10^{-8}
Sun temperature K	T_s	5770
Ambient temperature °C	T_{amb}	25
Glass cover temperature°C	T_{cc}	64
Atmospheric pressure Kpa	P_{atm}	101.325
Wind velocity (m/s)	v	5

Table 13: HTFs thermal properties for different working Temperatures [34].

T_{in} (°C)	Property	Pressurized Water	Therminol VP-1	Molten Salt	Liquid Sodium	Air	CO_2	He
300	k (W/mK)	0.628	0.135	-	-	0.036	0.031	0.160
	ρ (kg/m^3)	994	1046	-	-	0.769	1.098	0.146
	C_p (J/kgK)	4164	1577	-	-	1021	1004	5193
	μ (Pa s)	$5.9{\cdot}10^{-4}$	$3.2{\cdot}10^{-3}$	-	-	$2.5{\cdot}10^{-5}$	$2.3{\cdot}10^{-5}$	$2.1{\cdot}10^{-5}$
400	k (W/mK)	0.674	0.124	-	86.9	0.043	0.037	0.191
	ρ (kg/m^3)	926	964	-	918	0.632	0.939	0.112
	C_p (J/kgK)	4277	1860	-	1370	1040	1057	5193
	μ (Pa s)	$1.9{\cdot}10^{-4}$	$6.6{\cdot}10^{-4}$	-	$5.9{\cdot}10^{-4}$	$2.9{\cdot}10^{-5}$	$2.6{\cdot}10^{-5}$	$2.5{\cdot}10^{-5}$
500	k (W/mK)	0.622	0.109	-	79.8	0.049	0.044	0.221
	ρ (kg/m^3)	813	878	-	896	0.537	0.813	0.091
	C_p (J/kgK)	4741	2128	-	1332	1062	1104	5193
	μ (Pa s)	$1.1{\cdot}10^{-4}$	$3.2{\cdot}10^{-4}$	-	$4.1{\cdot}10^{-4}$	$3.2{\cdot}10^{-5}$	$3.0{\cdot}10^{-5}$	$2.9{\cdot}10^{-5}$
600	k (W/mK)	-	0.091	0.506	73.4	0.054	0.051	0.251
	ρ (kg/m^3)	-	775	1880	873	0.467	0.713	0.076
	C_p (J/kgK)	-	2392	1504	1300	1086	1145	5193
	μ (Pa s)	-	$2.0{\cdot}10^{-4}$	$2.7{\cdot}10^{-3}$	$3.2{\cdot}10^{-4}$	$3.5{\cdot}10^{-5}$	$3.3{\cdot}10^{-5}$	$3.3{\cdot}10^{-5}$
700	k (W/mK)	-	0.069	0.525	67.8	0.059	0.057	0.281
	ρ (kg/m^3)	-	641	1816	851	0.413	0.633	0.066
	C_p (J/kgK)	-	2768	1521	1276	1108	1180	5193
	μ (Pa s)	-	$1.3{\cdot}10^{-4}$	$1.6{\cdot}10^{-3}$	$2.6{\cdot}10^{-4}$	$3.8{\cdot}10^{-5}$	$3.6{\cdot}10^{-5}$	$3.7{\cdot}10^{-5}$
800	k (W/mK)	-	-	0.545	62.7	0.064	0.064	0.310
	ρ (kg/m^3)	-	-	1752	827	0.371	0.568	0.058
	C_p (J/kgK)	-	-	1539	1260	1129	1211	5193
	μ (Pa s)	-	-	$1.2{\cdot}10^{-3}$	$2.3{\cdot}10^{-4}$	$4.0{\cdot}10^{-5}$	$3.9{\cdot}10^{-5}$	$4.0{\cdot}10^{-5}$
900	k (W/mK)	-	-	-	58.1	0.069	0.070	0.338
	ρ (kg/m^3)	-	-	-	804	0.336	0.515	0.052
	C_p (J/kgK)	-	-	-	1252	1148	1238	5193
	μ (Pa s)	-	-	-	$2.0{\cdot}10^{-4}$	$4.3{\cdot}10^{-5}$	$4.2{\cdot}10^{-5}$	$4.4{\cdot}10^{-5}$
1000	k (W/mK)	-	-	-	54.1	0.073	0.076	0.366
	ρ (kg/m^3)	-	-	-	780	0.307	0.471	0.047
	C_p (J/kgK)	-	-	-	1252	1164	1262	5193
	μ (Pa s)	-	-	-	$1.8{\cdot}10^{-4}$	$4.5{\cdot}10^{-5}$	$4.5{\cdot}10^{-5}$	$4.7{\cdot}10^{-5}$

4.1.2. Gas Turbine plants (HGT and ABHGT). A thermodynamic status at each point on the cycle is simulated through (EES) which can be illustrated at Table 14 while Figure 21 illustrates the temperature entropy diagram for both cycles. The ambient air is compressed adiabatically through compressor (1-2). After compression, air enters the parabolic trough where it is preheated with the available solar flux at the receiver (2-3). Next, air goes through the combustion chamber and heat is added to the air fuel mixture in an isobaric process (3-4) where the firing temperature reaches 1673 K. In the next stage, the mixture of gases departing the combustion chamber are mixed with cooled air and expanded adiabatically in the gas turbine with TIT of 1515 K for power generation.

Exhaust gases from the topping gas turbine go through the air heat exchanger where a portion of the available waste heat is recovered by the bottoming cycle air flow (5-6). In the bottoming cycle, ambient air is drawn into the bottoming cycle compressor (7) and it is compressed adiabatically (7-8). It is then intercooled through an intercooler and entered into the high-pressure compressor (9-10). Afterwards, it is heated up successively by the heat exchanger with exhaust air from the topping and bottoming turbines that passed through waste heat recovery and recuperator, respectively (10-11). It is finally expanded in the turbine and cooled down in the recuperator (11-12).

Table 14: Cycle thermodynamic properties analysis of ABHGT through EES

Stage No	P_i [KPa]	S_i [KJ/Kg.K]	T_i [K]	h_i [KJ/Kg]
1	101.3	6.83	298	300.4
2	2137	6.9	723	738.1
3	2135	7.5	1173	1246
4	2120	7.9	1515	1846
5	2035.6	7.9	848	875
6	105.5	7.4	573	578.8
7	101.3	7.35	300	300.4
8	253.8	7.37	373	374
9	246.8	7.15	323	323.6
10	617	7.17	423	424.6
11	580	7.84	798	819.8
12	105.4	7.95	523	526.9

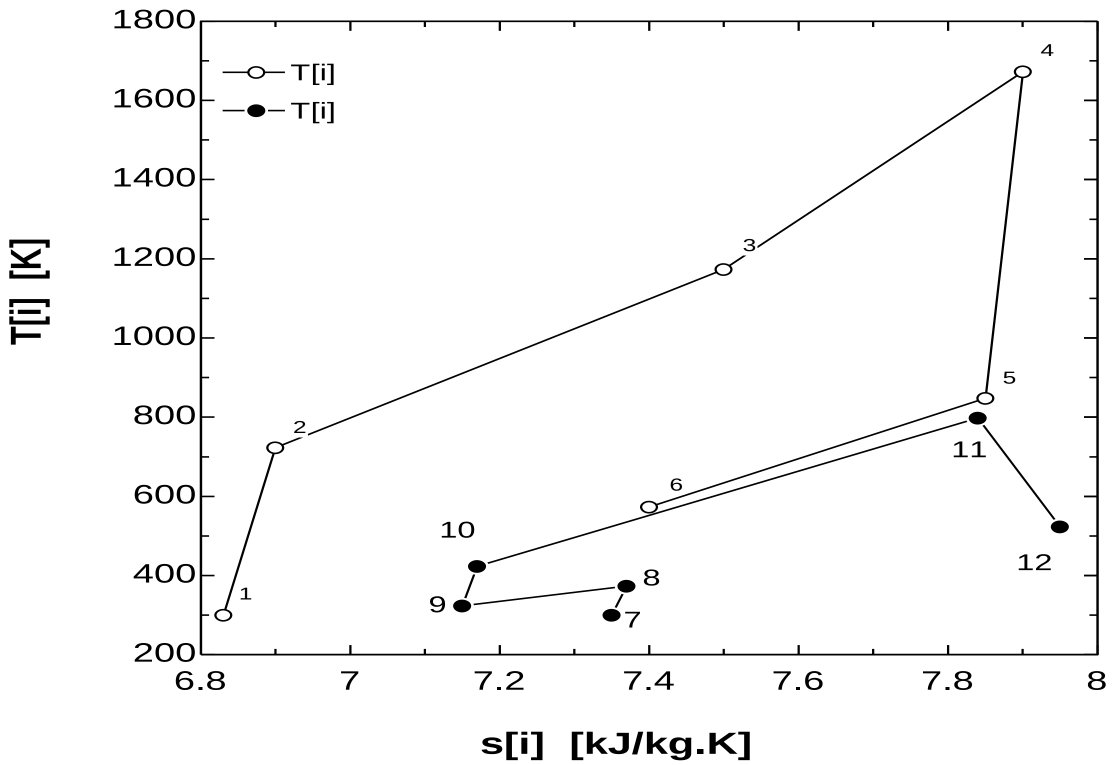

Figure 21: T_S diagram of ABHGT model

To be able to apply thermo-economic and environmental analysis on HGT and ABHGT, nominal parameter selection and steady state results need to be illustrated at the beginning. These steady state analyses are done through MATLAB and EES. It can be noticed that the main difference between HST and ABHGT plants is adding a bottoming cycle. So, HGT represents the same plant of ABHGT but without its bottoming cycle. Table 15 represents the nominal parameter selection of the power plant.

Table 15: Gas Turbine nominal parameters and constrains:

Parameter	**Assigned values**
Natural gas lower heating value (kJ/kg)	50000
LPG lower heating value (KJ/kg)	46607
Top turbine exhaust air Mass flow rate (kg/s)	134.2
Fuel ch4 mass flow rate(kg/s)	1.5
Gas mixture flow rate (kg/s)	135.5
Bottom cycle Air Mass flow rate (m/s)	138
Reference temperature (K)	298
Combustion chamber efficiency	98%
Combustion chamber pressure drop	4%
Top Compressor pressure ratio	21.1:1
Bottoming LP compressor pressure ratio	2.5:1
Bottoming HP compressor pressure ratio	2.5:1
Compressor isentropic efficiency	85%
Compressor mechanical efficiency	99%
Turbine isentropic efficiency	85%
Turbine mechanical efficiency	99%
Generator electrical efficiency	99%
Generator mechanical efficiency	98%
Minimum approach temperature of Heat exchanger (℃)	30

The main nominal results and specification comparison of HGT and ABHGT are summarized and illustrated at Table 16. The simulation analyses are done through

MATLAB for both top and bottoming cycle. It can be noticed the characteristics and specification of HGT is the same as ABHGT but without its bottoming cycle.

Table 16: Gas Turbine models' nominal specifications and results (for HGT and ABHGT).

Parameters	HGT	ABHGT
Top Compressor pressure ratio	21.1:1	21.1:1
Top Turbine pressure ratio	19.2:1	19.2:1
Top Turbine Exhaust gas temperature (K)	848	848
Top Turbine Exhaust gas mass flow rate (kg/s)	134.2	134.2
Fuel mass flow rate (kg/s)	1.5	1.5
Top cycle Power output (MW)	47	47
Bottom LP and HP Compressor pressure ratio	-	2.5:1 (for both)
Bottom Turbine pressure ratio	-	5.5:1
Bottom turbine Exhaust gas mass flow rate (kg/s)	-	137.5
Bottom cycle Power output (MW)	-	9
Total Power output (MW)	47	56
Total plant Energy Efficiency (%)	33.6	40
Total plant Exergy Efficiency (%)	37.6	44.8
Solar share (f_{solar}) (%)	46	46
Specific emission of CO_2 (kg/MWh)	307	257.6

Solar share of the plant can be calculated by the below equation:

$$f_{solar} = \frac{\dot{Q}_{u,solar}{}^{+}}{\dot{Q}_{comb}{}^{+} + \dot{Q}_{u,solar}{}^{+}} \quad (101)$$

where $\dot{Q}_{u,solar}{}^{+}$ is the useful solar energy rate from the PTSC in KW and $\dot{Q}_{comb}{}^{+}$ is the heat rate supplied to the combustion chamber in (KW).The specific of CO_2 amount per unit of electricity emitted by the plant can be calculated by the below equation:

$$f_{CO_2} = \frac{44}{12}\left(\frac{c_c{}^{fuel}\dot{m}_f}{\dot{W}_{net}}\right) \quad (102)$$

where $c_c{}^{fuel}$ is the fuel carbon content, $\dot{m}_f$ is the fuel mass flow rate in (kg/s) and $\dot{W}_{net}$ is total power output of the plant in (MW).

It can be noticed from the nominal results presented on Table 16 that total Power output, energy and exergy efficiencies are improved by (19%) with the addition of the bottoming cycle. Moreover, it can be shown that ABHGT has less specific emission of CO_2 by 16(%) than HGT. Furthermore, it can be noticed that the exergy efficiency for both plants is higher than the energy efficiency because the available heat in the PTSC receiver has less exergy content than energy content due to a lot of losses at the receiver. These improvements give economic incentive to build additional bottom cycle.

4.1.2.1. Model validation. In order to know the accuracy of the simulated model of the power plant, the top cycle simulation results are compared with siemens gas turbine plant. Table 17 illustrates specification and results of HGT model without solar power compared with Siemens SGT-800 and SGT-A45(See Appendix C) [70]. These analyses are done under ISO conditions with ambient temperature of 15 (℃). HGT without solar power is analyzed by utilizing data of SGT-800 and SGT-A45 with the simulated MATLAB model. The results of the simulated model show a relative accurate analysis while comparing it with SGT-800 and SGT-A45. It can be noted that the power output is highly accurate with a relative error of (1%) for the simulated model once compared with literature. Furthermore, the energy efficiency of the model has an acceptable relative inaccuracy of (2.6 %) and (2.02%) when compared with Siemens SGT-800 and SGT-A45, respectively.

The main reason behind these small relative errors can be demonstrated by applying the Nasa polynomial method to compute the specific entropy and heat capacity of air and turbine exhaust gases. Moreover, natural gas lower heating value is calculated based on CH_4 and assumed to be the only source of energy in the combustion chamber while the natural gas contains multiple component with the CH_4.To improve the accuracy of the simulated model, real gases properties of air and more complex composition of fuel can be taken into consideration. Nevertheless, the complexity of the simulated model after applying these solutions does not justify the improvement in the simulated model accuracy. By comparing Tables 16 and 17, it can be noticed that the HGT without solar preheating has a quite better performance in terms of efficiency and power output than the actual HGT. This phenomenon can be explained by a lot of reasons. Firstly, using Parabolic trough solar collector leads to additional pressure losses which reduces the pressure ratio of the turbine. Secondly, the gas mixture that enter the turbine on HGT has lower energy content because of lower fuel mass flow rate content. Thus, steady state analysis is validated by Siemens SGT-800 and SGT-A45. The simulated model illustrates the nominal results and specifications that will be used in the transient analysis model.

Table 17: Comparison between Siemens SGT-800 and SGT-A45 catalogue and the simulated models [70]

Parameters	**Siemens GT-800 [70]**	**Simulated Model**	**Error (%)**	**Siemens SGT-A45 [70]**	**Simulated Model**	**Error (%)**
Compressor pressure ratio	21.1:1	21.1:1	-	27.9:1	27.9:1	-
Fuel mass flow rate (kg/s)	2.67	2.68	+0.375	2.25	2.26	0.444
Turbine Exhaust gas temperature (℃)	553	553	-	483	483	-
Exhaust gas mass flow rate (kg/s)	134.2	134.2	-	126	126	-
Power output (MW)	50.5	50	-1.0	44	43.6	-0.91
Efficiency %	38.3	37.3	-2.6	40.4	39.6	-2.02

4.2. Transient Analysis

Transient analysis is done to consider for the change in solar radiation reaching the parabolic trough solar collector and account for the heat variation that is supplied to the gas turbine plant. To be able to simulate and account for the off-design condition that changes with time, a dynamic model is needed. This Transient simulation is working with certain meteorological year of a typical place. The Transient analyses are done through TRNSYS and MATLAB to account for parameters that changes with time.

4.2.1. Dynamic model of gas turbine plant. TRNSYS is a dynamic simulation program which tabulate the results in flexible graphical environmental base. TRNSYS is divided to two main parts.

Firstly, an engine called Kernel which reads and simulate the parameters and input files. The engine starts its analysis by doing some iterations to solve certain problem tell convergence and illustrate the results on an output file with their system variables in graphical form. Kernel can assist on linear regressions, thermophysical properties, matrices, import external files and implement interpolations. Secondly, is an extensive library full of components, each of which simulate and model the behavior of one part of the system such as weather data file processor, compressor, turbine, heat exchanger, etc. Models are defined in such a way that help the user to modify a certain component or write their own ones. Moreover, it consists of an additional STEC library that provide solar and thermal components such as PTSC. Each component at the library can be expressed as a black box that involves the governing equation of a certain behavior. The inputs and output can be classified as time dependent variable parameters or time independent constant parameters. The components are connected to each other through links acting as wires or pipes. Inputs can be defined by an external file or an output of a certain type linked to it. Furthermore, TRNSYS can open and link weather files, read an input file of the steady state model from MATLAB. Outputs can be illustrated as a physical quantity or first derivative of it quantitates since the governing equations of inputs are either algebraic or first order differential equation. TRNSYS solve the problems numerically through three different methods which are non-self-starting Hein method, 4th-order Adams method and modified-Euler method.

4.2.1.1. TRNSYS dynamic model of gas turbine plant. The flow sheet of ABHGT is done by TRNSYS which represent the dynamic model of the plant. Figure 22 illustrates the model of solar and other components which are chosen from STEC Brayton sub library.

The model of Parabolic trough solar collector receiver is modelled by Type 423.Whereas, heat exchanger, turbines, compressors, gage pressure drop, and combustors of combustion chamber are simulated by Types 425, 426, 424, 429 and 427, respectively. When the PTSC receiver inlet temperature is higher than the outlet temperature of the PTSC receiver, bypass controller is used to set the outlet parameters of the parabolic trough receiver equally to the inlet parameters which means that the colder air will not enter the PTSC receiver and the Plant will be working purely with fuel gasses. This scenario happens on cloudy days or at night. To account for the off-design efficiency operating condition, the compressor model is simulated to address this issue by adjusting its isentropic efficiency, air mass flow rate, relative pressure drop according to the nominal inlet environmental conditions. Moreover, The Combustor in the combustion chamber also account for off -design operation conditions, where the fuel mass flow rate may vary to compensate for the heat lost or the pressure losses by the PTSC receiver. The topping Turbine assumed to be working with full load at any time so no need to account for off-design efficiency operating condition. Nevertheless, a control strategy is needed for the topping turbine to ensure that the top cycle power output is stable and not fluctuating. Furthermore, the bottoming turbine need to take in account off-design efficiency operating conditions since the bottoming turbine will be having inconsistent load. In reality, the bottoming turbine power output will always be lower than the nominal power in the steady state condition since the actual inlet temperature of the bottoming turbine is lower than the nominal inlet temperature. Thus, controlling the mass flow rate at bottoming turbine is not essential. The intercooler mass flow rate is set to be equal to the bottoming mass flow rate cycle. All the steady state parameters including the heat exchanger UA values, mechanical and isentropic efficiencies are imported externally as input file to TRNSYS.

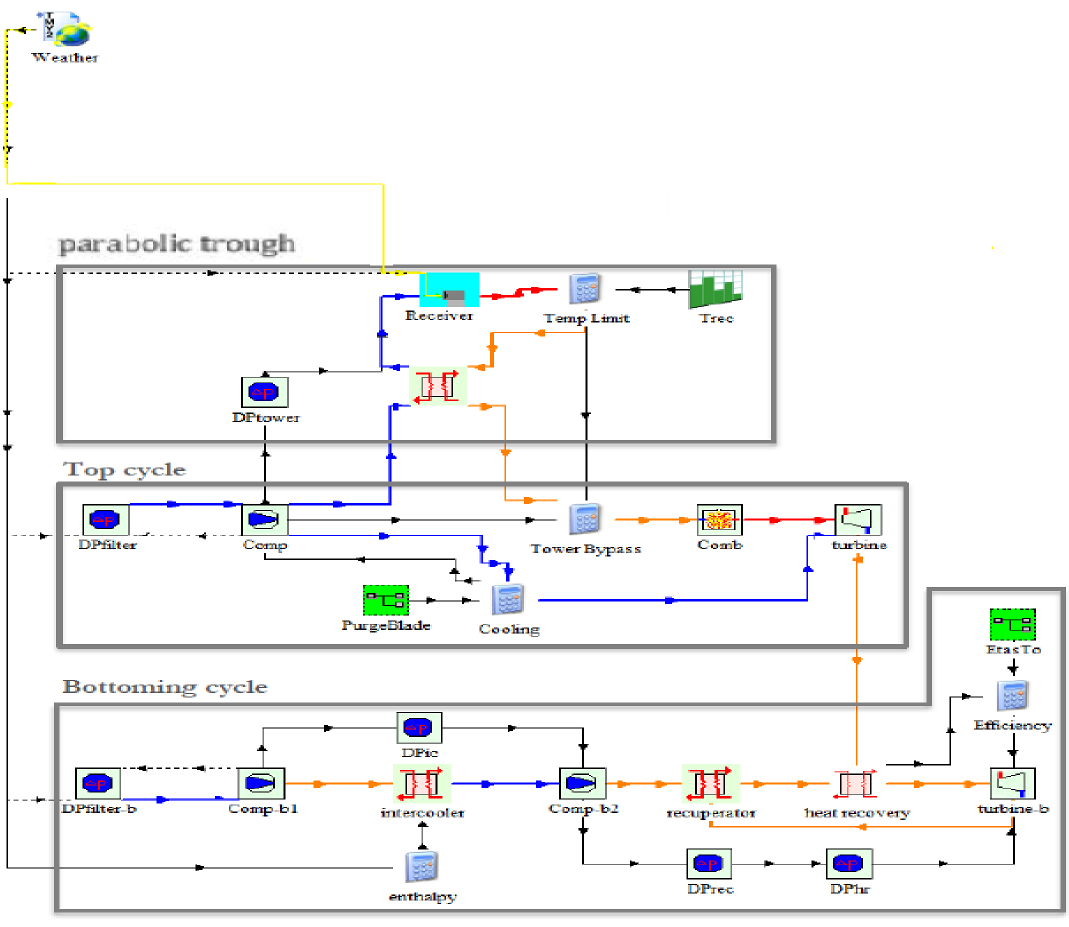

Figure 22: ABHGT dynamic model diagram

4.2.1.2.- Top turbine control and bottom turbine off-design efficiency. The topping turbine assumed to be working with full load at any time so no need to account for off-design efficiency operating condition.

Nevertheless, a control strategy is needed for the topping turbine to ensure that the top cycle power output is stable and not fluctuating, since there is a change in the ambient condition that cause unstable power output. The turbine controller is used to control inlet vane angle of the turbine to maintain stable nominal power output by estimating the required volumetric flow rate. The purge controller which is used to control the change on vanes angle of the topping turbine has two limits.

The upper limit occurs once the maximum mass flow rate passes through as the vanes angle of topping turbine is fully opened. This scenario happens when the nominal parameter conditions including the mass flow rate are equally to the realistic operating condition. The maximum mass flow rate in (kg/s) can be defined by the below equation under the ISO conditions (20℃, 101.3 KPa).

$$\dot{\mathrm{M}}_{\mathrm{max}} = \dot{\mathrm{M}}_{\mathrm{ISO}} \left(\frac{T_{ISO}}{T_a}\right)\left(\frac{P_a}{P_{ISO}}\right) \tag{103}$$

Where P_{ISO}, T_{ISO}, $\dot{\mathrm{M}}_{\mathrm{ISO}}$ are pressure in (KPa), temperature in (℃), mass flow rate in (Kg/s) at ISO condition, and T_a, P_a are the ambient temperature in (℃), and the ambient pressure in KPa. Therefore, an increase in ambient temperature will lead to a decrease in maximum mass flow rate and result on a small decrease on the power output. The small decrease on the power output which was induced by the control strategy will result on having stable constant power output.

The lower limit occurs when the vanes angle of the topping turbine is bounded with certain constrains depending on the ambient temperature. The lower limit control will avoid any overloading scenarios above the compressor capacity. Thus, the actual minimum mass flow rate can be estimated as half of its nominal value. Nevertheless, the minimum mass flow rate is rarely reached since the Gas Turbine plants are built in suitable regional places. The minimum mass flow rate in (kg/s) can be defined by the below equation under the ISO conditions (20℃, 101.3 KPa) [2].

$$\dot{\mathrm{M}}_{\mathrm{min}} = \frac{1}{2}\left(\dot{\mathrm{M}}_{\mathrm{ISO}} \left(\frac{\mathrm{T_{ISO}}}{\mathrm{T_a}}\right)\left(\frac{\mathrm{P_a}}{\mathrm{P_{ISO}}}\right)\right) \tag{104}$$

Based on the previous the discussion, the bottoming cycle need to consider for the off-design efficiency since it has inconsistent load. The off-design efficiency equation below can be expressed by the change of bottoming turbine isentropic efficiency with the inlet temperature [2].

$$\eta_s = \eta_{s0} - 2\left(\sqrt{\frac{T_{in}}{T_{in0}}} - 1\right)^2 \tag{105}$$

Where T_{in0} and η_{s0} are the nominal temperature inlet in °C and isentropic efficiency.

4.2.2. Meteorological data. The dynamic model will be simulated on United Arab Emirates, specifically on Abu Dhabi. Abu Dhabi is chosen for the plant implementation due to its outstanding suitability for the collection of solar thermal energy.

Based on the discussed Table 1, which illustrates the mean dry bulb temperature of Abu Dhabi during the day for every month. It is very clear that the average temperature reaches its peak during noon with August having recorded the highest average temperature. Air temperature has a notable effect on the gas cycle thermal performance. Relative humidity is another crucial factor that highly influences the cycle performance. Nevertheless, it can be asserted that humid climates highly reduce the performance of humid air turbine cycles. The most vital component that must be considered for CSP analysis and solar thermal power generation is the rate of DNI obtainable within the appointed site's location. The average rate of DNI per hour available for Abu Dhabi was illustrated in T

able 2. From these results, it can be noted that the Rate of DNI supplied reaches its peak at noon. The amount of solar radiation per day on Abu Dhabi is considerably high which is about 18.5 MJ/m^2. The metrological data is imported through TRNSYS by an external input file called weather file. The dynamic simulation begins at 00:00 on January 1st and runs throughout the year.

4.2.3. Transient simulation results. The transient simulation is done on ABHGT since HGT is basically the same dynamic model without it is bottoming cycle.

It can be observed from Figure 23 that toping gas turbine cycle (red curve) has stable net power output during the cold season since a controller strategy is used. Purge controller is used to control the angle of inlet vain of the topping compressor to maintain constant power equal to the nominal power output. During the hot season, an increase in ambient temperature will lead to a decrease in mass flow rate. Therefore, producing the same nominal power output requires less mass flow rate and the angle of inlet vain of the topping compressor are not fully open. On the other hand, it can be noticed that the bottoming gas turbine cycle (blue curve) does not have constant net power output. The variation on the net power output is duo to the mass flow rate at the bottoming cycle is not controlled. During the cold season, the ambient conditions and mass low rate are quite similar to the nominal conditions. During the hot season, an increase in ambient temperature will lead to a decrease in mass flow rate and net power output.

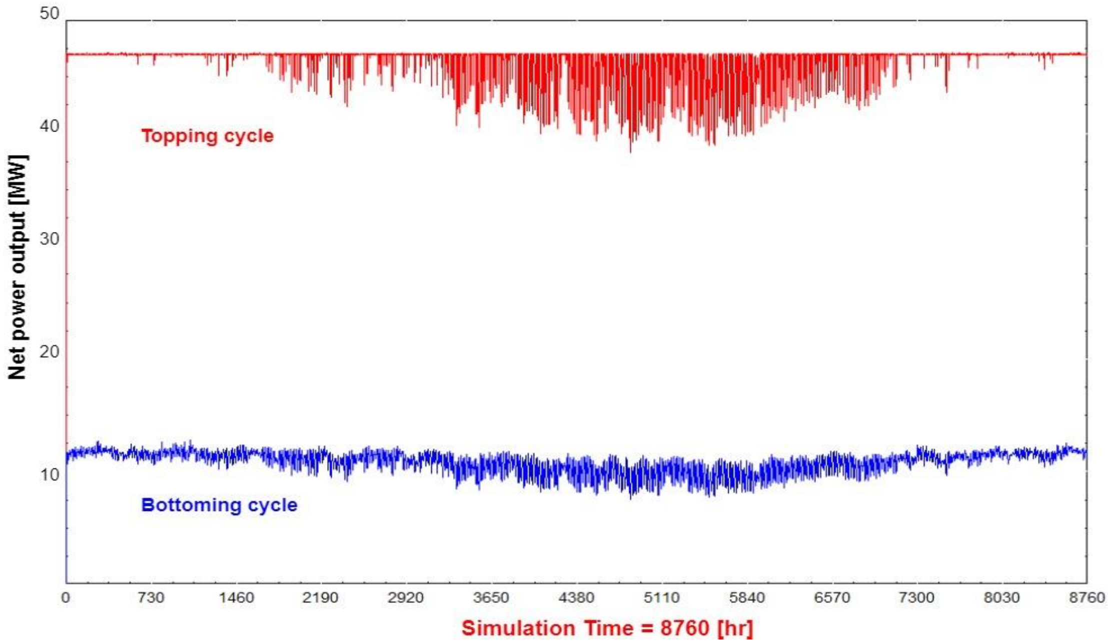

Figure 23: Net power output variation on ABHGT

Hourly simulation will be illustrated since seasonal simulation does not give detailed information analysis about the transient behavior of the dynamic model. The advantage of hourly simulation analysis is that a transient model can be illustrated with small time frame. So 30th of April is the day that is chosen to do the transient analysis on. This date was picked for two main reasons. Firstly, the transient control affect can be clearly seen throughout the day where the maximum mass flow rate of the topping turbine achieved. Secondly, the maximum temperature of PTSC receiver is reached.

Hourly simulation of combustor inlet temperature and PTSC outlet temperature are shown in Figure 24. The controller effect is clearly illustrated at the combustion chamber combustor. During the night, it can be noticed that the compressor outlet temperature is equal to the combustor inlet temperature since no solar share is provided through the PTSC. During the morning (at 7:30 am), the PTSC start heating the air leading to an increase on the combustor inlet temperature to reach its peak value of 900°C during noon (between 10:30 am till 6:30 pm) and drops down at night again.

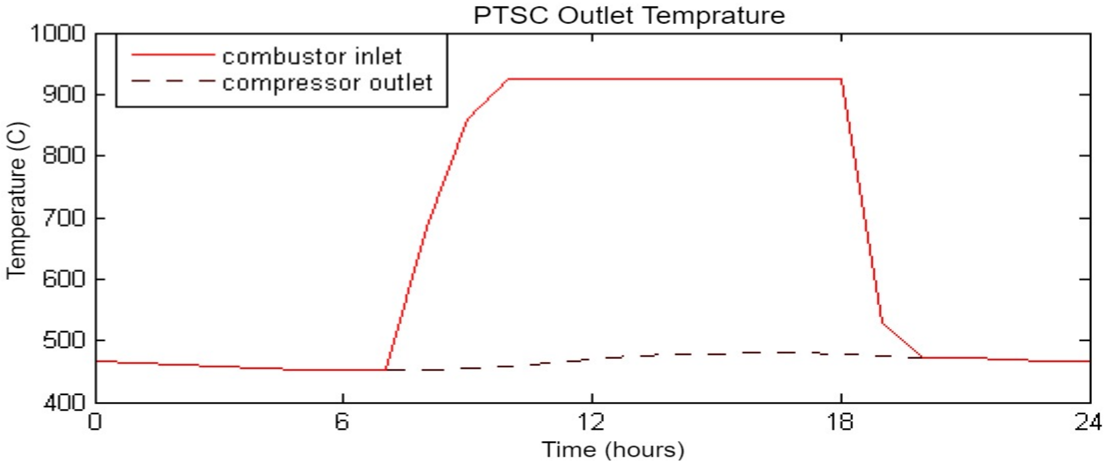

Figure 24: Hourly simulation of combustor inlet temperature and PTSC outlet temperature.

The hourly simulation of fuel and exhaust gases mass flow rates of ABHGT is shown in Figure 25. It can be noticed that the mass flow rate of fuel is decreasing by 7:00 am since the PTSC receiver preheats the air of the combustor inlet leading to less fuel is used to produce the same nominal power output. During the day, an increase in ambient temperature of the bottoming cycle (between 7:00 am till 5 pm) will lead to a decrease in exhaust mass flow rate of the turbine since its working at constant volumetric flow rate. On the other hand, an increase in ambient temperature of the topping cycle, (between 6:30 am till 10:30 am), will cause an increase in exhaust mass flow rate of the turbine since the solar share of PTSC increases. An increase on solar share will lead to less fuel burned, (topping turbine exhaust gasses have lower c_p), and cause less power output. Consequently, to produce the same nominal power output an increase on mass flow rate is needed. However, the control strategy induces an upper limit for the maximum mass flow rate. So, an increase in ambient temperature will lead to a decrease in maximum mass flow rate that will result on small decrease on the power output. The control strategy effect on the topping cycle, where the maximum mass flow rate cannot reach the nominal value, is clearly visible between 10:30 am till 6:30 pm.

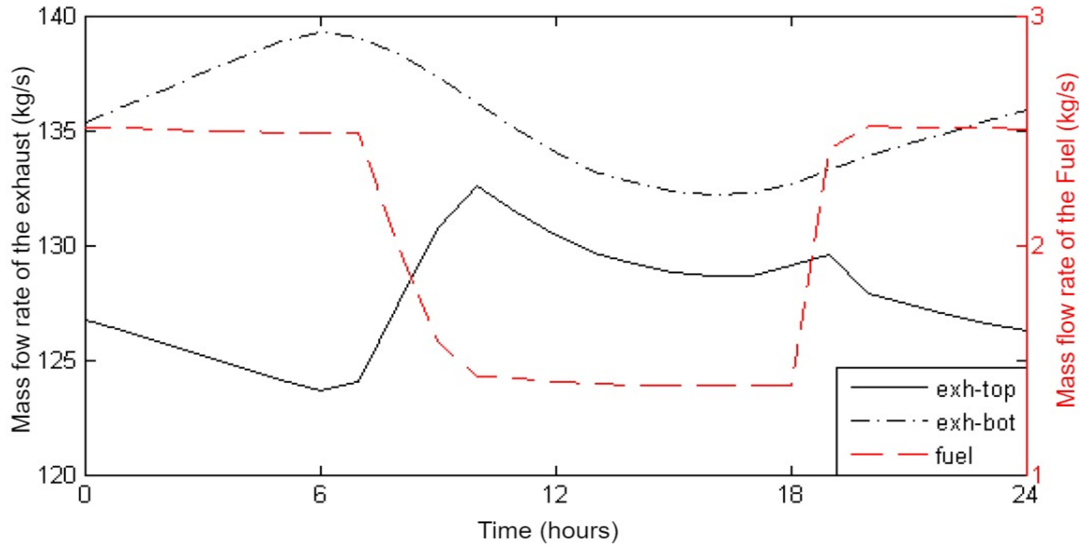

Figure 25: Hourly simulation of fuel and exhaust gases mass flow rates of ABHGT.

Hourly simulation of solar and fuel heat rates ABHGT are shown in Figure 26. It can be noticed that the fuel mass flow rate is directly promotional to the fuel heat rate. The fuel heat rate is decreasing by 7:00 am since the PTSC receiver preheats the air of the combustor inlet leading to less fuel is used to produce the same nominal power output.

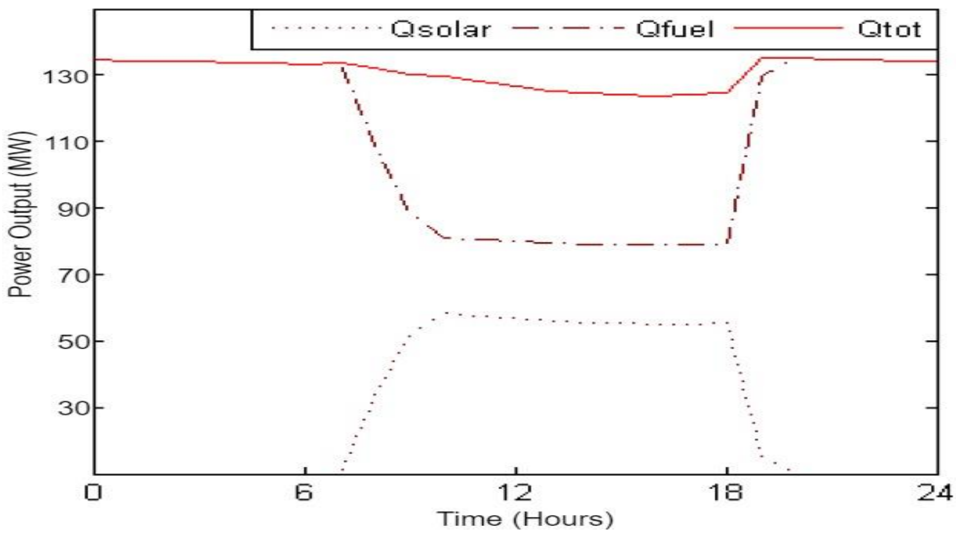

Figure 26: Hourly simulation of solar and fuel heat rates

The solar heat rate is produced by the PTSC receiver between 7:00 am till 6:30 pm. The total heat rate is almost constant since the decrease on fuel rate is compensated by an increase on the solar heat rate. Moreover, hourly simulation of ABHGT net power output is shown in Figure 27. The small drop in net power output at the top cycle, between 10:30 am till 6:30 pm, duo to control strategy that is used on top cycle. So, an increase in ambient temperature will lead to a decrease in maximum mass flow rate that will result on a small decrease on the net power output.

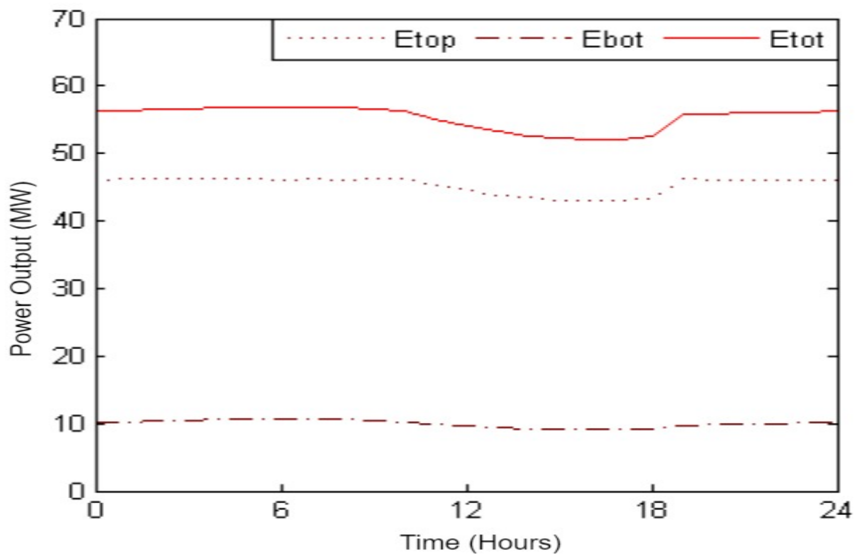

Figure 27: Hourly simulation of ABHGT net power output.

Hourly simulation of ABHGT overall energy and exergy efficiencies is shown in Figure 28. It can be observed that both energy and exergy efficiencies are high at night since the main source of power is fuel. The cycle efficiencies at night are equal to the overall efficiencies due to the absence of PTSC solar losses. During the morning (at 7:30 am), the PTSC start heating the air which lead to a drop in the overall efficiencies. The significant drop on both energy and exergy effectiveness, between 7:30am till 6:30 pm, is duo to solar losses. Moreover, it can be noticed that an increase on energy or exergy content lead to a decrease on energy and exergy efficiencies. Furthermore, it can be observed that energy efficiency is higher than the exergy efficiency at nigh but it’s the opposite during the day. Its higher at night as for producing the same power output, the energy content of fuel is lower than its exergy content. Nevertheless, its lower during the day since the energy content of direct normal radiation at PTSC is higher than its exergy content.

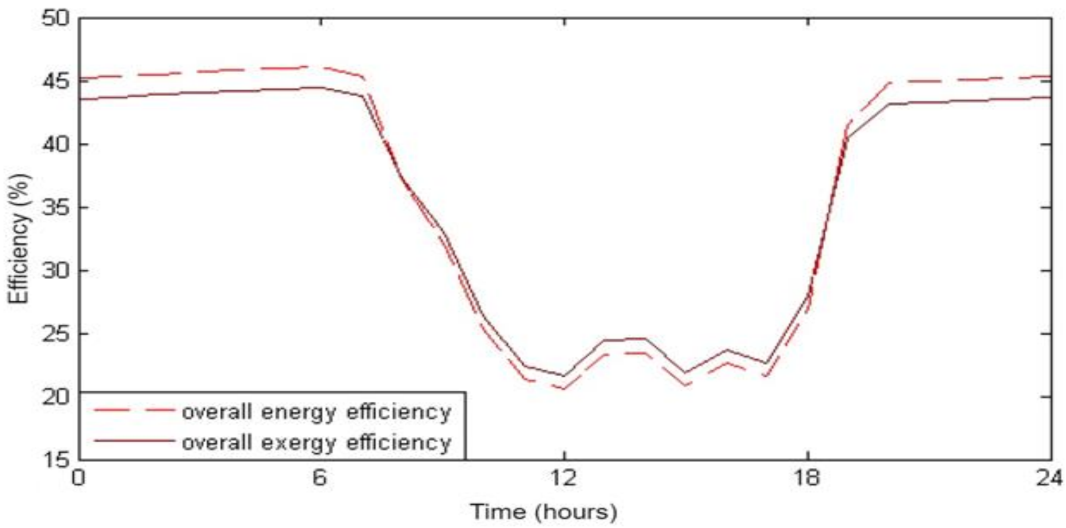

Figure 28: Hourly simulation of ABHGT overall energy and exergy efficiencies.

Hourly simulation of PTSC solar share is shown in Figure 29. It can be observed that there is no solar share during the night. It gradually increases from 7:00 am till 10:00 am and maintain at a constant peak level with 46% solar share until 6:30 pm. It rapidly drops to zero by 7 pm. As the solar share reaches to its peak by 46% during the day, which indicates that the fuel still delivers 54% of the total heat rate. Thus, the maximum solar share is limited by the PTSC receiver peak temperature.

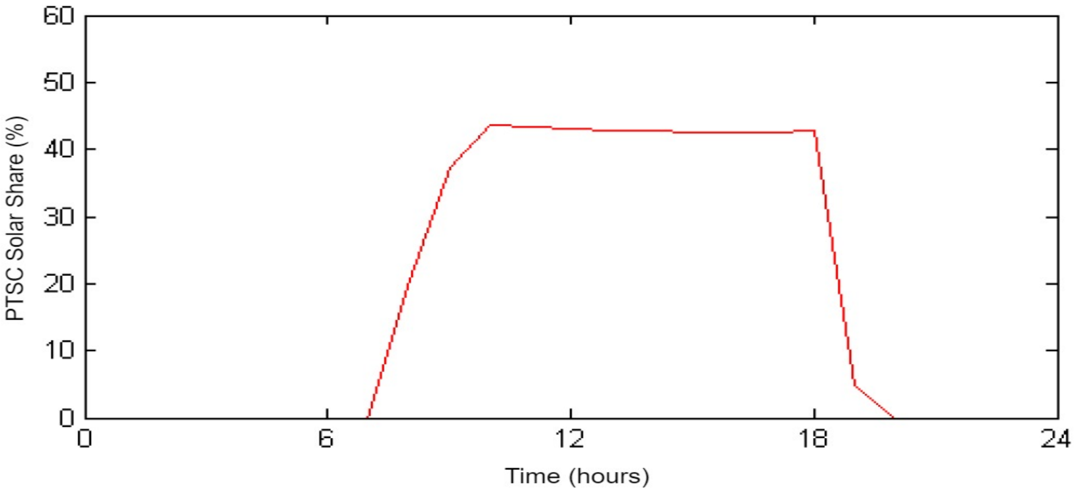

Figure 29: Hourly simulation of PTSC solar share.

4.3. Optimization Results

This section will illustrate the optimization results of the two models (HGT and ABHGT). The optimization algorithm was discussed on chapter 3. An optimization convergence is needed to allocate the optimal design variables and parameters of the optimization problem. This section will illustrate the power plant performance indicators results and assign a unified indicator to obtain an optimum confirmation that satisfies the optimization problem.

4.3.1. Optimization convergence. The optimization convergence algorithm results are illustrated on Figures 30 and 31. The multi objective algorithm method that is used in this project, is the Pareto optimal front method.

The advantages of using this method as it gives clear sign of the tradeoff curve between the objective functions in the objective space. Using Pareto optimal front method on HGT and ABHGT power plants would illustrate a clear indication of the tradeoff curve between the total capital cost and the cost of CO_2 emissions.

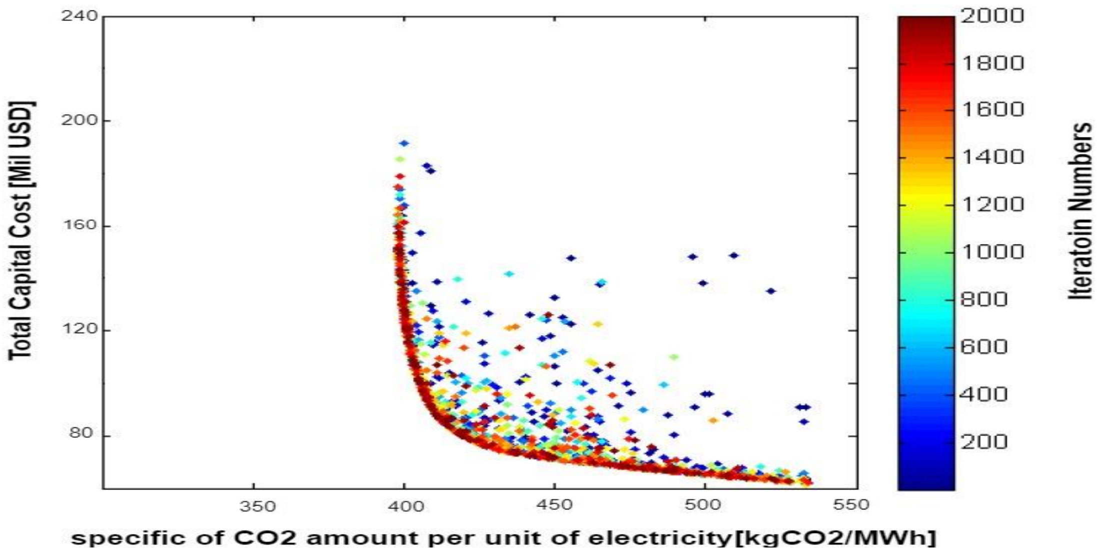

Figure 30: The optimization convergence algorithm of HGT

Pareto optimal front (POF) method defines a pareto optimal point when there are no other better objective points on the objective space. Accordingly, moving away from Pareto optimal curve leads to worse ranking of the objective points. Therefore, the first iteration on the optimization problem represents the first individual that lies on the Pareto optimal curve. As the number of iterations increase, more individuals shape the Paetro optimal curve. Thus, the individuals laying on the pareto optimal curve illustrates the optimal design parameters where the total capital cost can’t be minimized further to achieve lower CO_2 emissions. As Decreasing the CO_2 emissions below the pareto optimal curve will lead to an exponential increase on the total capital cost. It can be noticed that the number of iterations needed for convergence is less on HGT than ABHGT power plants. This is due to a simpler optimization problem where HGT power plant requires smaller number of iterations to reach convergence.

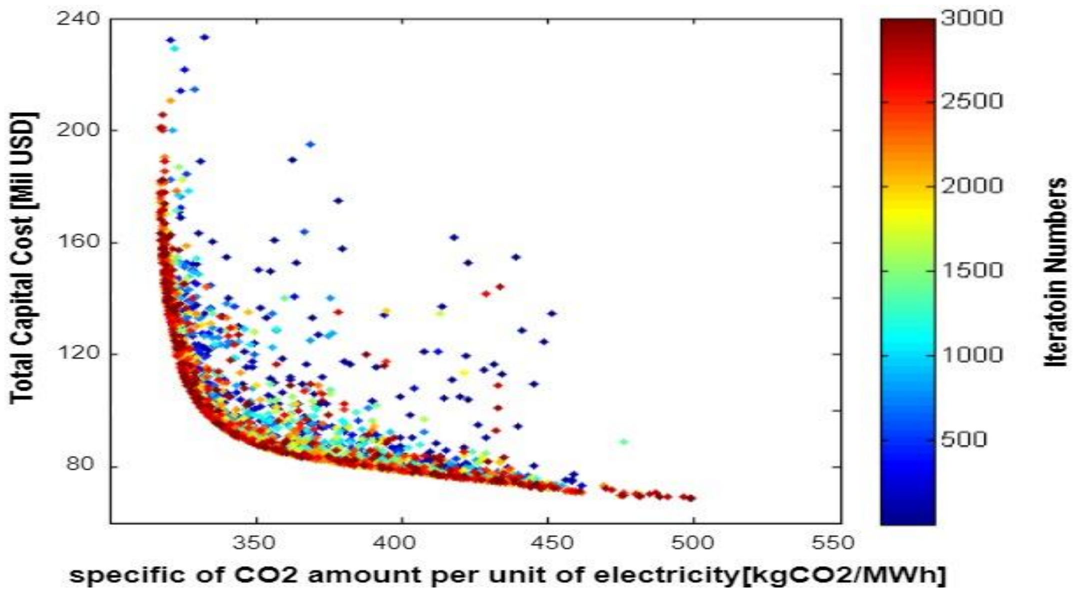

Figure 31: The optimization convergence algorithm of ABHGT

4.3.2. Plant Performance Using (POF). The tradeoff between the objective functions is shown clearly in Figure 32 where a decrease on the CO_2 emissions leads to an increase on the total capital cost.

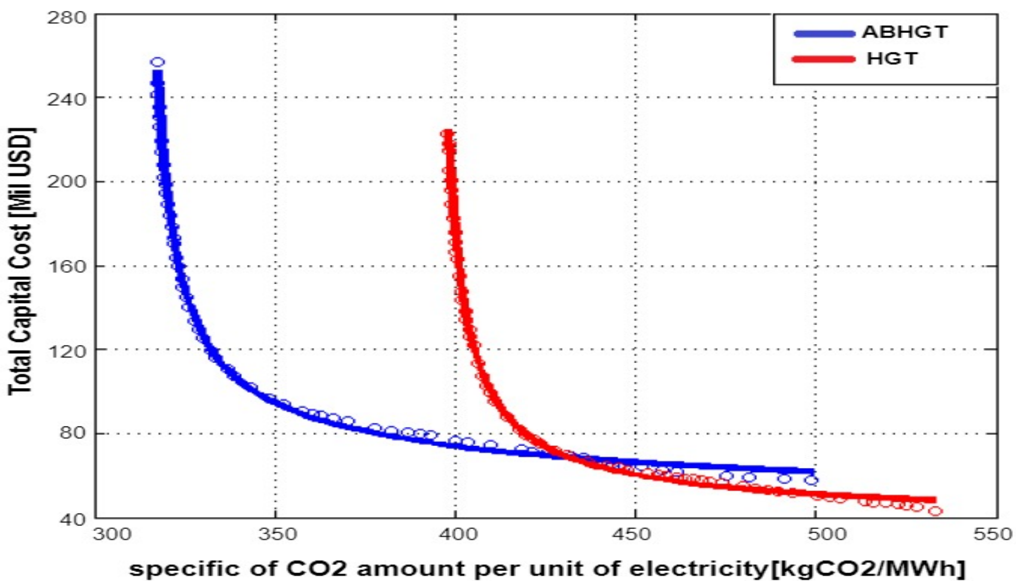

Figure 32: The Objective functions trade off of HGT and ABHGT

It can be noticed that the total capital cost is increasing linearly as the CO_2 emissions decreases till a certain point. This point is called the lower theoretical limit where decreasing the CO_2 emissions below this limit leads to an exponential increase in the total capital cost. The CO_2 emissions lower theoretical limits of HGT and ABHGT is 420 $kgCO_2/MWh$ and 325 $kgCO_2/MWh$ respectively. Moreover, it can be seen that ABHGT specific CO_2 emissions are lower than HGT emissions for a given total capital cost.

4.3.2.1 Thermodynamic performance indicator. The Thermodynamic efficiencies analyses are essential indicators to estimate the optimal performance of the power plant. Figure 33 illustrates the overall annual efficiencies versus the annual solar share. It can be seen that ABHGT and HGT efficiencies are decreasing linearly with increasing the solar share till a certain limit where an increase in solar share leads to an exponential decrease on both efficiencies. The higher theoretical limit for ABHGT and HGT is 22% and 20%, respectively. It can be noticed in both power plants models that the overall annual energy efficiencies are higher than the overall annual exergy efficiencies.

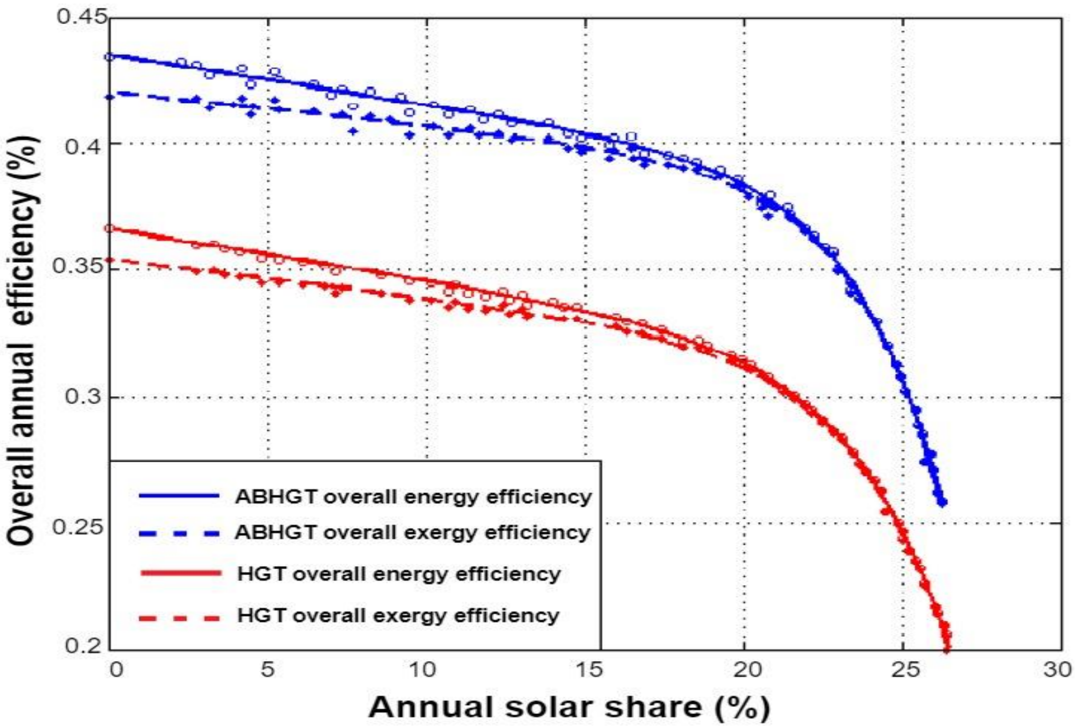

Figure 33: Overall annual efficiencies versus the annual solar share

Moreover, the difference between both efficiencies decreases as the annual solar share increases. The reason behind that is the fact that the power plants typically run on pure fuel gases at a lower solar share where fuel has more exergy content than energy content. Accordingly, the energy efficiency is higher than the exergy efficiency for producing the same power output. However, an increase in solar share leads to a decrease in energy efficiency and an increase in exergy efficiency since solar share has more energy content than an exergy content. Consequently, pure solar power plants have higher exergy efficiency than energy efficiency. In addition to that, ABHGT has higher overall annual energy and exergy efficiencies than HGT power plants. This is due to the built-in additional bottoming cycle for the ABHGT to enhance the overall efficiencies of the power plant.

4.3.2.2. Economic Performance Indicator. One of the most popular economic indicators for power plants performance is the levelized cost of electricity (LCOE). LCOE is used to measure the cost of electricity produced. It can be also defined as the cost of electricity sale which makes the net present value (NPV) of the investment equal to zero. The investment of the project would be more profitable if the LCOE is minimized. Figure 34 shows the effect of solar share on LCOE.

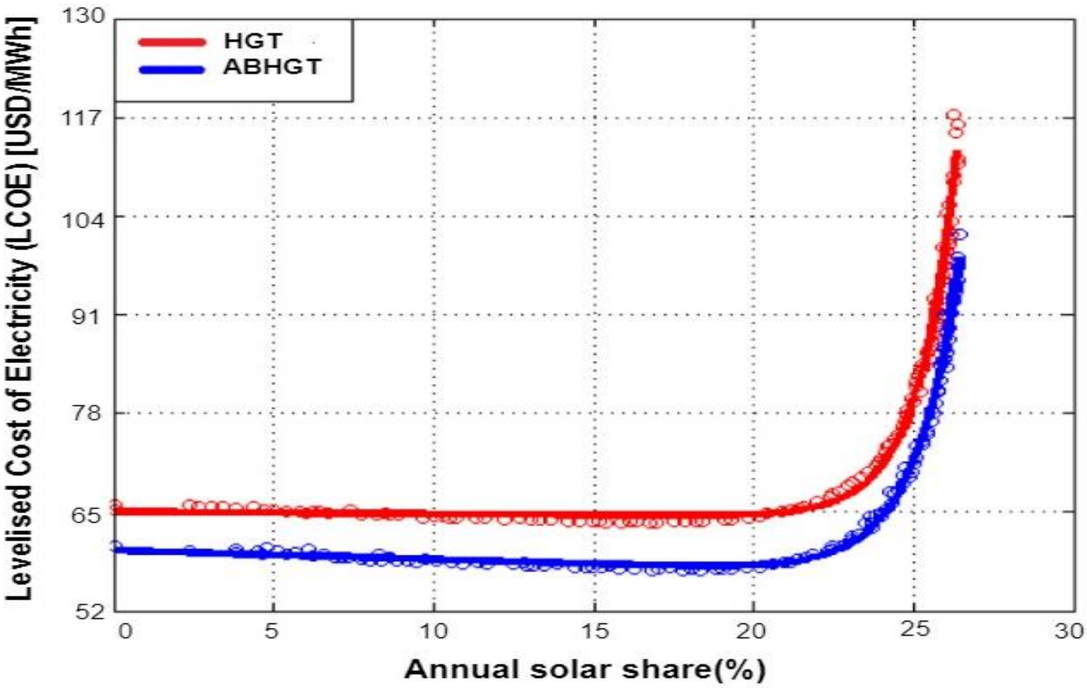

Figure 34: Levelised cost of electricity (LCOE) versus annual solar share

It can be noticed from Figure 34 that the LCOE is slightly decreasing as the solar share increases up until a certain limit where an increase in solar share leads to an exponential increase in LCOE. This is due to the fact that adding solar components to a certain solar share limit is more profitable than running the power plant purely with fuel gases. Moreover, it can be seen that the LOCE of ABHGT power plant is about 58 (USD /MWh) with a corresponding annual solar share of 22% while LCOE of HGT powerplant is about 65 (USD /MWh) with a solar share of 20%. Furthermore, the cost of electricity generated by ABHGT is always lower than HGT at any given annual solar share. This due to fact that the additional electricity profit produced by ABHGT overcomes the cost of building an additional bottoming cycle.

4.3.2.3 Environmental performance indicator. Reducing the CO_2 emissions is one of the main objectives in the current thesis. Reducing the CO_2 emissions means less reliance on fossil fuel that has a large impact on the climate change. The specific of CO_2 amount per unit of electricity emitted by the plant $\left(f_{CO_2}\right)$ is one of the key factors to the environmental indicators. The relation between Specific CO_2 emissions $\left(f_{CO_2}\right)$ and the LCOE is shown in Figure 35.

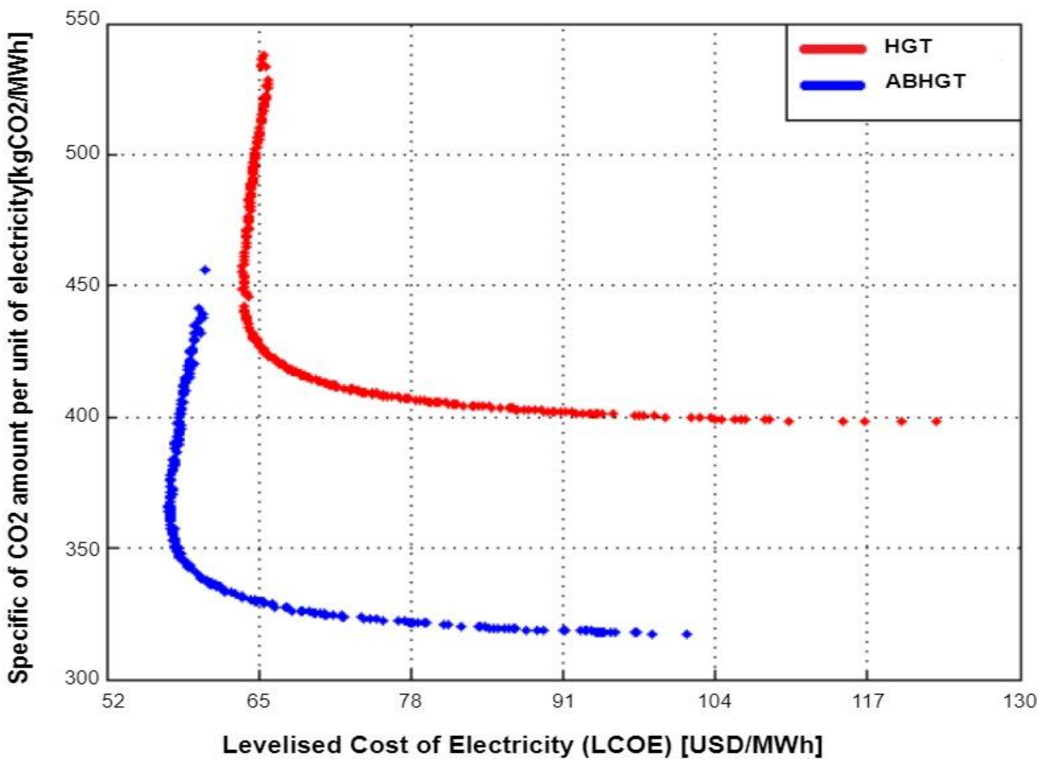

Figure 35: Specific CO2 emissions $\left(f_{CO_2}\right)$ versus LCOE

It can be noticed that both plants' specific CO_2 emissions $\left(f_{CO_2}\right)$ decrease with reducing the LCOE until a certain limit where decreasing $\left(f_{CO_2}\right)$ then leads to an exponential increase in LCOE. This theoretical limit illustrates that it's not worth it to invest more in LCOE in order to reduce more specific CO_2 emissions. The LCOE limits for ABHGT and HGT are 58.35 (USD /MWh) and 65.37 (USD /MWh) respectively. Moreover, it can be seen that ABHGT power plant emits less specific CO_2 emissions than HGT for a given LCOE. For example: at LCOE of 65 (USD /MWh), the ABHGT emits around 330 (kg CO_2/MWh) whereas HGT emits 425 (kg CO_2/MWh). This reduction on specific CO_2 emissions justifies the additional cost of the bottoming cycle.

4.3.2.4 Unified performance indicator. The optimization results of the two models (HGT and ABHGT) illustrate a diversity on different optimal configurations and designs. Different performance indicators are taken into consideration to evaluate the optimization problem.

One might argue that minimizing the LCOE and maximizing the NPV of the power plants leads to an optimal design parameter. Another person can argue from another perspective that minimizing the specific CO_2 emissions or maximizing the annual overall efficiencies leads to an optimal design parameter. To overcome this issue, a unified performance indicator is introduced to select an optimal design accordingly. Degree of penalty cost due to avoidance of CO_2 emissions is selected as a unified performance indicator to select an optimized configuration with optimal design variables. This performance indicator is significantly selected since it accounts for both economic and environmental performance indicators. The unified performance indicator is computed by the following equation [2]:

$$Z_{Co_2} = \frac{LCOE - LCOE_{ref}}{f_{Co_2} - fco_{2\,ref}} \tag{106}$$

where Z_{Co_2} is the degree of penalty cost due to CO_2 emissions avoidance in (USD/ton), $LCOE_{ref}$ is the Levelized cost of electricity in (USD/MWh), and $fco_{2\,ref}$ is the Specific of CO_2 emissions in (ton/MWh) of the reference cycle. The reference cycle is the Cycle that is running with Zero solar share. Figure 36 illustrates the degree of penalty cost due to CO_2 emissions avoidance versus annual solar share for both ABHGT and HGT configurations.

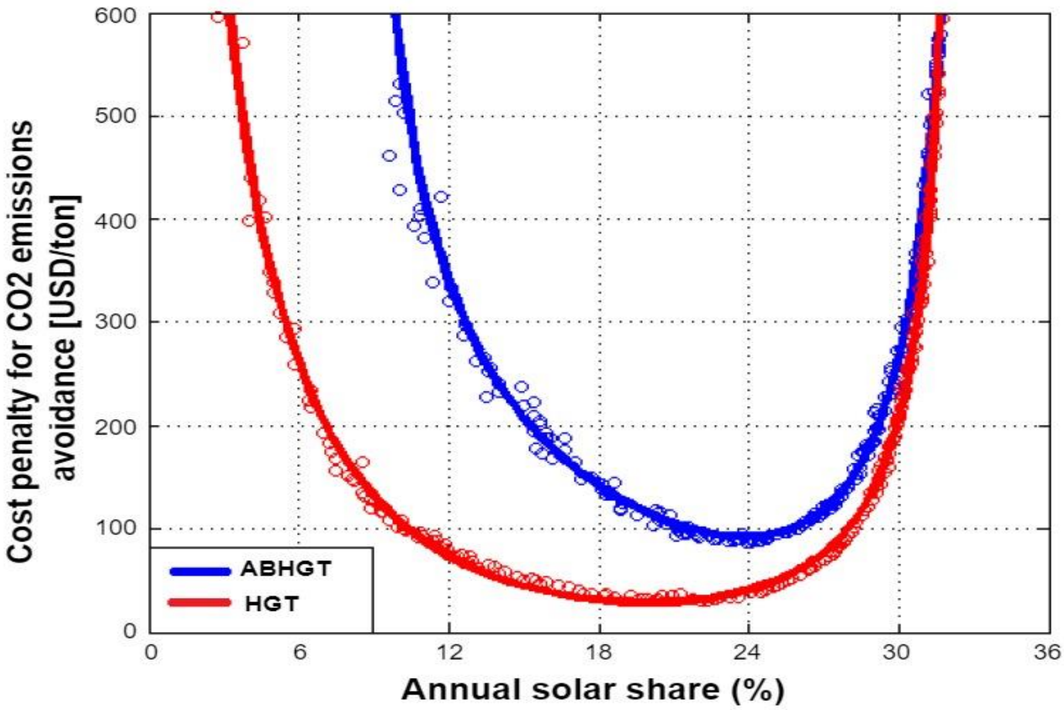

Figure 36: CO2 emissions penalty cost versus annual solar share.

It can be noticed that the minimum degree of penalty cost due to CO_2 emissions avoidance (Z_{Co_2}) of ABHGT power plant is 90 (USD/ton) at 22% annual solar share whereas the minimum degree of penalty cost due to CO_2 emissions avoidance (Z_{Co_2}) of HGT is 32 (USD/ton) at 20% annual solar share. Accordingly, the optimal design variables are selected based on minimizing the degree of penalty cost due to CO_2 emissions avoidance (Z_{Co_2}) with its corresponding annual solar share. Furthermore, it can be seen that the penalty cost due to CO_2 emissions avoidance (Z_{Co_2}) of ABHGT is higher than HGT for a given annual solar share. The reason behind that is that the LCOE of ABHGT running without solar share is substantially lower than running it with 22% annual solar share, while the LCOE of HGT running without solar share is almost the same cost as running it with 20% annual solar share.

4.3.3. Optimal plant performance results. The optimal design variables and parameters of HGT and ABHGT power plants are listed in Table 18. By comparing both power plant configurations, it can be noticed that the number of PTSCs units and PTSCs aperture area of HGT is lower than ABHGT since solar share is lower in HGT. The optimal Number of PTSC of ABHGT is 396 units while HGT is 360 units.

The PTSCs aperture area of ABHGT is 10% bigger than HGT due to the difference in solar share. Most of the topping cycle optimal parameters are validated in steady state section. Moreover, the optimal decision variables of the optimization problem are closely equal to nominal parameter variables. For example, the optimal bottoming compressors pressure ratio is 2.6:1 which is almost equal to the nominal value (2.5:1). All the optimal decision variables are obtained from the values that are lying on the POF curve. Additionally, the minimum approach temperature (MAT) of heat exchanger varies based on the component type. For instance, the intercooler MAT is about 6.5 °C whereas the heat waste and recuperator MATs are 19 °C and 21.5°C respectively. The reason behind this difference is that the heat exchanger effectiveness depends on the aperture area that is related to the cost function of the model. As a matter of fact, the intercooler has the lowest capital cost as it requires low aperture area due to the fact that it runs under low pressure and temperature. Furthermore, the capacity factor for both power plants are around 62.5% with annual operating hours of 5475 hours. The optimal Performance of HGT and ABHGT power plants are listed in Table 19. By comparing both power plant configurations, it can be noticed that an addition of bottoming cycle on ABHGT power plant increases the power output by 10 (MW).

Table 18: Optimal parameters of the power plants

Design parameters	**HGT**	**ABHGT**
Compressor pressure ratio (bottoming)	-	2.6
Number of PTSC (NPTSC) in [units]	360	396
PTSC aperture area in [m^2]	53935	59329
Intercooler Minimum Approach Temperature (MAT) [°C]	-	6.5
Heat waste Recovery (MAT) [°C]	-	19
Recuperator (MAT) [°C]	-	21.5
Exhaust Turbine Mass Flow Top in [kg/s]	134.2	134.2
Firing Temperature in [K]	1673	1673
Compressor pressure ratio (Top)	21.1:1	21.1:1
Capacity Factor %	62.5	62.5
Power plant annual operating hours in [hr]	5475	5475

The Annual Electricity output in HGT and ABHGT power plants are 257.3 (GWh/year) and 312 (GWh/year) respectively. It can be noticed in both power plant models that the overall annual energy efficiency is higher than the overall annual exergy efficiency. Moreover, the difference between both efficiencies decreases as the solar share increases. That is due to the fact that power plants mostly run on fuel gases at a lower solar share where fuel has more exergy content than energy content. Accordingly, the energy efficiency is higher than the exergy efficiency for producing the same power output. The annual overall energy and exergy efficiencies of ABHGT are 38.5% and 38.3% where as HGT annual overall energy and exergy efficiencies of HGT are 32.5% and 32.3%.

Table 19: Optimal performance of the power plants

Design performance	**HGT**	**ABHGT**
Optimal Power Output [MW]	47	57
Annual power Output [GWh/year]	257.3	312.1
Capacity Factor %	62.5	62.5
Number of PTSC (NPTSC) [units]	360	396
Annual optimal Solar Share %	20	22
Nominal Solar Share %	46	46
Bottoming Cycle Electrical Share %	-	17.5
Annual Overall Energy Efficiency %	32.5	38.5
Annual Overall Exergy Efficiency %	32.3	38.3
Cycle Energy Efficiency %	37.6	44.5
Cycle Exergy Efficiency %	37.3	44.2
Specific CO_2 Emissions [kg CO_2/MWh]	451.5	351.5
Cost penalty for CO_2 Avoidance [USD/tonCO_2]	32	90
Specific Water Consumption [ltr /MWh]	24.9	25.1
Total Capital Cost [Mil USD]	80.6	100.5
Levelized Cost of Electricity [USD/MW]	65.374	58.35
Net Present Value (NPV) [Mil USD]	103.924	151.858

Additionally, a noticeable increase on cycle energy efficiencies on both power plants since the solar share is reduced. Furthermore, the LCOE of ABHGT is lower than HGT despite the fact that total capital cost of ABHGT is higher than HGT power plant. The LCOE of ABHGT and HGT are 58.35 (USD/MW) and 65.37(USD/MW) respectively. Both of the power plants have positive NPV, where the NPV of HGT and ABHGT is 103.9 (Mil USD) and 151.8 (Mil USD) correspondingly. This is due to the fact that the fuel cost in UAE is cheap enough to make the investment profitable. The Specific CO_2 emissions of ABHGT is 22% lower than HGT. Reducing the CO_2 emissions is one of the main objectives in the current thesis. The specific of CO_2 amount per unit of electricity emitted by the plant (f_{CO_2}) is one of the key factors to the environmental indicators. Thus, reducing the CO_2 emission means less reliance on fossil fuel that has large impact on the climate change.

4.3.4. Total capital cost breakdown of power plants. The Total capital cost breakdown of ABHGT and HGT power plants is shown in Table 20. Figures 37 and 38 illustrate the total capital cost breakdown of HGT and ABHGT models in pie charts.

It can be noticed that both power plants have almost 60% contribution of total equipment cost whereas the rest of contributions go to land, contingencies, civil engineering, and pipeline branching costs. Moreover, it can be seen that the PTSCs contribution in total equipment cost is not high. This is due to the fact that air is used as heat transfer fluid and the optimized annual solar share is considerably low. Despite the slight increase on PTSC cost of ABHGT, the solar cost contribution to total capital cost is still lower than HGT by 1%. The most expensive component in both configurations is the top gas turbine cost. The Gas Turbine cost contribution to the total capital cost is about 27% for HGT and 17% for ABGHT. Furthermore, it can be seen that the heat waste recovery, intercooler and recuperator costs contribution to the total capital cost are about 17.5%.

4.3.5. Levelized cost breakdown of power plants. The levelized cost of electricity (LCOE) breakdown of ABHGT and HGT power plants are shown on Table 21. It can be noticed in both power plants that the annualized capital cost and fuel cost are the main share contributors to the LCOE.

Table 20: Total capital cost breakdown of the power plants

Capital cost break down	**ABHGT [Mil US $]**	**HGT [Mil US $]**
PTSC total price	2.1	2
Top Gas Turbine	17.5	17.5
Bottom Gas Turbine	8	0
Top Compressor	6.8	6.8
Bottom Compressors (LP and HP)	0.6	0
Generators	5.1	4
Electronics	9	8
Heat waste recovery	12.5	0
Intercooler with Fan	2.7	0
Recuperator	2.4	0
Total Equipment cost	**66.7**	**38.3**
Civil Engineers and Pipe Branching	16	14
Land	6	4.8
Contingencies	11.8	9.5
Total Capital Cost	**100.5**	**66**

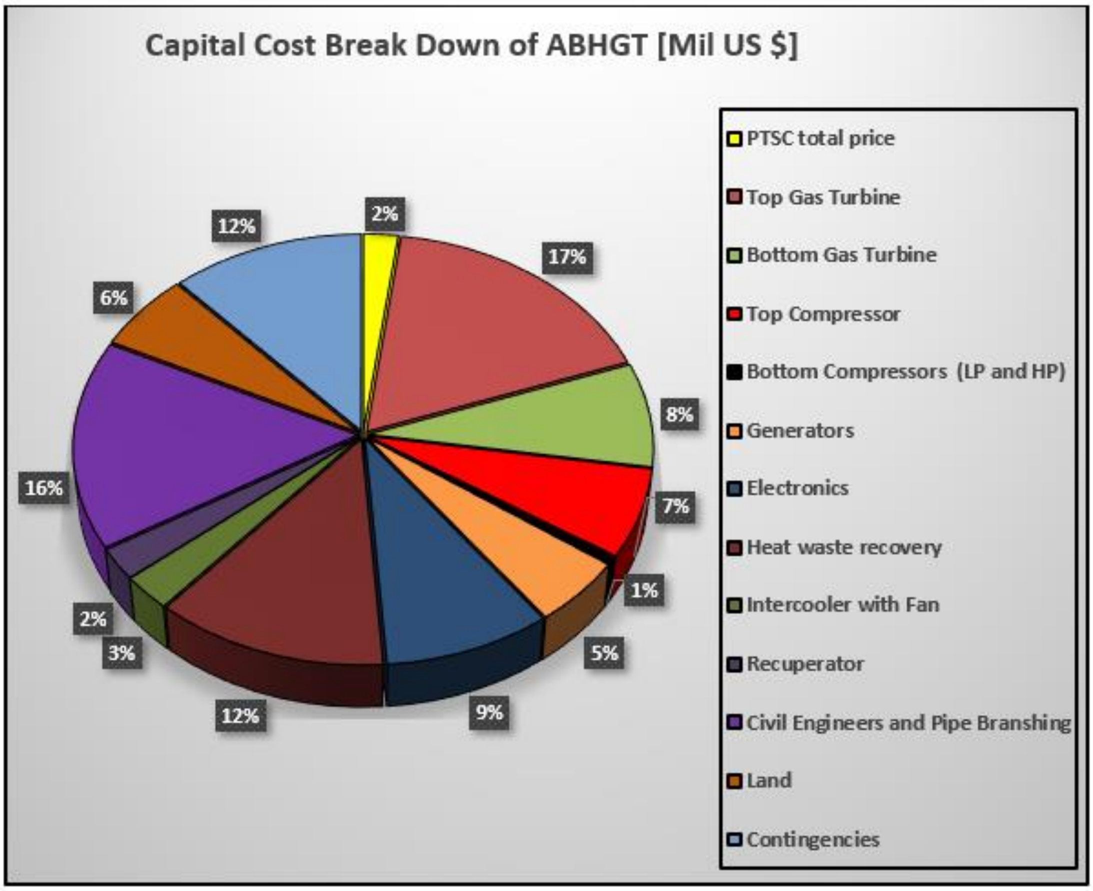

Figure 37: Total capital cost Breakdown of ABHGT

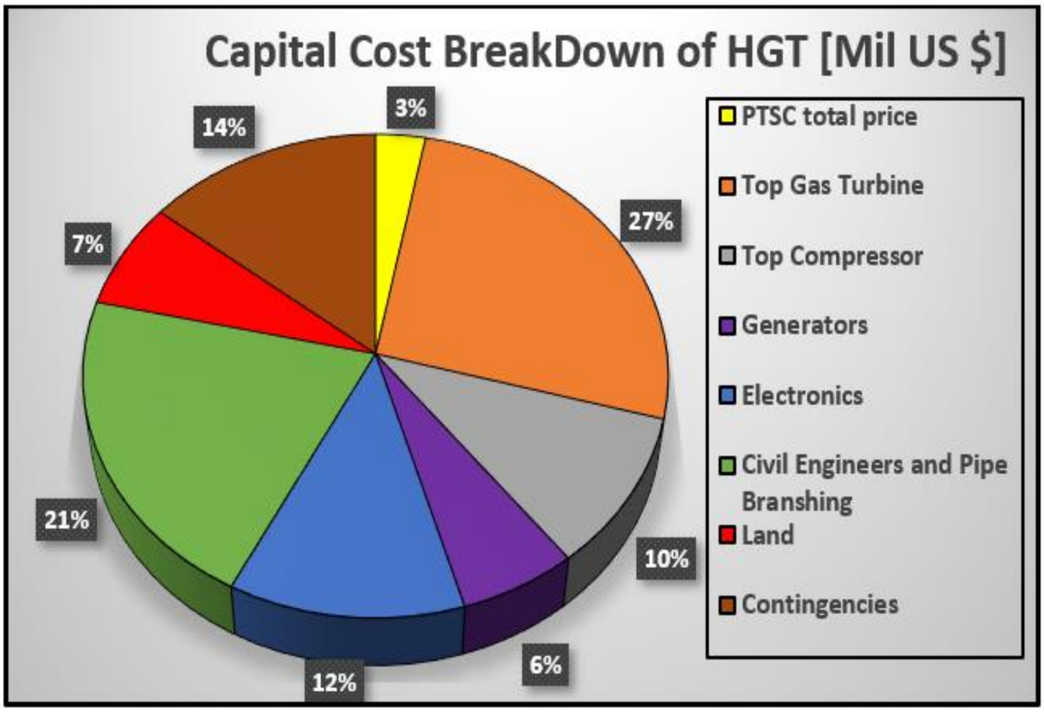

Figure 38: Total capital cost Breakdown of HGT

The annualized capital cost and fuel cost of ABHGT are 30.9 (USD/MWh) and 17.6 (USD/MWh) whereas the annualized capital cost and fuel cost of HGT are 24.4 (USD/MWh) and 31.5 (USD/MWh) respectively. Moreover, the additional annualized capital cost of bottoming cycle of ABHGT is remunerated by the annualized fuel cost reduction at the topping cycle. Accordingly, LCOE of ABHGT power plant is lower than HGT power plant by 7 (USD/MWh). Additionally, the annualized water cost in both power plants is almost negligible since the gas turbine power plants do not rely on water.

Table 21: The levelized cost breakdown of power plants

Levelized cost of electricity break down	**ABHGT**	**HGT**
Total capital cost [Mil US $]	100.5	66.6
Annualized Capital Cost [USD/MWh]	**30.9**	**24.8**
Annual Water cost [Mil US $]	0.0156	0.0129
Annualized water cost [USD/MWh]	**0.05**	**0.05**
Annual Fuel (NG) cost [Mil US $]	5.49	8.1
Annualized fuel cost [USD/MWh]	**17.6**	**31.5**
Annual Operation and Maintenance [Mil US $]	3.03	2.32
Annualized Operation and Maintenance [USD/MWh]	**9.7**	**9**
Total Decommissioning [Mil US $]	2.1	0.5
Annualized Decommissioning [USD/MWh]	**0.1**	**0.024**
Total LCOE [USD/MWh]	**58.35**	**65.374**

4.3.6. Net present value breakdown of power plants. The net present value (NPV) breakdown of ABHGT and HGT power plants are shown in Table 22. Figure 39 illustrates the NPV breakdown of ABHGT in bar chart. It can be noticed in both configurations that the NPV is positive which means that the generated revenues by electricity production in both power pants overcome the investment expenses. Indeed, the additional bottoming cycle increases the NPV of ABHGT by 47.9 (Mil USD). The generated revenues by electricity production and Fuel cost are the main contributors to the total NPV. Accordingly, these two main contributors play a dominant effect on NPV of the power plant. Furthermore, the NPV and LCOE of ABHGT will be analyzed more in the sensitivity analysis.

Table 22: The Net Present Value (NPV) breakdown of the power plants

Net present value cost Breakdown	**ABHGT [Mil US $]**	**HGT [Mil US $]**
capital cost contribution	112.2	74.36
Decommissioning	0.362	0.086
Revenues	363.7	299.8
Fuel (NG) cost contribution	63.98	94.39
Operation and Maintenance	35.3	27.04
Total NPV	**151.858**	**103.924**

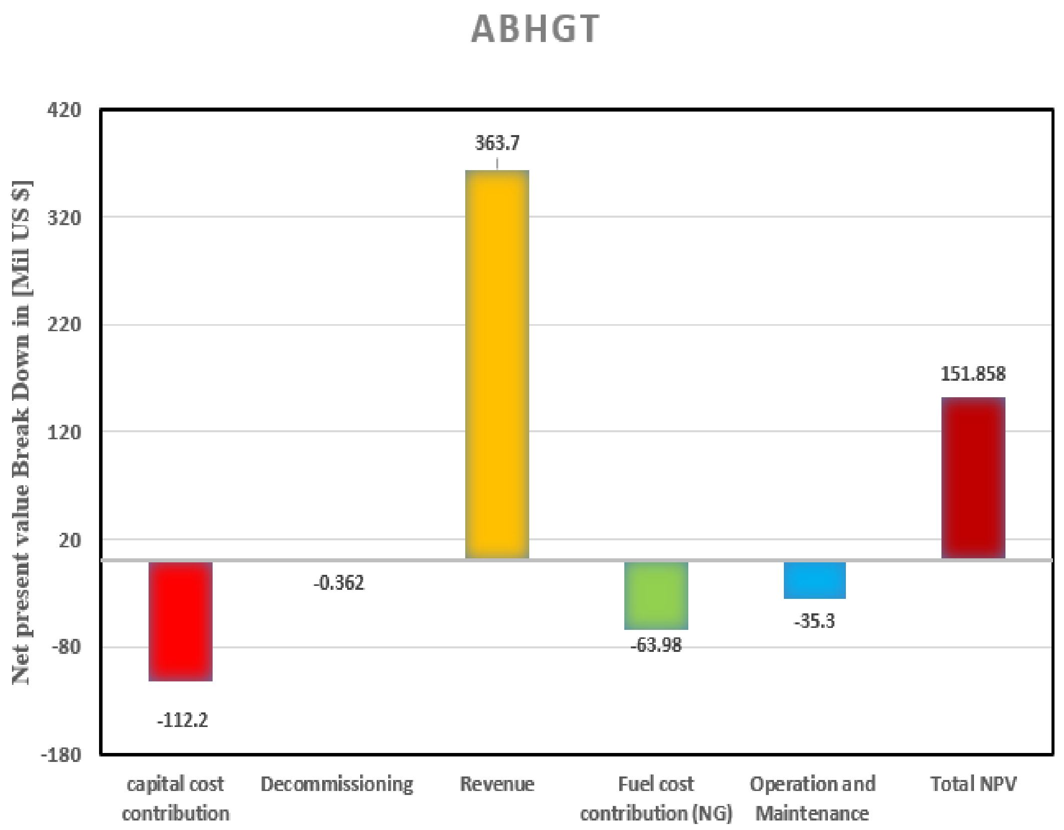

Figure 39: The Net Present Value (NPV) breakdown of ABHGT

4.3.7. Sensitivity analysis. Sensitivity analysis is used to study the economic behavior of the power plant by varying the economic parameters to a certain extent. The sensitivity analysis is applied to ABHGT power plant to study its economic value and indicate the most sensitive parameters that have dominant effect on the economic analysis. Accordingly, LCOE and NPV are chosen as economic indicators for the sensitivity analysis. A uniform change in the economic parameters is implemented to analyze the effect on the economic performance indicators.

4.3.7.1. Sensitivity analysis on LCOE of ABHGT. A comparative sensitivity analysis on LCOE of ABHGT is presented through tornado diagram. Figure 40 illustrates a tornado diagram portraying the sensitivity analysis on the LCOE by ±30% alteration in economic parameters of ABHGT. The sensitivity analysis of economic parameters are capital cost, solar cost, fuel cost, operation and maintenance cost, and decommissioning cost. The reference point of the sensitivity analysis is defined by the white line at the middle of the tornado chart where its LCOE is equal to 58.3 (UD/MWh).The sensitivity analysis effect on LCOE is presented on percentage with respect to its reference value. It can be noticed that the capital and fuel cost are the most sensitive parameters which have major effects on LCOE of ABHGT.

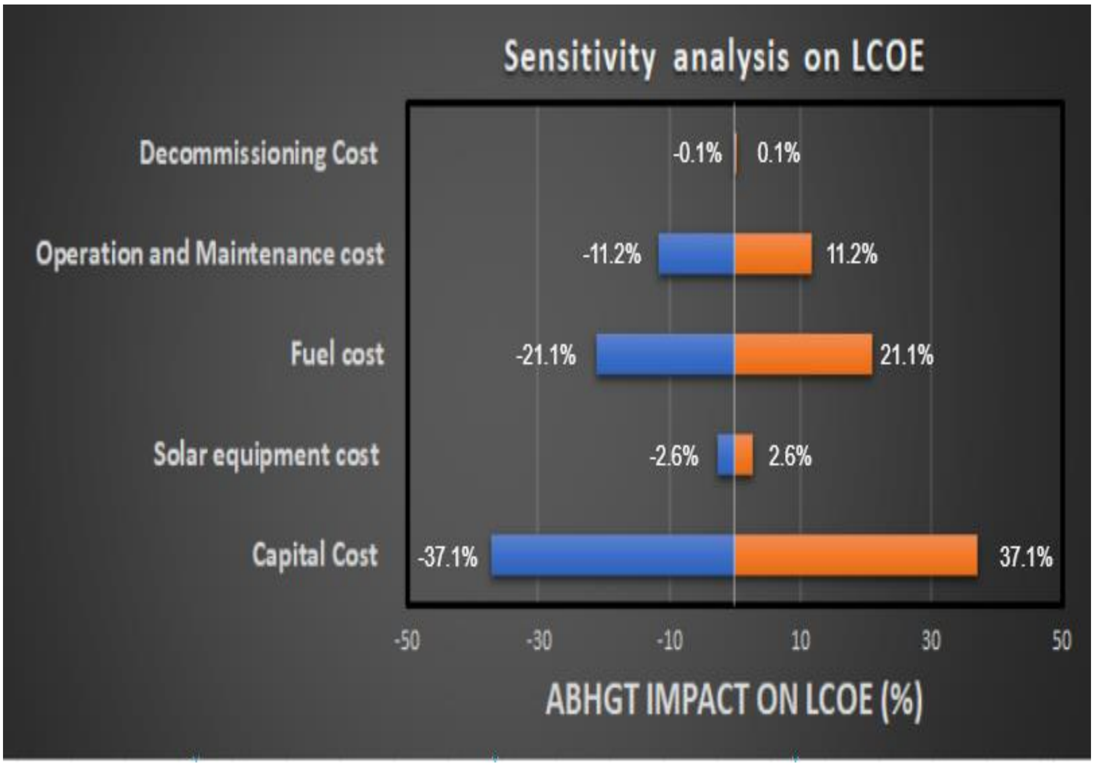

Figure 40: Sensitivity analysis on the LCOE by ±30% alteration in economic parameters of ABHGT

Applying ±30% alteration to the reference capital cost and fuel cost result on 37.1% and 21.1% change on LCOE of ABHGT respectively. However, applying ±30% change to the reference solar cost lead to a change of 2.6 % on LCOE of ABHGT. This is due to the fact that ABHGT power plant has a low annual solar share. Moreover, an increase on fuel cost illustrates a huge effect on the LCOE which generates a huge risk on the market.

4.3.7.2. Sensitivity analysis on NPV of ABHGT. Another comparative sensitivity analysis on NPV of ABHGT is presented through the tornado diagram. Figure 41 illustrates a tornado diagram portraying the sensitivity analysis on the NPV by ±30% alteration in economic parameters of ABHGT. The sensitivity analysis economic parameters are similar to the LCOE parameters.

The reference point of the sensitivity analysis is defined by the white line at the middle of the tornado chart where its NPV is equal to 151.858 (Mil USD). It can be seen that capital cost and fuel cost contributions are the most sensitive parameters which have major effects on NPV of ABHGT. Applying ±30% alteration to the reference capital cost and fuel cost result in a 51.7% and a 29.5% change on NPV of ABHGT respectively. Nevertheless, solar equipment cost, and decommissioning cost are less sensitive to the NPV since ABHGT relies more on fuel and has a lower annual solar share.

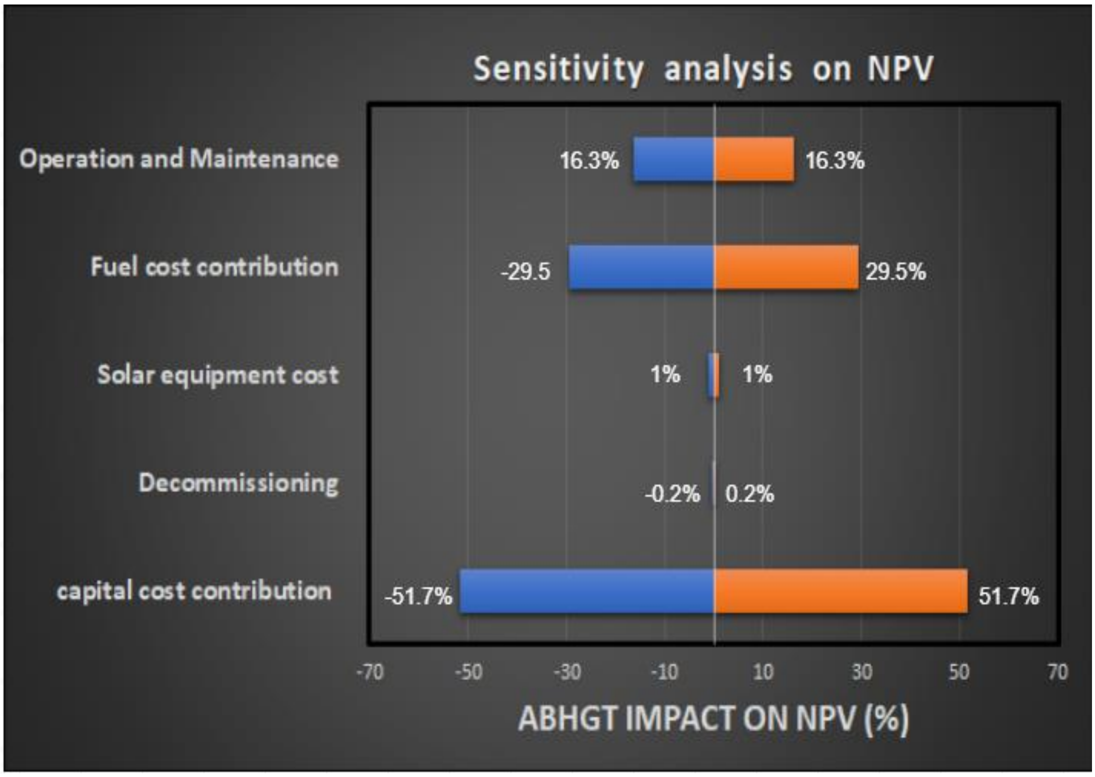

Figure 41: Sensitivity analysis on the NPV by ±30% alteration in economic parameters of ABHGT

4.3.7.3. Sensitivity analysis on fuel cost of ABHGT. Natural gas impact on LCOE and Natural gas cost share over LCOE are shown in Figure 42. The reference point of the natural gas cost is defined by the gray line.

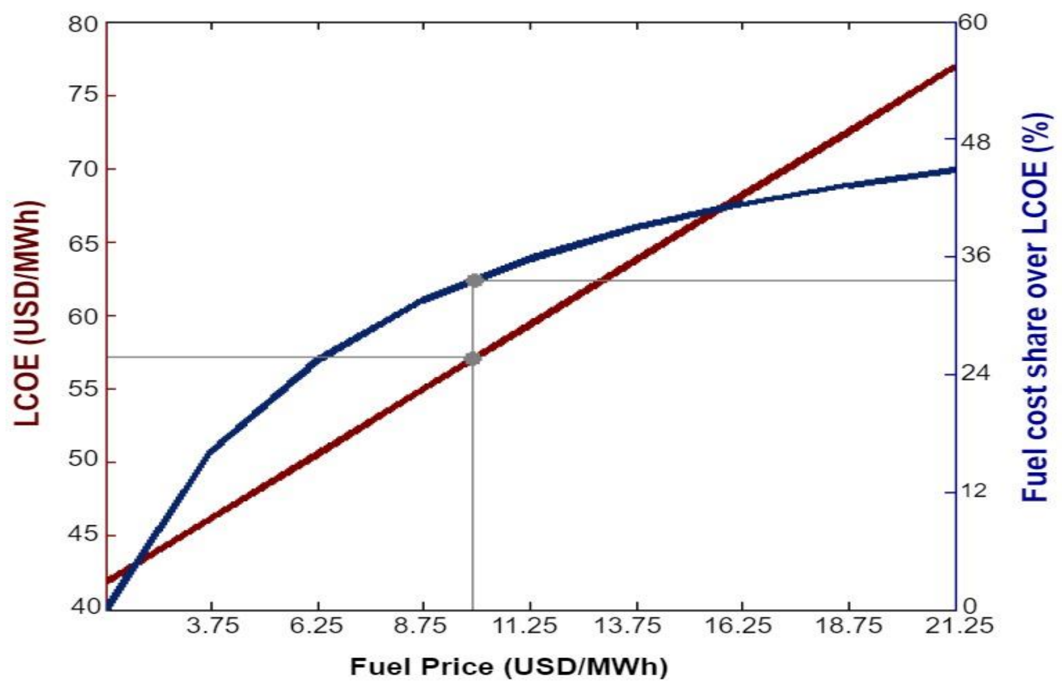

Figure 42: Natural gas impact on LCOE

It can be noticed that LCOE of ABHGT is increasing linearly as the fuel cost increases. The fuel cost is a sensitive economic parameter where a slight increase on its price leads to a significant change in LCOE. This is due to the fact that ABHGT power plant relies more on natural gas. The natural gas price in UAE is about 10 USD/MWh which corresponds to LCOE of 58 USD/MWh, where an increase by 5USD/MWh in the price of natural gas leads to a significant increase in LCOE by 8 USD/MWh. Moreover, it can be seen that the fuel cost share over LCOE increase as the natural gas price slope decreases.

Figure 43 illustrates the natural gas impact on NPV. It can be seen that the NPV of ABHGT is decreasing linearly as the fuel cost increases. The reference point of the natural gas cost is defined by the gray line. The reference natural gas price on UAE is about 10 USD/MWh which corresponds to NPV of 151.8 (Mil USD), where an increase by 5USD/MWh on price of natural gas leads to a significant decrease in NPV by 32 (Mil USD). Thus, the low fuel cost makes the ABHGT investment worth taking in

UAE. However, applying this investment in different regions such as Europe would result on lower NPV due to high fuel cost in these regions.

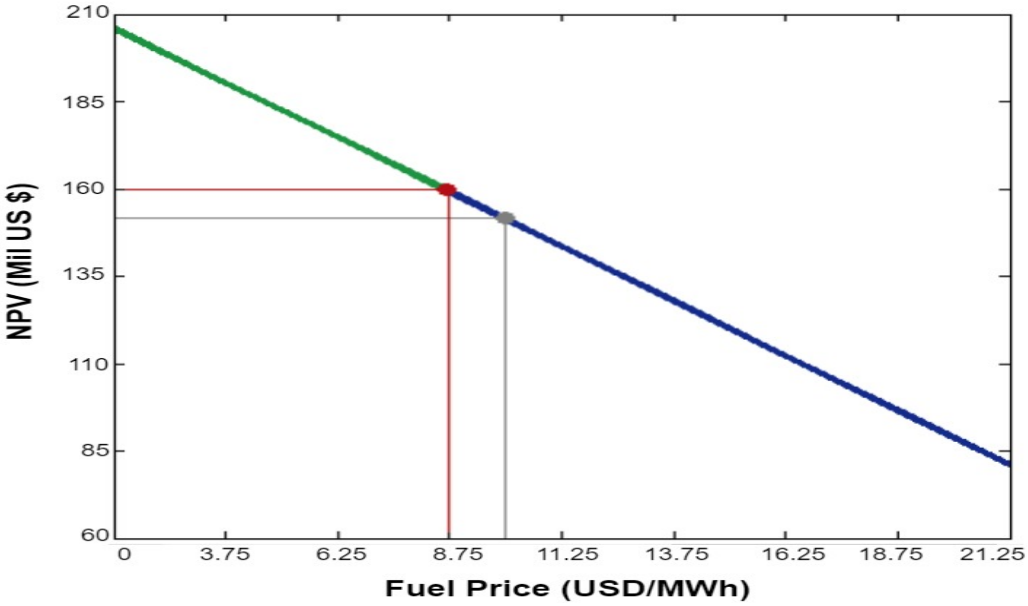

Figure 43: Natural gas impact on NPV

4.3.7.4. Sensitivity analysis of LPG performance on ABHGT. One of the main problems that is facing the energy sector in the upcoming years is the risk of natural gas depletion. Among the high demand on natural gases these days, running the power plants with Liquified Petroleum Gas (LPG) can be one of the promising alternative solutions to overcome the natural gas depletion threats. One of the main advantages of using LPG is its vast abundance due to the fact that LPG is mainly propane which can be chemically extracted.

A comparative performance analysis of LPG and natural gas on ABHGT is summarized on Table 23. It can be noticed that LPG is more dense than air with a relative density of 1.52:1 whereas natural gas is lighter than air with a relative density of 0.554:1. Infact, the lower heating value of LPG is lower than the natural gas where the lower heating value of LPG is about 46.6 (MJ/kg) while the natural gas is 50 (MJ/kg). Accordingly, to produce the same power output, more mass flow rate is needed for LPG to compensate for the difference in lower heating values. Moreover, LPG has more carbon content than natural gas. Therefore, it emits more specific CO_2 emissions than natural gas where LPG Specific CO_2 emissions (f_{CO_2}) is equal to 411

(Kg/MWh) and natural gas (f_{CO_2}) is equal to 351.5 (Kg/MWh).Additionally, it can be noticed that natural gas cost is cheaper than LPG by 5 USD /MWh. Consequently, annualized fuel cost of natural gas is cheaper by 8.8 (USD/MWh). Furthermore, ABHGT running with LPG will have a decrease on NPV by 32 (Mil US $). The NPV break down of ABHGT running with LPG is illustrated by a bar cart in Figure 44.

Table 23: LPG and Natrual gas performance on ABHGT

Fuel Type in ABHGT	**Liquified Petroleum Gas (LPG)**	**Natural Gas**
Chemical Formula	C_3H_8	Ch_4
Fuel Density to air	1.52:1	0.554:1
Lower heating value (MJ/kg)	46.607	50
Mass flow rate (kg/s)	2.15	2
Cost of fuel in UAE (US $ /MWh)	15	10
Carbon content	0.817	0.75
Specific CO_2 emissions (Kg/MWh)	411	351.5
Annual fuel cost (Mil US $)	8.229	5.490
Annualized fuel cost (USD/MWh)	26.4	17.6
LCOE (USD/MWh)	67.15	58.35
NPV (Mil US $)	119.9	151.858

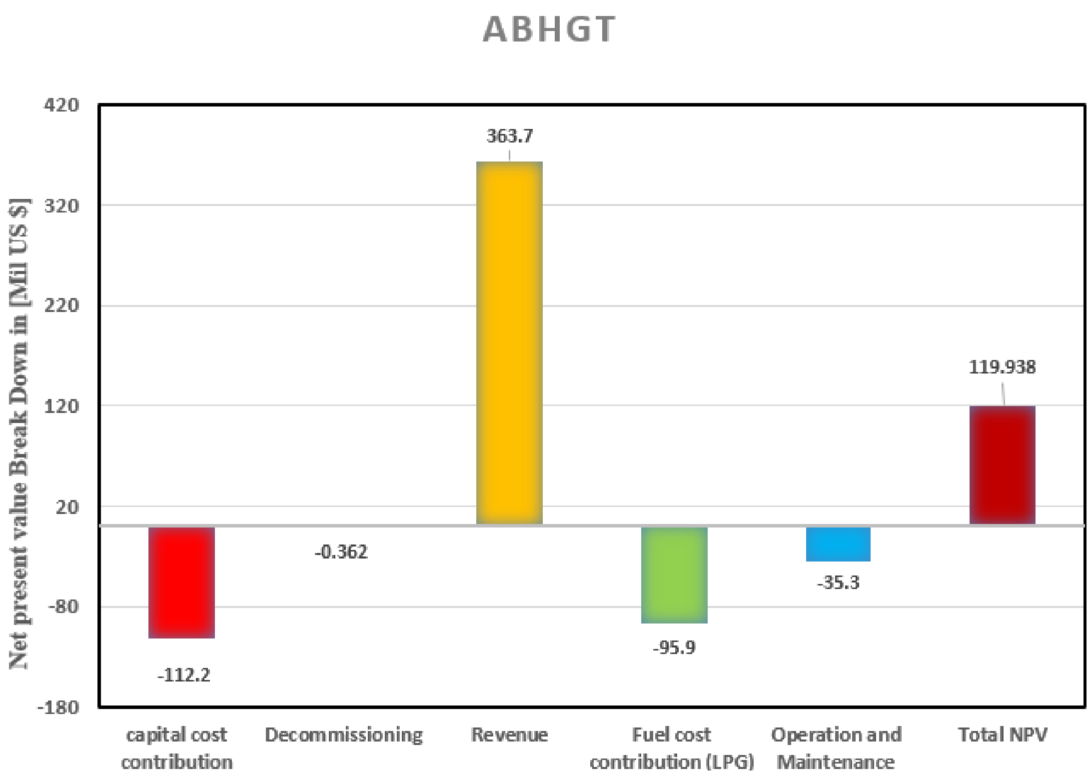

Figure 44: Net present value breakdown of ABGHT running with LPG

Although the natural gas is cheaper than LPG, the natural gas is not recommended to be used in the upcoming years due to the depletion effect. LPG will be more feasible in the future since it can be chemically extracted. Consequently, sensitivity analysis of using LPG as fuel on ABHGT is important to analyze the LPG cost contribution to the LCOE and NPV. A comparative sensitivity analysis on LCOE of ABHGT running with LPG is presented through the tornado diagram. Figure 45 illustrates a tornado diagram portraying the sensitivity analysis on the LCOE by ±30% alteration in economic parameters of ABHGT running with LPG. The sensitivity analysis economic parameters are: capital cost, solar cost, fuel cost, operation and maintenance cost, and decommissioning cost. The reference point of the sensitivity analysis is defined by the white line at the middle of the tornado chart where its LCOE is equal to 67.15 (UD/MWh). The sensitivity analysis effect on LCOE is presented as a percentage with respect to its reference value. Applying ±30% alteration to the reference capital cost and fuel cost results in a 32.2% and a 27.5% change in the LCOE of ABHGT respectively. It can be noticed that the capital and fuel cost are the most sensitive parameters which have major effects on LCOE of ABHGT running with LPG.

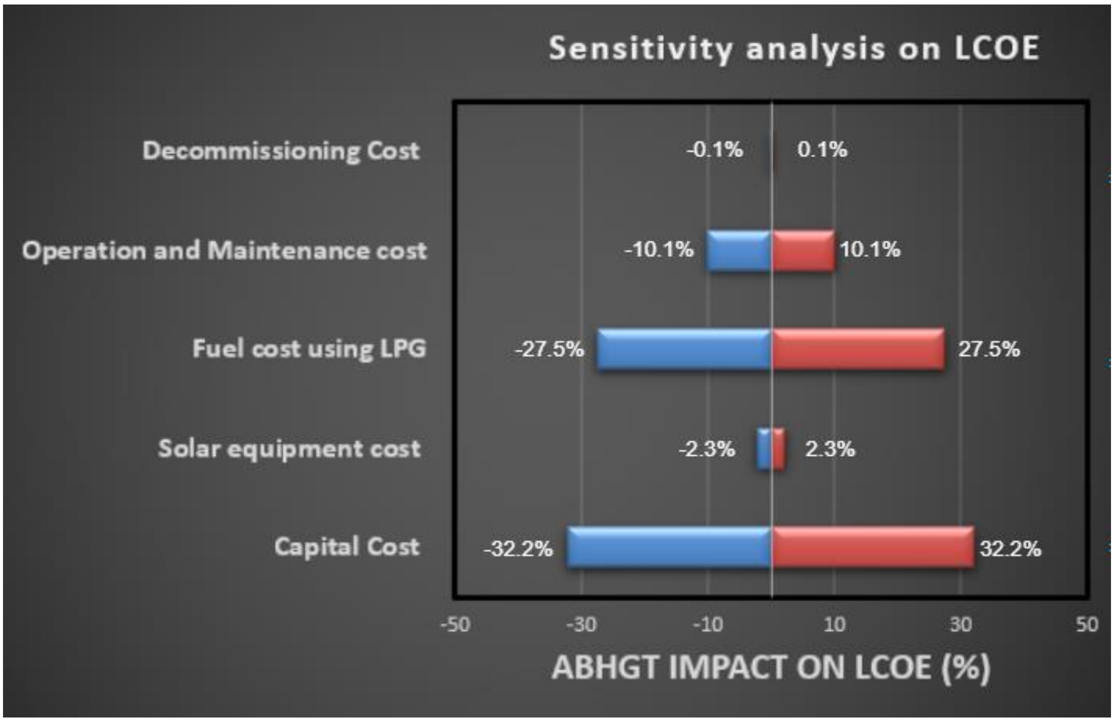

Figure 45: Sensitivity analysis on the LCOE by using LPG as fuel on ABHGT

Another comparative sensitivity analysis on NPV of ABHGT running with LPG is presented through a tornado diagram. Figure 46 illustrates a tornado diagram portraying the sensitivity analysis on the NPV by ±30% alteration in economic parameters of ABHGT running with LPG. The sensitivity analysis economic parameters are similar to the LCOE parameters. The reference point of the sensitivity analysis is defined by the white line at the middle of the tornado chart where its NPV is equal to 119.9 (Mil USD). It can be seen that capital cost and fuel cost contributions are the most sensitive parameters which have major effects on NPV of ABHGT. Applying ±30% alteration to the reference capital cost and fuel cost result in a 65.5% and a 56% change in the NPV of ABHGT respectively. Nevertheless, the solar equipment and decommissioning costs are less sensitive to the NPV since ABHGT relies more on fuel and has a lower annual solar share.

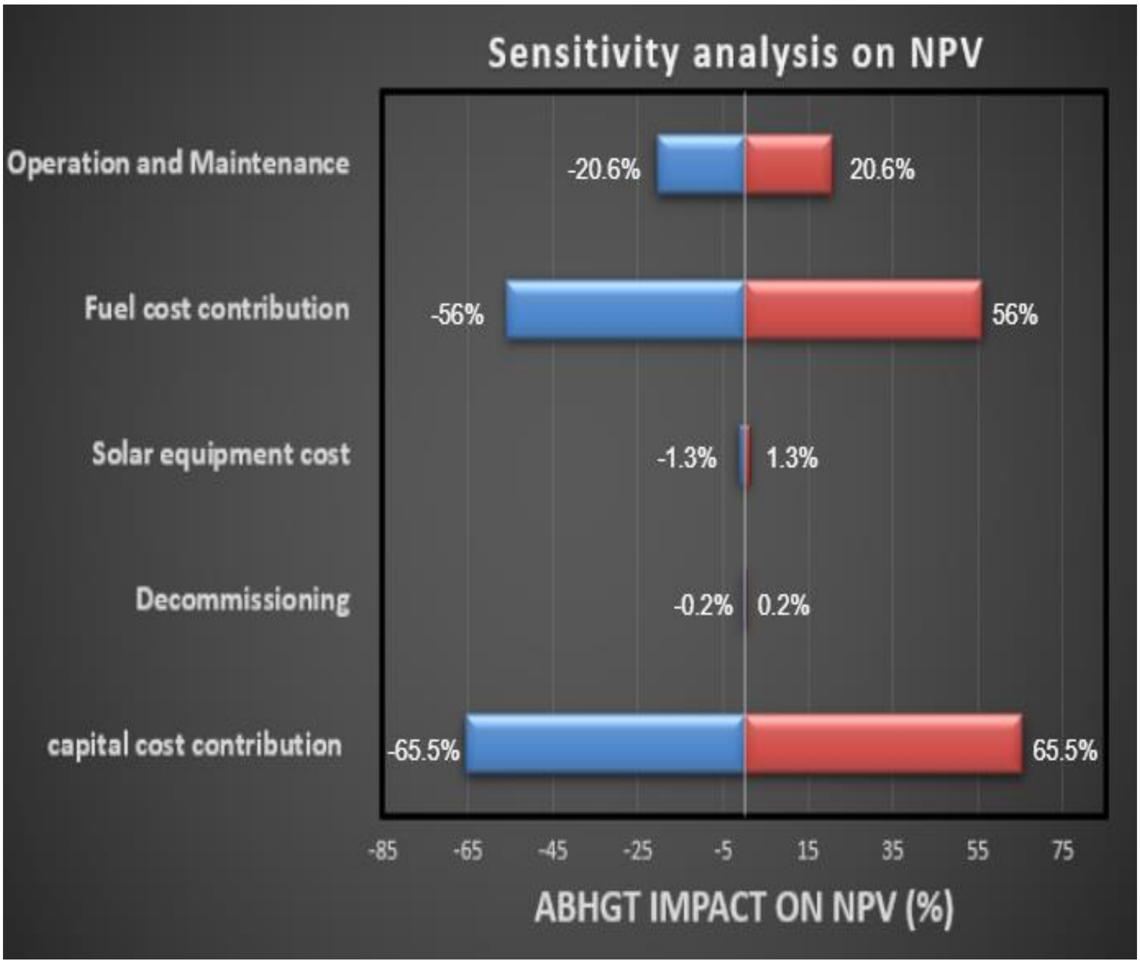

Figure 46: Sensitivity analysis on the NPV by using LPG as fuel on ABHGT

4.4. Compressed Air Energy Storage

The structure of this section will begin with compressed air energy storage (CAES) history and literature which will be discussed from sub-section (4.4.1-4.4.9). Two proposed configurations are presented at sub-section 4.4.10. The mathematical model of the CAES and the Salt cavern will be illustrated at sub-section 4.4.11.

4.4.1. CAES history. Compressed Air Energy Storage (CAES) has reaped a lot of interest due to the small capital expense, efficiencies, and high energy densities. At the present time, there are two CAES plants running, in addition to others being planned or manufactured. The current running plants are called Diabatic CAES due to similarity to the conventional gas turbines, apart from the fact that the expansion and compression stages are decoupled. Subsequently at the compression stage, high pressure gas is stored in a large a storage reservoir at off-peak low-cost electricity.

Energy is discharged by taking the compressed air, heating it and expanding it through a high-pressure turbine. After that, fuel is added to the exhaust, combusted then goes through low-pressure turbine. The very first Diabatic CAES plant was built at Huntorf, Germany in 1978 [72]. The storage was built in salt domes with a volume of 300 000 m^3 and can sustain up to 100 bar pressure. It takes eight hours to charge the plant whilst discharging it takes two hours to generate 290MW. The second CAES system which currently running is the McIntosh plant in Alabama, USA and has a cavern of 500 000 m^3 that operates at 75 bars. The McIntosh plant can generate 110 MW for 26 hours and uses a recuperate to reuse heat from the gas turbine exhaust to recover some heat loses and increase the CAES efficiency. Table 24 illustrate a summary of the current CAES plants [21].

There are two main types of compressed air storage, the first being an underground storage and the second being the aboveground storage. Presently, from the economic and technical point of view, the underground storage reservoirs are more practicable for large-scale systems, whilst the aboveground storage systems being more compatible with smaller scale systems. The research will be focused on the underground storage since the required power is considerably large. Figure 47 shows that the thermal energy storage technologies can use sensible heat storage, latent heat storage, and thermochemical heat storage [27].

Table 24: Summary of the current CAES plants [25]

Location	Huntorf, Bremen, Germany	McIntosh, Alabama, USA
Date commissioned	1978	1991
Storage volume	310,000 m^3	540,000 m^3
Input energy / compressor operation	60 MW	50 MW
Output energy / turbine operation	290 MW upgraded to 321 MW in 2006	110 MW
Energy required for 1 kWh (electricity)	0.8 kWh electricity + 1.6 kWh gas	0.69 kWh electricity + 1.17 kWh gas
Cycle efficiency	42%	54%
Working cavern pressure	43-70 bar	45-76 bar

There are two modes at which the compressed air energy storage power plant switches in between:

1. Charging mode – Solar Energy provides excess energy during periods of time when there is a low amount of energy consumption and is used for air compression and thermal energy storage. The charging mode starts working, if connected to the electrical power station, during the off periods of the day like night-time [73].
2. Discharging mode – The point at which energy is needed and alternative sources are depleted , the air that has been compressed is taken back from the tank and expanded to be able to generate enough power for the user or electric grid [74].

4.4.2 Air storage types. The two kinds of underground air storage are Isobaric and Isochoric air storage. Both natural and artificial underground caverns are used for compressed air energy storage. Figure 48 illustrates the features of these underground caverns [85].

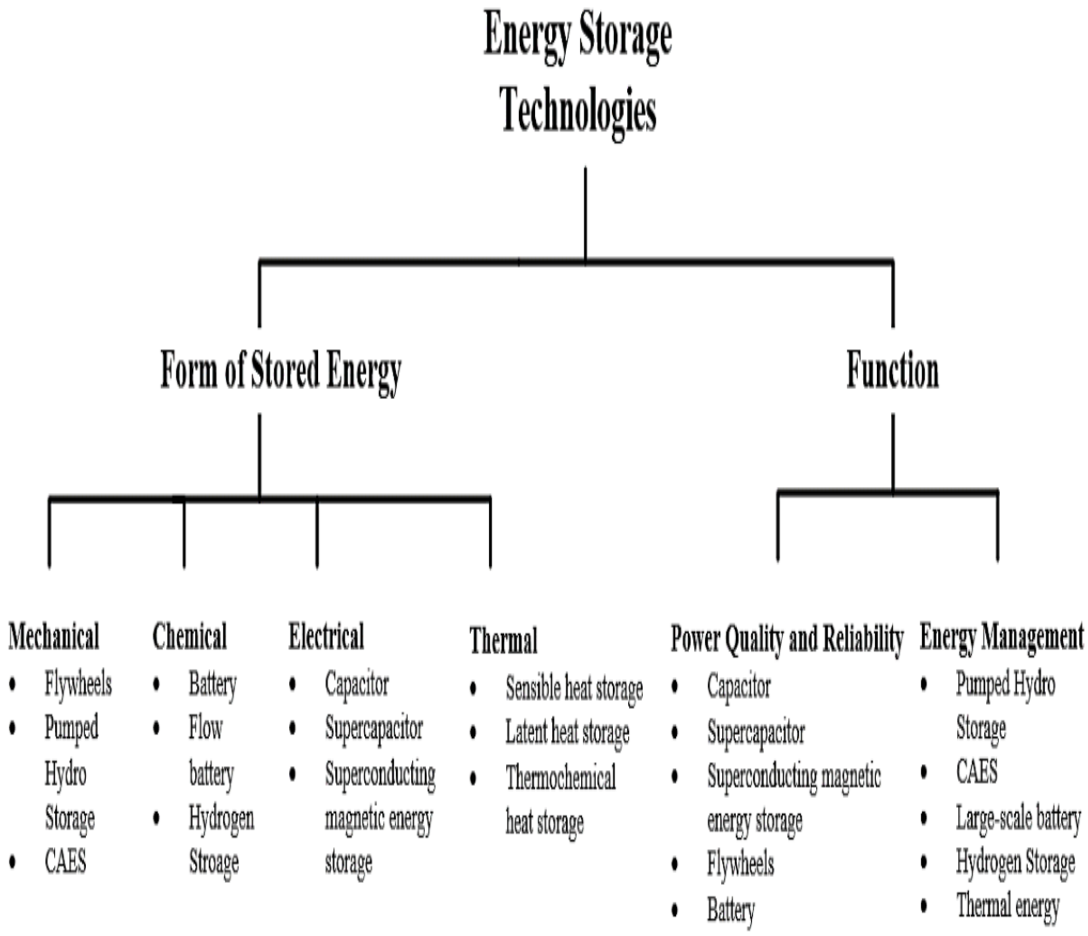

Figure 47: Energy storage Technologies [27]

4.4.2.1. Sliding pressure storage. In a sliding pressure storage, the process of the charge and discharge process will increase and decrease the pressure of the air, respectively, but the volume of the cavern will remain constant.

For the pressure of the discharged air to be discharged constantly, it has to be controlled and guided by a discharge process decided upon by the turbine's optimal performance. With that mechanism called throttling, a constant power supply can be maintained provided by the plant which is autonomous of its state of charge. Underground caverns are created in salt deposits and made vacant through a dissolving process. Water dissolves the salt by a drilling process and is then extracted from the salt deposit creating a cavern. Alabama and Huntorf, Germany are both using the sliding pressure, isochoric underground salt cavern.

4.4.2.2 Constant pressure storage. In Isobaric storage, in which there is a constant pressure, the volume is not constant. This mechanism is not used in Alabama and Huntorf. In order to have Constant pressure storage cavern, we omit the salt deposit and use water to decrease and increase the volume to maintain Isobaric conditions, Therefor the depth of the cavern dictates the storage pressure which remains constant throughout the process [76].

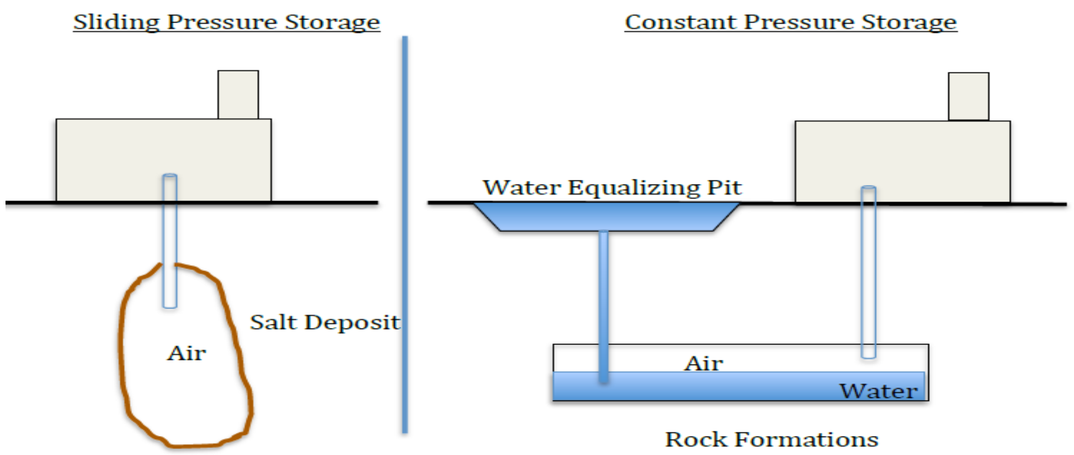

Figure 48: Air Storage Types: Sliding Pressure Storage (left) Constant Pressure Storage (right) [30].

4.4.3 Depleted natural gas caverns. natural gas reservoirs are appealing being as they already exist and hold through the pressure. The issue presenting here will be the fact that ever so often the natural gas is stored for a while at a low pressure. Whilst the CAES requiring a daily to weekly variations of the pressure in thermal energy storage producing a lot of stress in the cavern walls [87].

4.4.4. Salt cavern. Salt Cavern are economically valuable since they are created by a homogeneous deposit of salt through drilling a conventional reservoir to pump fresh water into a salt dome, salt mines are made.

After which the salt is dissolved till the water is saturated, water is extracted to the surface at that moment. The process is done repeatedly until we attain the storage volume. Though it is a lengthy process, it is not burdensome building an underground gas cavern. It is also one of the most economical competitive solutions to build reservoirs at which the compressed air can be stored through. Figure 49 illustrates the geological map of salt formation in UAE [88].

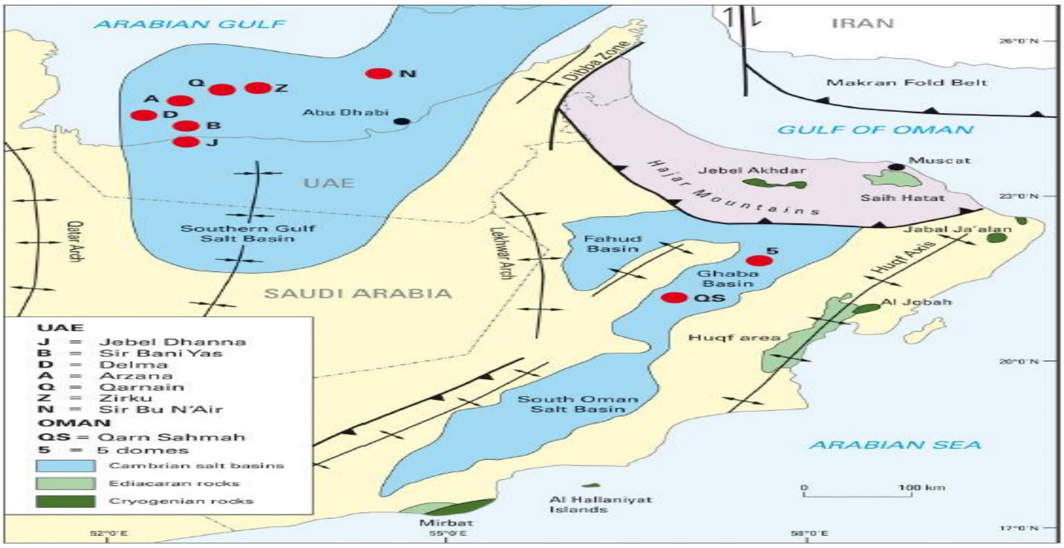

Figure 49:Geological map of salt formation in UAE [82]

4.4.5. Aquifers. Located a couple of hundred meters below ground level and typically full of water, Aquifers are porous and permeable rock formations. Storing compressed air in aquifers has many benefits including the following: geologically widespread availability, relatively large storage capacity and inexpensive construction fees.

The CAES can be classified under three categories based on the system criteria which are isothermal, diabetic, and advanced adiabatic [89].

4.4.6. Isothermal. An isothermal process can be defined as a system that has constant temperature where heat and energy can be exchanged with surrounding. In isothermal CAES, the aim is to decrease any elevation in the temperature during the compression stage.

Essentially, this is attained by increasing the heat transfer rate, as a notable part of energy is converted to heat at the compression stage. Consequently, in order to achieve these states, certain compressor designs are required. Theoretically, high number of compression stages coupled with intercooling heat exchangers are needed to achieve isothermal. Nevertheless, such architecture is unworkable and causes notable pressure losses and costs. Many other methods of attaining near isothermal compression were tested by scientist. One of the more interesting proposals tries to spray water in the compression chamber, allowing huge heat transfer rates, where water droplets have high surface area that enhance the specific heat exchange rate.

4.4.7. Diabatic. Diabatic process can be defined as a system where heat and energy can be exchanged with surrounding. The only two existing compressed air energy storage plants in the world, located in McIntosh, Alabama, and Huntorf, Germany, they are both built on the diabatic method. In diabatic compressed air energy storage, multi-stage compression paired with intercooling heat exchangers which are used to control the notable increase in the heat of the compressor exhaust.

The collected heat at compression stage is wasted and diminished into the environment and needs fuel to operate the gas turbine. This leads to a decrease in CAES roundtrip efficiency and affects the system performance. Figure 50 illustrates Diabetic process of gas turbine with Salt cavern [90].

4.4.8. Advanced adiabatic. An advanced adiabatic process can be defined as a system that has a rapid change on temperature where no heat and energy can be exchanged with surrounding. The main proposition in an adiabatic design is to use the generated heat at the compression stage during the charge process, reuse it later during the discharge process. This process will enhance the roundtrip efficiency of the system. By definition, an adiabatic process will invest the heat which is generated by the compression stage.

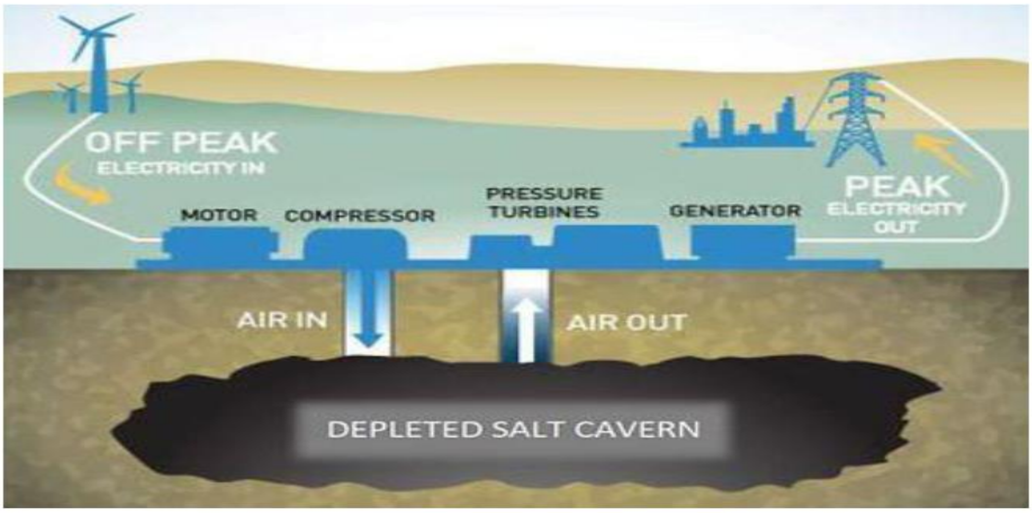

Figure 50:Gas turbine with Salt cavern CAES (Diabatic Process) [92]

An advanced adiabatic design usually needs the utilization of thermal energy storage (TES) system, that stores the generated heat during the compression stage, and reuse the heat to supply the gas turbine with air stream during the expansion process. The TES medium could be a gas or fluid, such as oil or salt, the hot air is circulated as a heat carrier fluid during the expansion process. Figure 51 illustrate the advanced adiabatic process of Gas turbine [91].

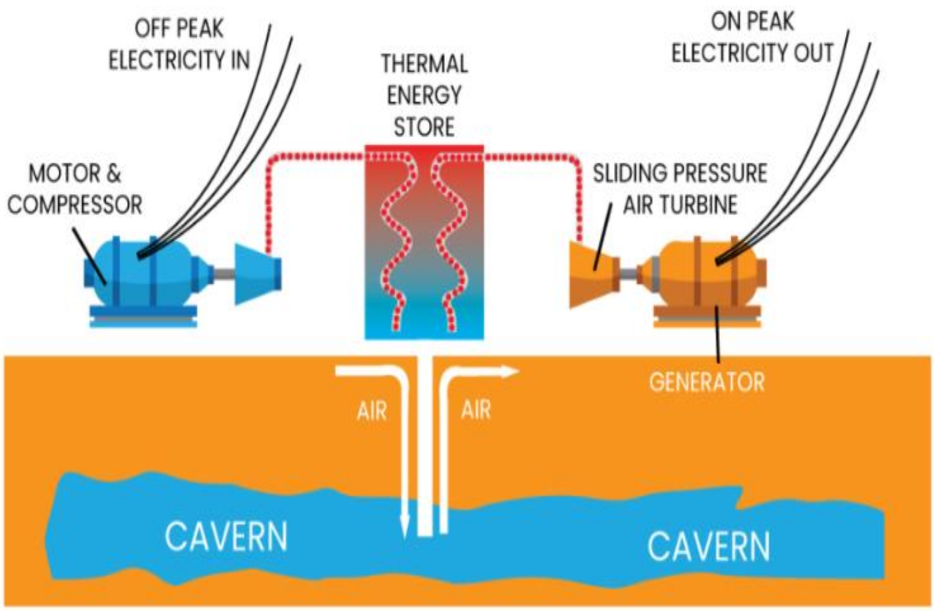

Figure 51: Gas turbine with Salt cavern CAES (Advanced Adiabatic Process) [92]

4.4.9. Material selection. It is important to choose the correct thermal energy storage material medium since it affects the roundtrip efficiency of the CAES .Material selection is based on different criteria as material composition , cost ,availability, thermal conductivity, specific heat capacity, and chemically stable. These criteria are vital to choose the optimum material selection of the thermal energy storage medium. Most of thermal energy storage material medium uses sensible heat storage (SHG) where an increase on the thermal energy storage temperature occurs during the charging process.

The thermal energy storage material medium has direct influence on the amount of heat dissipated to gas turbine at discharging process. Table 25 will illustrate different salt and oil compositions for sensible heat storage medium. It can be noticed that reinforced Concrete is the best option to be applied to this thesis due to many reasons. Firstly, it can sustain higher temperature medium fluid up to 900 C. Secondly, it has lower heat conductivity which means less heat losses will be dissipated with the surroundings. Moreover, its media cost effective when it is compared with other materials, where 1 Kg of reinforced concrete cost around 0.05 USD dollar. Furthermore, CAES is selected to be built in Salt Cavern due to the geological nature of UAE. Air is chosen to be the heat transfer fluid (HTF) at charging and discharging process. The most promising technique for storing a high temperature thermal energy is to use regenerative thermal energy storage (TES) system.

Table 25: Sensible heat storage material data (SHG) [27]

Storage Medium	Sand-rock-mineral oil	Reinforced concrete	Cast iron	Cast steel
Cold Temperature (°C)	200	200	200	200
Hot Temperature (°C)	300	900	400	700
Average density $\left(\frac{kg}{m^3}\right)$	1700	2200	7200	7800
Average heat conductivity $\left(\frac{W}{m*K}\right)$	1	1.5	37	40
Average heat capacity $\left(\frac{KJ}{kg*K}\right)$	1.3	0.85	0.56	0.6
Volume specific heat capacity $\left(\frac{KWh}{m^3}\right)$	60	100	160	450
Media costs per kg $\left(\frac{USD\ \$}{kg}\right)$	0.15	0.05	1	5
Media costs per kWh $\left(\frac{USD\ \$}{kwh}\right)$	4.2	1	32	60

This technology uses packed bed to sustain the high temperature of the pressurized air efficiently. The Regenerative TES acts as a heat exchanger where the heat is transferred by the contact of the solid particles with HTF inside the pipe by a convection heat transfer process. The pipe tube allows the heat exchange between the HTF coming from the PTSC at the charging process and exchanges the heat from the storage material with HTF at the discharging process. An insolation layer is added to the material storage medium as shown in Figure 52 to reduce the thermal losses.

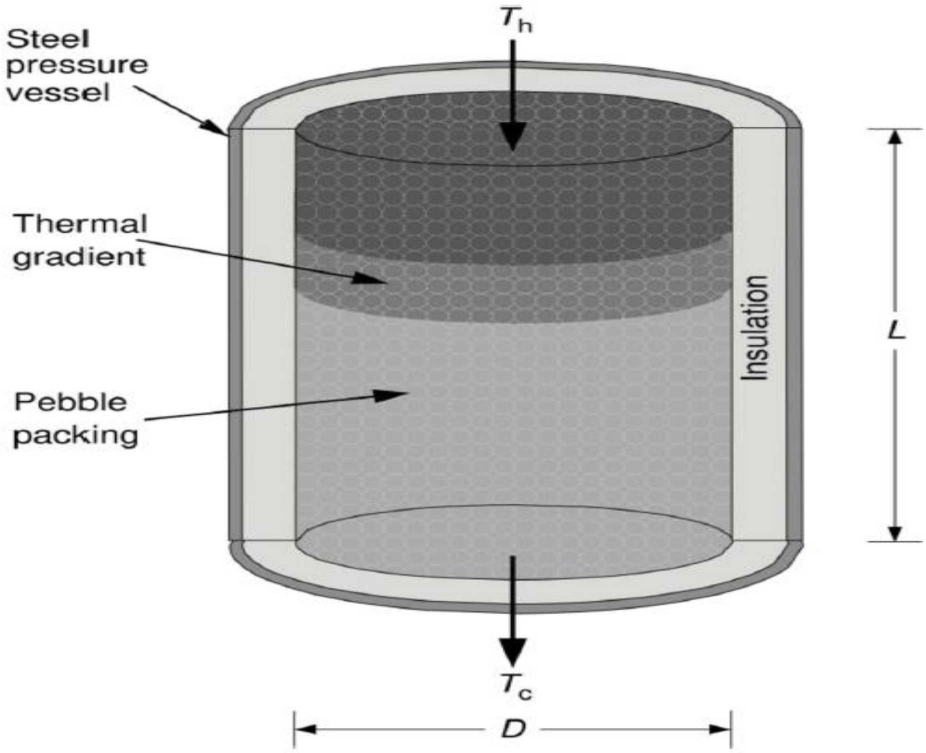

Figure 52: Heat Thermal Energy Storage Medium [30]

4.4.10. **Proposed configurations using CAES technology.** Two new models with CAES technology are proposed. The proposed configurations are simple hybrid gas turbine cycle configuration with advanced adiabatic compressed air energy storage and gas Turbine using low temperature intercooled recuperated air bottoming cycle with advanced adiabatic compressed air energy storage (CAES_ABHGT).

Figure 53 displays the third model which is a simple hybrid gas turbine cycle configuration coupled with a compressed air Energy storage (CAES_HGT). During the high peak of electricity, ambient air is drawn into the topping cycle compressor (1) where it is compressed adiabatically (1-2). After compression, air enters the parabolic trough where it is preheated with the available solar flux at the receiver (2-3). Next, its stored at slat cavern through advanced adiabatic CAES tank (3-3*). During the high peak, the valve of the cavern is opened (4*-4), air goes from the CAES tank through the combustion chamber and heat is added to the air fuel mixture in an isobaric process (4-5). In the next stage, flue gases departing the combustion chamber are expanded adiabatically in the gas turbine for power generation through generators (5-6).

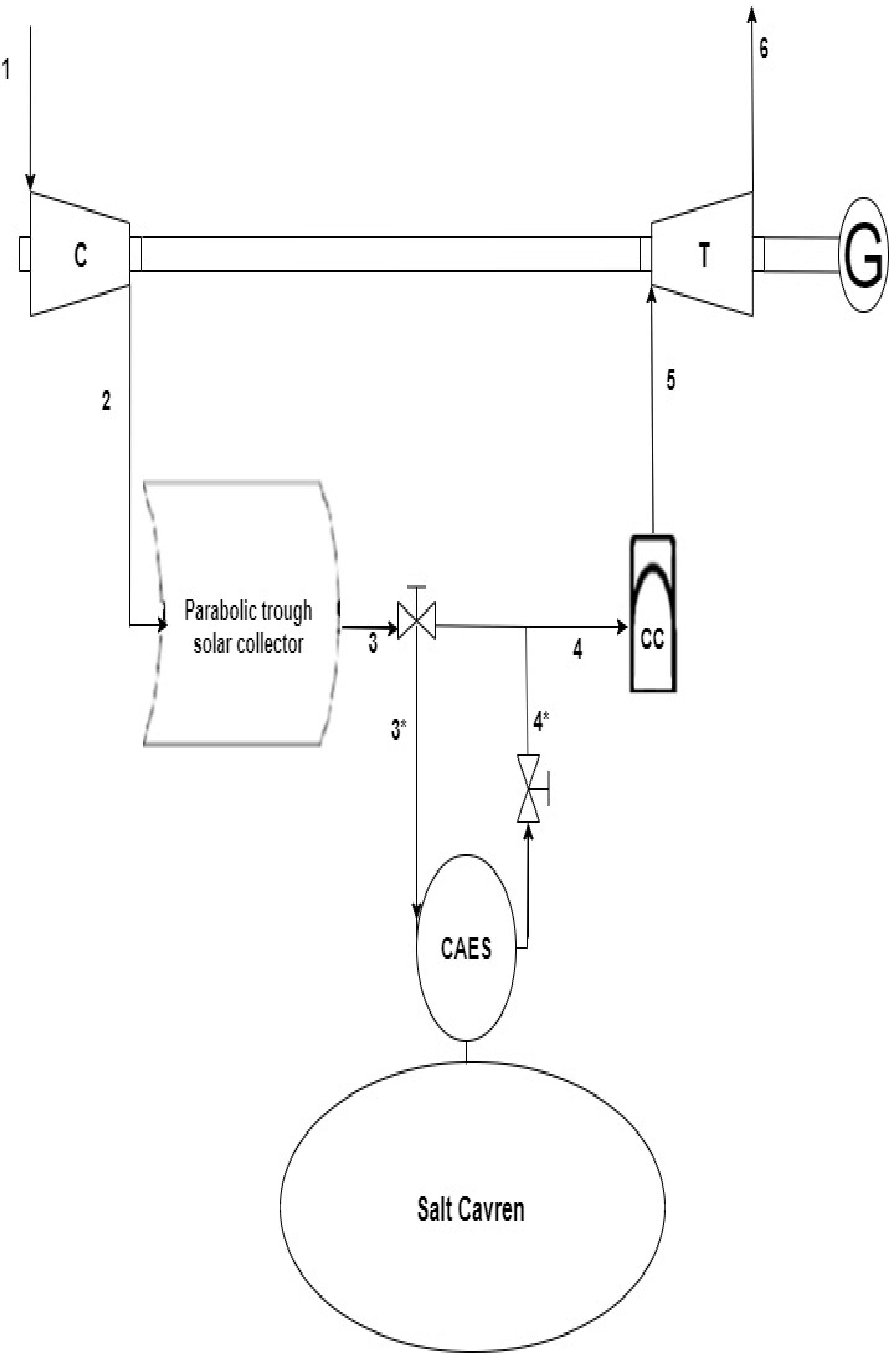

Figure 53: Simple hybrid gas turbine cycle configuration with advanced adiabatic compressed air energy storage (CAES_HGT)

The fourth model concept shown in Figure 54, conceived for hybrid-solar applications, integrates an air-based bottoming cycle with advanced adiabatic compressed air energy storage (CAES_ABHGT). A process flow diagram of this cycle is shown in Figure 54. During the high peak of electricity, In the top cycle, Ambient air is drawn into the topping cycle compressor (1) where it is compressed adiabatically (1-2). After compression, air enters the parabolic trough where it is preheated with the available solar flux at the receiver (2-3). Next its stored at salt cavern through advanced adiabatic CAES tank (3-3*). During the high peak the valve of the cavern is opened (4*-4) air goes from CAES tank through the combustion chamber and heat is added to the air fuel mixture in an isobaric process (4-5). In the next stage, flue gases departing the combustion chamber are expanded adiabatically in the gas turbine for power generation (5-6). Exhaust gases from the topping gas turbine go through the air heat exchanger where a portion of the available waste heat is recovered by the bottoming cycle air flow (6-7). In the bottoming cycle, ambient air is drawn into the bottoming cycle compressor (8) and it is compressed adiabatically (8-9). It is then intercooled through intercooler (9-10) and enters the high-pressure compressor (10-11). Afterwards, it is heated up successively by heat exchanged with exhaust air from the topping and bottoming turbines through waste heat recovery and recuperator respectively (11-12). It is finally expanded in the turbine and cooled down in the recuperator (12-13).

4.4.11. Mathematical model of the CAES and the salt cavern. The mathematical model of CAES and the salt cavern will be illustrated at this sub section. For simplicity, the cyclic loading at the cavern will not be taken in consideration.

4.4.11.1 Regenerative storage. The chief goal of the model of the regenerative storage system is to decide the volume of the tank needed to store a certain amount of heat, alongside that to decide upon the nominal pressure drop produced by the flow inside the CAES.

Two theories have been developed in order to calculate the storage tanks:

- Heat and mass transfer phenomena are purely axial.
- The packed bed is uniform with a persistent void fraction and
shape factor.

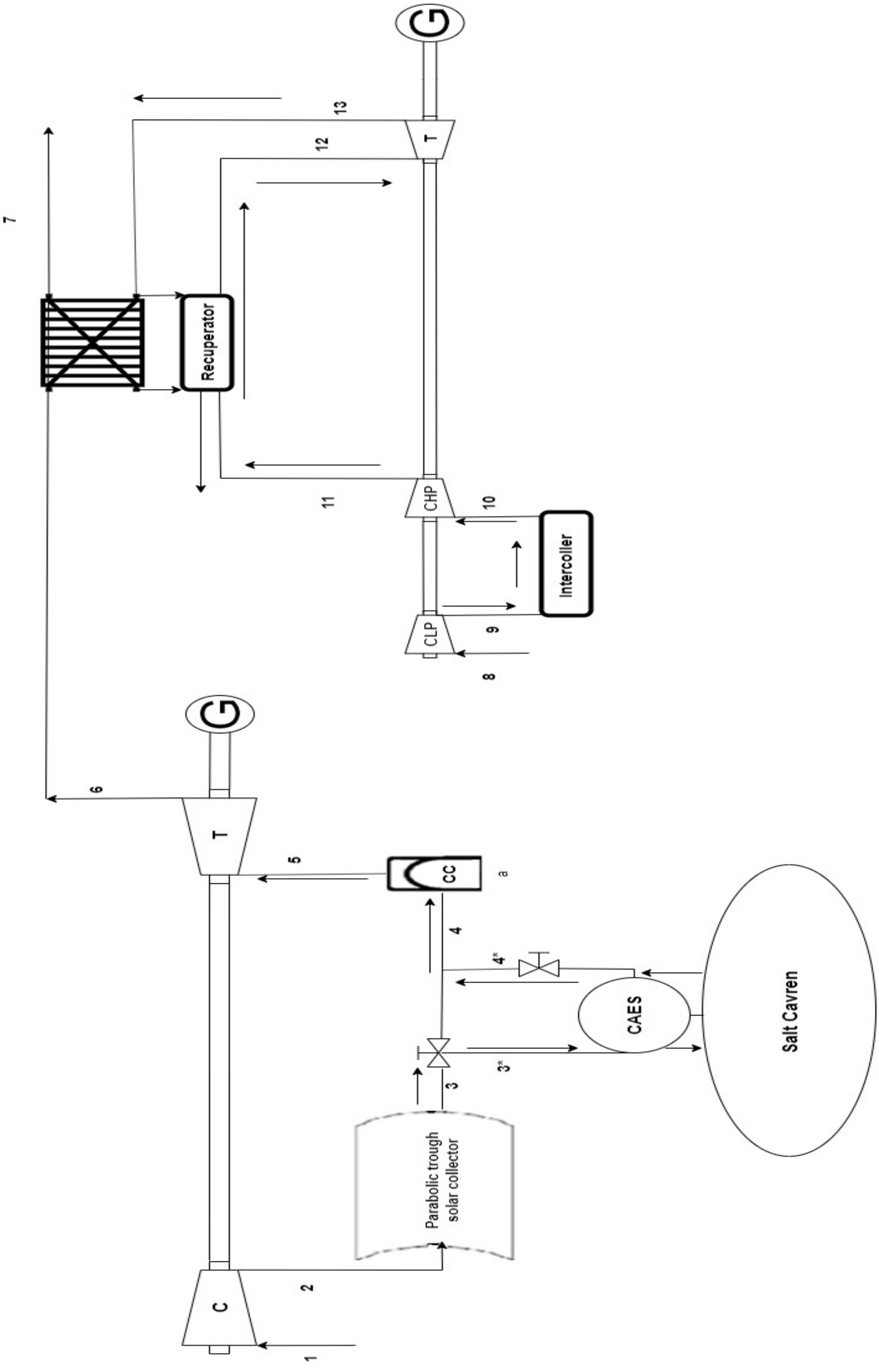

Figure 54: Model of gas Turbine using low temperature intercooled recuperated air bottoming cycle with advanced adiabatic compressed air energy storage (CAES_ABHGT).

The perimeter of the module does not allow air to leave. In addition to that, the regenerative storage unit happens to be a sensible heat storage system, and therefore the quantity of heat able to store in each volume is dependent upon the temperature range at which the operation of this unit takes place, The higher the temperature range, the more the storage density. In the case of a hybrid solar gas-turbine power plant, this temperature range is between the Parabolic trough piping outlet temperature $T4$ and the compressor discharge temperature $T2$. The amount of thermal energy stored in a thermal energy storage cancan be expressed in the equation below [92].

$$Q_{TES} = \rho_s V_{storage} C_s \Delta T \tag{107}$$

where $Q_{storage}$ is the amount of heat stored in [J], ρ_s is the density of the storage material [kg/m^3], $V_{storage}$ is the volume of storage material used (m^3), ΔT is the temperature range of operation [K], and C_s is the specific heat of the medium [J/(kg K)].

The regenerative storage's volumetric nature indicates that the material within the packed bed is not contiguous. The void fraction of the bed ξ is described as the ratio between the void volume and the total volume of the bed and is reckoned to be constant across. If we were to deem the width of the thermocline zone negligible in comparison to the total length of the unit, then we can determine the volume of unit needed to store a given duration of nominal receiver is deduced by the equation (108) where $t_{storage}$ is desired storage duration ρ_s and c_s the density and specific heat capacity of the s medium, and Q_{rec} the nominal receiver output [92].

$$V_{TES} = \frac{\dot{Q}_{rec}^{nom} * t_{storage}}{(1 - \xi)\rho_s C_s (T_4 - T_2)} \tag{108}$$

The storage unit's capacity to sustain the thermocline zone depends on the effective thermal conductivity k_{eff} of the packed bed, that can be calculated by the conductivity of material k_s using Equation (109) [2].

$$k_{eff} = k_s * \frac{(1 - \xi)}{(1 + \xi)} \tag{109}$$

The pressure lost at cavern can be expressed by equation (110) , where the pressure losses occurs by flow of air inside the unit and can be calculated using the McCorquodale correlation [22], given in Equation and adjusted to consider the shape factor fs of the storage particles, which are not necessarily spherical. l is the length of the storage unit module; the mass flux G is the ratio between the mass flow and the flow area and ds is the characteristic diameter of the storage media. The heat transfer fluid is characterized by its dynamic viscosity μ_b and density ρ_b, evaluated at a mean bulk temperature [2].

$$\Delta P_{stor} = \frac{f_s G^2 l(1-\xi\ )}{\rho_b d_s \xi^{\frac{3}{2}}}\left[4.74 + 166\frac{(1-\xi\ )f_s\mu_b}{\xi^{\frac{3}{2}} G d_s}\right] \quad (110)$$

Through the walls of the CAES, heat losses from the storage unit will occurs. The final heat loss coefficient U_{loss} can be calculated using Equation(111), where α_{NC} is the natural convection heat transfer coefficient at the external surface of the insulation, which Morel [71] gives as 5 W/m^{2}K, *and* t_{ins} and k_{ins} are the thickness and thermal conductivity of thermal in isolation [2].

$$\frac{1}{U_{loss}} = \frac{t_{ins}}{k_{ins}} + \frac{1}{\alpha_{NC}} \quad (111)$$

4.4.11.2 Adiabatic cavern storage. The adiabatic cavern mathematical model is illustrated below [92]:

Charge: ($\dot{m}_{out} = 0$)

$$M(t) = \dot{t} + \grave{M} \quad (112)$$

$$T(t) = \frac{\dot{m}kT_4 t}{M(t)} + \grave{T}\frac{\grave{M}}{M(t)} \quad (113)$$

$$p(t) = \frac{m\dot{K}T_4 t}{M(t)} + \grave{p} \quad (114)$$

Discharge: ($\dot{m}_{in} = 0$)

$$M(t) = M_{max} - \dot{m}t \quad (115)$$

$$T(t) = T_{max}(1 - \frac{\dot{m}t}{M_{max}})^{(K+1)} \quad (116)$$

$$P(t)V_{cavern} = M(t)RT(t) \quad (117)$$

where $\grave{p}$ is the cavern initial pressure, M' is the initial mass flow rate of the cavern and T_4 is the inlet temperature of the cavern, T_{max} and M_{max} can be obtained by substituting the charging time (t) at the above equations, $\grave{T}$ are the initial mass and temperature of air at the charging phase. It can be assumed that $\grave{T} = T_4$ since it is an adiabatic process [90].

The round-trip storage efficiency of the CAES is given by the following equation:

$$\eta_{HGT-CAE} = \frac{\dot{W}_t}{\dot{W}_c + \dot{Q}_{TES}} \tag{118}$$

where $\dot{Q}_{TES}$ is the useful Thermal energy storage.

4.4.12. Economical model of the CAES and the salt cavern. The cost of generative TES can be divided to three separate parts which are the cost of storage vessel (Z_{ves}), the cost of storage material ($Z_{TES,material}$) and the cost of storage insulation ($Z_{TES,ins}$). The total cost of generative TES (Z_{TES}) can be calculated using the equation 119.

$$Z_{TES} = Z_{ves} + Z_{TES,material} + Z_{TES,ins} \tag{119}$$

The cost of storage of storage vessel can be expressed as a function of its length and diameter using Turton equation 120 [65]:

$$\begin{aligned} log_{10}Z_{ves} &= K_1 + K_2 . log_{10}l_{TES,Ves} + K_3(log_{10}l_{TES,Ves})^2 \\ &+ log_{10}\left(B_{1+}B_2F_MF_p\right) \end{aligned} \tag{120}$$

where value of K_1 , K_2 and K_3 can be selected from Table 26 based on the Vessel Diameter. Turton states on his literature that B_1 equals to 1.620 and B_2 equal to 1.471. F_M, F_p are the material and pressure correlation factors, respectively. The material and pressure correlation factors can be expressed by the below equations (121 ,122) based on the working Pressure ($P_{4)}$ and temperature (T_4) at the Storage [2].

$$F_M = \left(\frac{T_4}{623}\right)^2 \tag{121}$$

$$\begin{aligned} F_p &= 0.515 + 0.684log_{10}P_4 + 0.297(log_{10}P_4)^2 + 0.024(log_{10}P_4)^4 \\ &+ 0.002(log_{10}P_4)^8 \end{aligned} \tag{122}$$

Table 26: Storage Vessel Cost Correlation [2]

Vessel Diameter (m)	K_1	K_2	K_3	$l_{TES,max}$(m)
0.3	2.90	0.578	0.126	20
0.5	3.103	0.578	0.063	25
1	3.359	0.591	0.111	30
2	3.760	0.368	0.95	40
3	3.772	0.716	0.043	50
4	4.155	0.224	0.250	52
5	4.355	0.214	0.350	55
6	4.650	0.115	0.450	56
7	4.772	0.110	0.478	58
8	5.213	0.100	0.532	60

The cost of TES material and thermal insulation can be calculated through the below equations [2]:

$$Z_{TES,material} = c_{TES,material}.\, \rho_s \xi .\, \pi \, \frac{d^2{}_{TES,Ves}}{4} \;\; l_{TES,Ves} \tag{123}$$

$$Z_{TES,ins} = c_{TES,ins}.\, \pi \frac{t^2{}_{TES,ins} + (2d_{TES,Ves}.\, t_{ins})}{4} \;\; l_{TES,Ves} \tag{124}$$

where $c_{TES,ins}$ is the specific insulation cost in ($\frac{\mathrm{USD}}{m^3}$), $c_{TES,material}$ is the specific material cost in ($\frac{\mathrm{USD}}{\mathrm{kg}}$) ,$\xi$ is void fraction of the storage, ρ_s is the density of the material storage , t_{ins} is the insulation thickness in (m) and $d_{TES,Ves}$ is the diameter of the vessel in (m). Wool thermal insulation is selected as the material of Vessel insulation. $c_{TES,ins}$ for Wool thermal insulation equals to 300 ($\frac{USD}{m^3}$) Concrete is selected as the material storage, $c_{TES,material}$ for concrete equals to 0.05 ($\frac{USD}{kg}$) .The cost of salt cavern can be illustrated by the equation 125 [92]:

$$Z_{cavern} = 3.75 * 10^7 + 62 * V_{cavren} \tag{125}$$

where Z_{cavern} is the cost of salt cavern in (US \$) , V_{cavren} is the cavern volume in (m^3).

4.4.13. Decision variables. The topping cycle parameters will be validated by Siemens GT-800 so the data will be collected from the steady state analysis. However, the bottoming cycle paraments need to be optimized to obtain the optimal value. The heat exchanger minimum approach temperature needs to be optimized to acquire the optimal capital-energy trade off. The heat exchanger components in this model are heat waste, recuperator and intercooler. Additional CAES models were taken in consideration in the optimization problem to determine the optimal cavern and TES Volume with the addition of optimal TES capacity. Table 27 illustrates the decision variables selected for the optimization problem with their corresponding validation ranges.

Table 27: Decision variables selected for the 2nd optimization problem.

Decision Variables	**Range**
Number of PTSCs (N_{PTSC}) (unit)	[100-1000]
Aperture area of PTSC A_{PTSC} (m^2)	[100-150]×10^3
Bottoming Compressor ratio	[1.5-3]
Heat waste Minimum approach Temperature (C°)	[5-40]
Recuperator Minimum approach Temperature (C°)	[5-40]
Intercooler Minimum approach Temperature (C°)	[5-40]
Cavern Volume (m^3)	[50-500] ×10^3
TES Volume (m^3)	[200-10000]
TES Capacity (hrs)	[1-24]

4.4.14. Optimization results. This section will illustrate the optimization results of the two CAES models which are the Simple hybrid gas turbine cycle configuration with advanced adiabatic compressed air energy storage (CAES_HGT) and the model of gas Turbine using low temperature intercooled recuperated air bottoming cycle with advanced compressed air energy storage (CAES_ABHGT).

The optimization convergence algorithm results are illustrated on Figure 55. The multi objective algorithm method that is used in this project, is the Pareto optimal front method. The advantages of using this method as it gives clear sign of the tradeoff curve between the objective functions in the objective space. Using Pareto optimal front method on Simple and combined hybrid gas turbine power plants with advanced adiabatic compressed air energy storage (CAES_HGT,CAES_ABHGT) would illustrate a clear indication of the tradeoff curve between the total capital cost and the cost of CO_2 emissions.

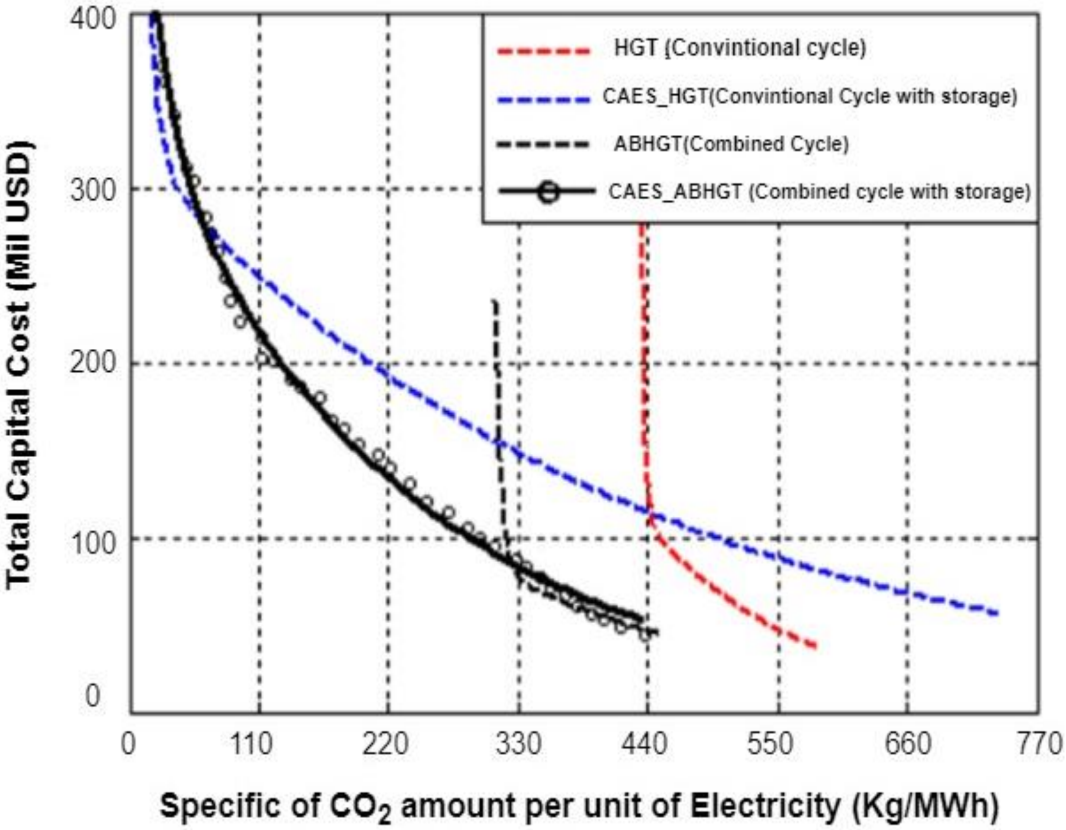

Figure 55: Objective functions trade off of CAES_HGT and CAES_ABHGT

It can be noticed that the total capital cost is increasing linearly as the CO_2 emissions decreases till a certain point. This point is called the lower theoretical limit where decreasing the CO_2 emissions below this limit leads to an exponential increase in the total capital cost. The CO_2 emissions lower theoretical limits of HGT and ABHGT is 420 $kgCO_2/MWh$ and 325 $kgCO_2/MWh$ respectively. Moreover, it can be noticed that ABHGT specific CO_2 emissions are lower than HGT emissions for a given total capital cost. The additional of advanced adiabatic compressed air energy storage reduced the CO_2 emissions lower theoretical limits of CAES_HGT and CAES_ABHGT to 50 $kgCO_2/MWh$.

One of the most popular economic indicators for power plants performance is the levelized cost of electricity (LCOE). LCOE is used to measure the cost of electricity produced. It can be also defined as the cost of electricity sale which makes the net present value (NPV) of the investment equal to zero. The investment of the project would be more profitable if the LCOE is minimized. Figure 56 shows the effect of solar share on LCOE.

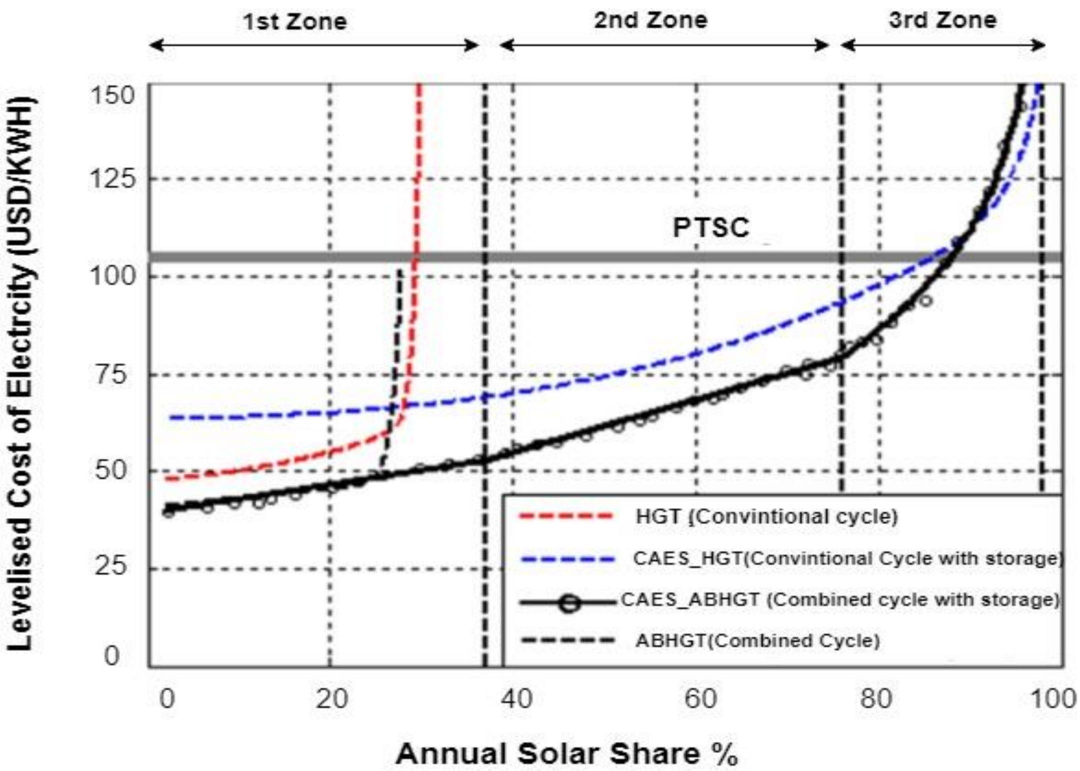

Figure 56: Levelized electricity costs of the Pareto-optimal gas-turbine designs

It can be noticed from Figure 56 that the LCOE is slightly decreasing as the solar share increases up until a certain limit where an increase in solar share leads to an exponential increase in LCOE. This is due to the fact that adding solar components to a certain solar share limit is more profitable than running the power plant purely with fuel gases. Moreover, it can be seen that the LOCE of ABHGT power plant is about 58 (USD /MWh) with a corresponding annual solar share of 22% while LCOE of HGT powerplant is about 65 (USD /MWh) with a solar share of 20%. It can be noticed at the 1st zone that that the values of LCOE of HGT and ABHGT increase steadily until the optimal annual solar share reached whereas adding the advanced adiabatic Compressed air energy storage to the two models leads to an increase in the solar share with reasonable LCOE. At 20% annual share it can be seen that the LCOE of ABHGT and CAES_ABHGT almost identical to each other. Furthermore, it can be observed at the 2nd zone that that the LCOE of CAES_ABHGT is lower than CAES_HGT at any annual solar share. Moreover, it can be seen at the 3rd zone that the LOCE of CAES_ABHGT power plant is about 94.5 (USD /MWh) with a corresponding optimal annual solar share of 87% while LCOE of CAES_HGT power plant is about 105.9 (USD /MWh) with an optimal solar share of 85%. An increase in the annual solar share can be achieved through increasing the area of the solar components which is not convenient to do after reaching the optimal value since the LCOE will increase exponentially. At higher annual share above 90 % the Simple hybrid gas turbine cycle configuration with advanced adiabatic compressed air energy storage (CAES_HGT) can achieve lower LCOE than the combined cycle with storage (CAES_ABHGT) .The reason behind is that adding more solar component at high solar share can no more justify the efficiency improvement by adding the bottoming cycle to the power plant. Nevertheless, the performance of both power plants above 90 % solar share is lower than Pure conventional PTSC power plant.

The solar electricity cost is another important economic indicator for power plants performance which can be seen in Figure 57. It can be noticed from Figure 57 that the values of Solar electricity of HGT and ABHGT increase steadily until the optimal annual solar share reached whereas adding the advanced adiabatic Compressed air energy storage to the two models leads to an increase in the solar share with reasonable solar electricity cost. It can be observed at lower annual share (below 22%) that the hybrid combined power plant without the advanced adiabatic compressed air energy storage (ABHGT) has lower solar electricity cost than CAES_ABHGT. Nevertheless, at medium and higher annual solar shares adding the advanced adiabatic compressed air energy storage will be beneficial since the higher annual solar share will compensate for the increase solar electrical cost. Also, it can be noticed that the performance of both power plants above 90 % solar share is lower than Pure conventional PTSC power plant.

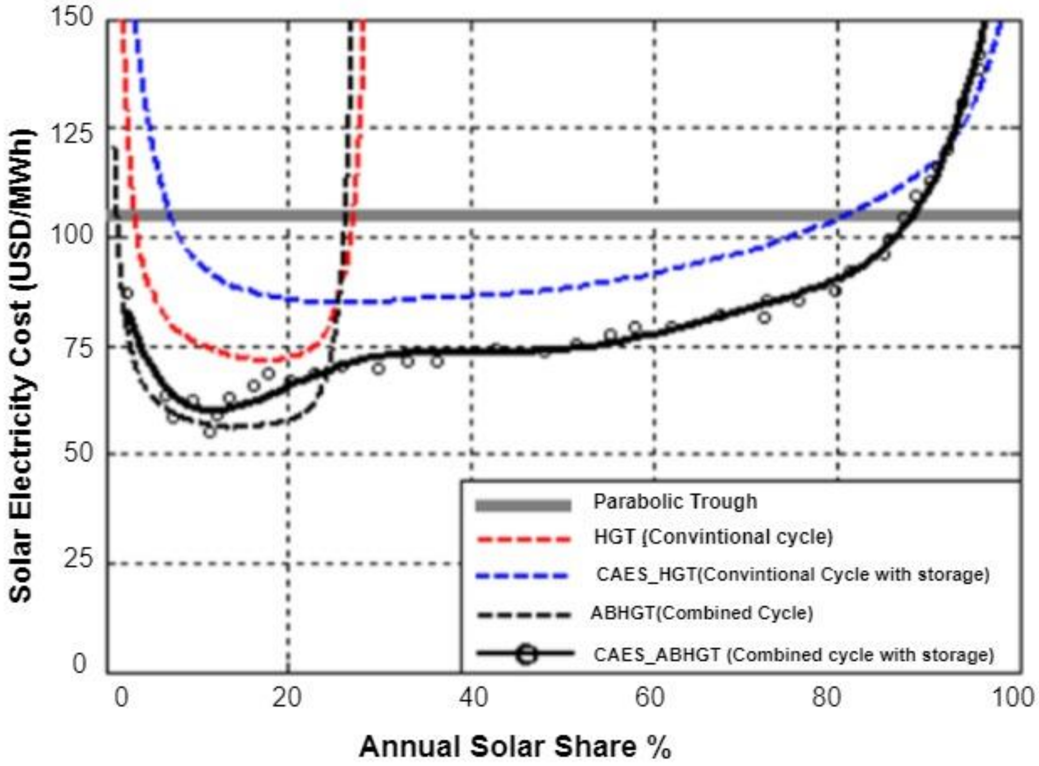

Figure 57: Solar Electricity cost versus the annual solar share

Reducing the CO_2 emissions is one of the main objectives in the current thesis. Reducing the CO_2 emissions means less reliance on fossil fuel that has a large impact on the climate change. The specific of CO_2 amount per unit of electricity emitted by the plant (f_{CO_2}) is one of the key factors to the environmental indicators. The relation between Specific CO_2 emissions (f_{CO_2}) and the annal solar share is shown in Figure 58. It can be noticed that both plants' specific CO_2 emissions (f_{CO_2}) decrease with increasing the annual solar share until a certain limit where decreasing (f_{CO_2}) then leads to an exponential increase in LCOE. This theoretical limit illustrates that it is not worth it to invest more in annual share in order to reduce more specific CO_2 emissions. The annul solar share limits for CAES_ABHGT and CAES_ HGT are 85% and 87% respectively. The (f_{CO_2}) of CAES_ABHGT at 22% annual solar share is 330 (kg CO_2/MWh) while at the (f_{CO_2}) of CAES_ABHGT at 87% annual solar share is 60 (kg CO_2/MWh). It can be observed by adding the advanced adiabatic compressed air energy storage that the specific of CO_2 amount per unit of electricity emitted by the plant $(f_{CO_2})$is enormously reduced by 82 % for both power plants.

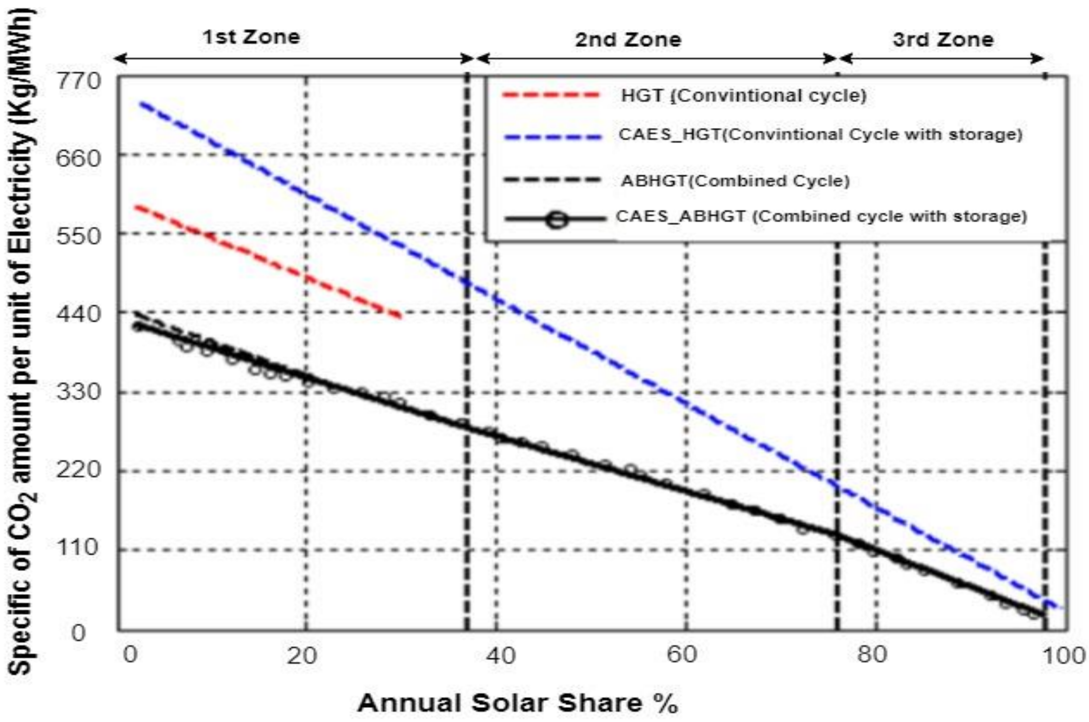

Figure 58: Specific CO_2 emissions (f_{CO_2}) versus the annal solar share

The optimization results of the four models' models (HGT, ABHGT, CAES-HGT, CAES-ABHGT) illustrate a diversity on different optimal configurations and designs. HGT model can be neglected in the comparison since it is not competitive when compared to the other three models where increasing the solar share leads to an increase in the LCOE exponentially .Different performance indicators were taken into consideration to evaluate the optimization problem. One might argue that minimizing the LCOE and maximizing the NPV of the power plants leads to an optimal design parameter. Another person can argue from another perspective that minimizing the specific CO_2 emissions or maximizing the annual overall efficiencies leads to an optimal design parameter. To overcome this issue, a unified performance indicator is introduced in Figure 59 to select an optimal design accordingly. Degree of penalty cost due to avoidance of CO_2 emissions is selected as a unified performance indicator to select an optimized configuration with optimal design variables. This performance indicator is significantly selected since it accounts for both economic and environmental performance indicators. Figure 59 illustrates the degree of penalty cost due to CO_2 emissions avoidance versus annual solar share for the three configurations.

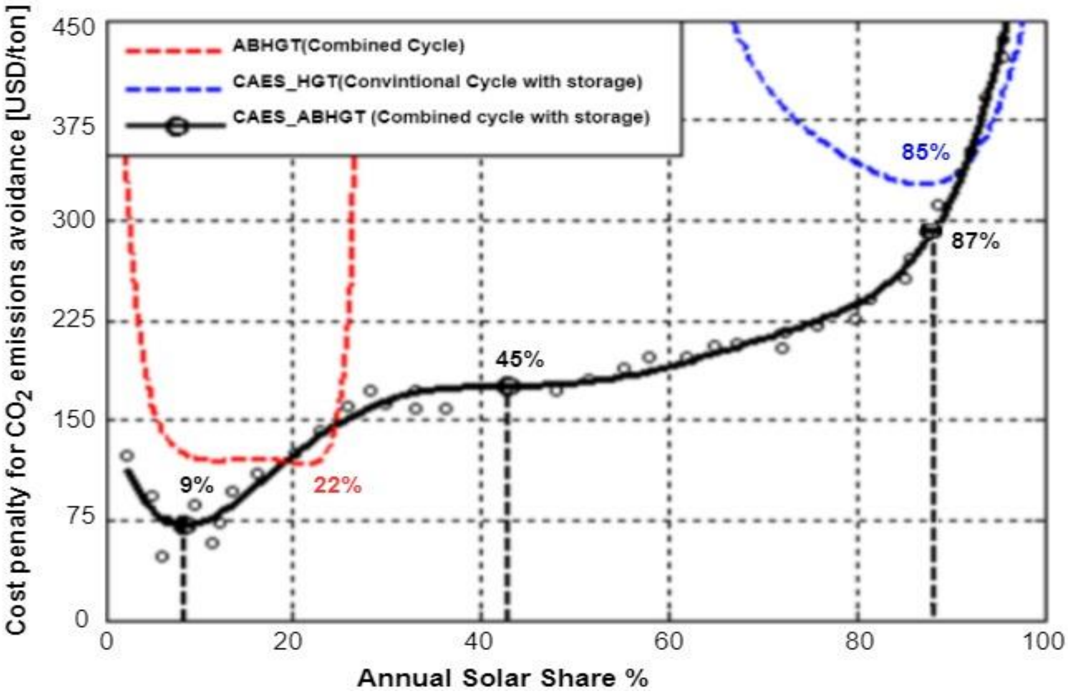

Figure*59*: CO2 emissions penalty cost versus annual solar share

It can be noticed that the minimum degree of penalty cost due to CO_2 emissions avoidance (Z_{Co_2}) of ABHGT power plant is 90 (USD/ton) at 22% annual solar share whereas the minimum degree of penalty cost due to CO_2 emissions avoidance (Z_{Co_2}) of CAES-ABHGT is 75 (USD/ton) at 9% annual solar share. It can be seen that the minimum degree of penalty cost due to CO_2 emissions avoidance (Z_{Co_2}) of CAES-HGT is 350 USD/ton at 85% annual solar which considered to be not competitive at all. Accordingly, the optimal design variables were selected based on minimizing the degree of penalty cost due to CO_2 emissions avoidance (Z_{Co_2}) with its corresponding annual solar share. Furthermore, it can be noticed that the optimal annual solar share for Conventional power plant has a limit at 22% where increasing more than that leads to an exponential increase on penalty cost due to CO_2 emissions avoidance. Accordingly, adding the CAES technology improves the optimal annual solar share up to 87%. Thus, choosing the optimal size of cavern and CAES will be based on the unified performance indicator with its corresponding annual solar share.

The optimal Storage capacity for different annual solar shares is illustrated at Figure 60. It can be noticed that storage capacity is small at lower shares and increases as the annual solar share increases.

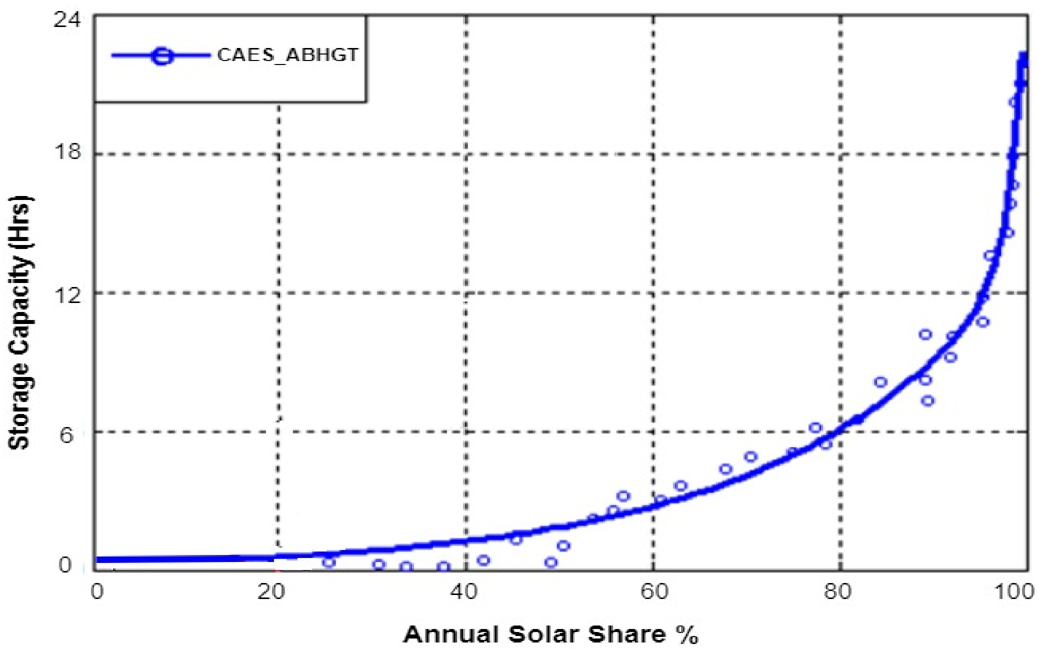

Figure 60: The optimal Storage capacity for different annual solar shares

Three optimized modes based on the unified performance indicator with different CAES capacities were compared on Table 28. The optimum LCOE and Solar equipment cost were computed. The Performance of gas Turbine using low temperature intercooled recuperated air bottoming cycle with advanced compressed air energy storage (CAES_ABHGT) is illustrated at 1, 3 and 7.5 hours of storage capacity. Thus, it can be seen that Mode C at 7.5 hours storage capacity is the most promising model since it has the highest annual solar share of 87% with reasonable LCOE of 94.5 (USD/MWh). Moreover, Mode C is the most clean and sustainable model since the specific carbon emission (kg CO_2/MWh) at mode C is reduced by 85%.

Table 28: Different operating modes of CAES_ABHGT

Design parameters	Mode A	Mode B	Mode C
CAES capacity (Hrs.)	1	3	7.5
Annual solar Share (%)	9	45	87
Total Capital Cost (Mil USD)	110	134	272.4
Solar equipment cost (Mil USD)	12	70	130
LCOE (USD/MWh)	40.5	58.4	94.5
Plant Capacity (%)	52.1	60.4	75
Specific carbon emission (kg CO_2/MWh)	380.3	250.5	60
CAES Volume (m^3)	278	834	2780
Plant annual operating hours (Hrs.)	4564	5291	6570
Annual power Output [GWh/year]	255.6	296.3	367.9

The optimal parameters and Performance of CAES_ABHGT power plant at mode C are listed in Table 29. The Annual Electricity output of CAES_ABHGT power plants is 367 (GWh/year).

It can be noticed the overall annual energy efficiency is almost identical to the overall annual exergy efficiency since the difference between both efficiencies decreases as the solar share increases. The annual overall energy and exergy efficiencies of ABHGT are 33.6% and 33.2.

Table 29: Optimal parameters and design performance of CAES_ABHGT at Mode C

Design performance	**CAES_ABHGT (Mode C at 7.5 Hrs. Storage)**
Optimal Power Output [MW]	56
Annual power Output [GWh/year]	367.9
Capacity Factor %	75
Number of PTSC (NPTSC) [units]	792
Annual optimal Solar Share %	87
Topping Cycle Mass flow rate (kg/s)	268
Power plant annual operating hours in [hr]	6570
Top Cycle Compressor pressure ratio	10.5:1
Bottom Cycle Compressor pressure ratio	2.5:1
CAES Roundtrip efficiency %	75
TIT Firing Temperature in [K]	1300
Specific CO_2 Emissions [kg CO_2/MWh]	60
Cost penalty for CO_2 Avoidance [USD/tonCO_2]	280
Total Capital Cost [Mil USD]	272.4
Levelized Cost of Electricity [USD/MW]	94.5
Cavern Volume (m^3)	300000
CAES Volume (m^3)	2780
Maximum Cavern pressure (MPa)	4
Annual Overall Energy Efficiency %	33.6
Annual Overall Exergy Efficiency %	33.2

The LCOE of CAES_ABHGT is 94.5 (USD/MW) and at annual solar share of 87%. The Specific CO_2 emissions of CAES_ ABHGT is 60 [kg CO_2/MWh] at 87% annual solar shares. Reducing the CO_2 emissions is one of the main objectives in the current thesis. The specific of CO_2 amount per unit of electricity emitted by the plant

(f_{CO_2}) is one of the key factors to the environmental indicators. Thus, reducing the CO_2 emission means less reliance on fossil fuel that has large impact on the climate change.

4.4.15 Total Capital Cost Breakdown of Power Plants with storage. The Total capital cost breakdown of CAES_ABHGT and CAES_HGT power plants is shown in Table 30. Figures 61 and 62 illustrate the total capital cost break down in pie charts. It can be noticed that both power plants have almost 70% contribution of total equipment cost whereas the rest of contributions go to land, contingencies, civil engineering, and pipeline branching costs.

Table 30: Total Capital cost Breakdown of CAES_ABHG and CAES_HGT

Capital cost break down [Mil US$]	**CAES_ABHGT**	**CAES_HGT**
PTSC total price	4.2	4
Top Gas Turbine	30	30
Bottom Gas Turbine	8	0
Top Compressor	13.8	13.8
Bottom Compressors (LP and HP)	0.6	0
Generators	6	5
Electronics	10	9
Heat waste recovery	15	0
Intercooler with Fan	3	0
Recuperator	4	0
Civil Engineers and Pipe Branching	25	23
Land	14	13
Contingencies	13	11
CAES	70	70
Salt cavern	56	56
Total Capital Cost [Mil US$]	**272.6**	**234.8**

Moreover, it can be seen that the PTSCs contribution with CAES have almost 50% contribution of total equipment cost. This is due to the fact that an adiabatic CAES technology was used. Despite the slight increase on PTSC cost of ABHGT, the solar cost contribution to total capital cost is still lower than HGT by 1%. The most expensive components in both configurations are the CAES and Salt cavern. The Gas Turbine cost contribution to the total capital cost is about 13% for HGT and 11% for ABGHT. Furthermore, it can be seen that the ABHGT heat waste recovery, intercooler and recuperator costs contribution to the total capital cost are about 11%.

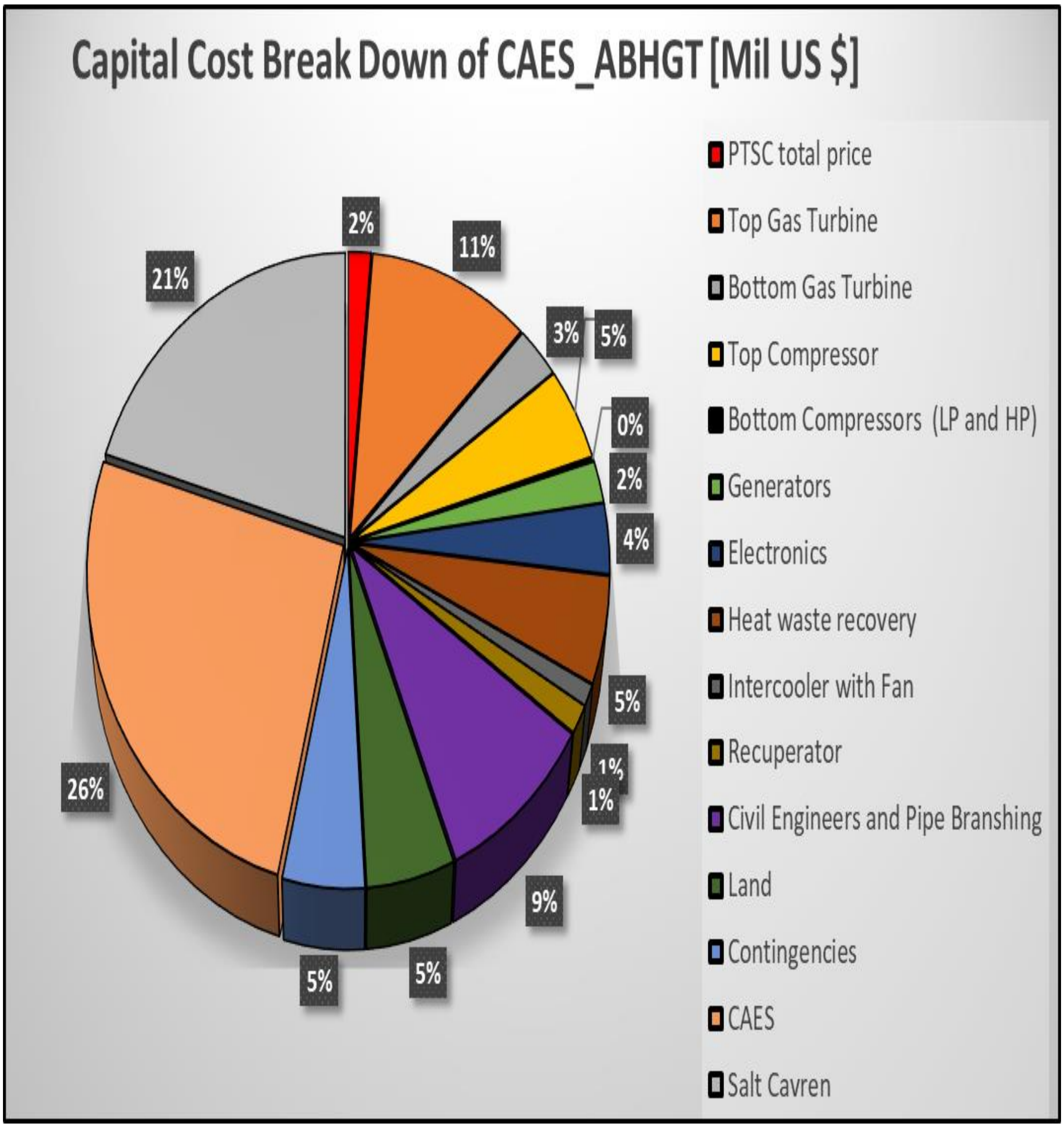

Figure 61: Capital Cost Breakdown of CAES_ABHGT

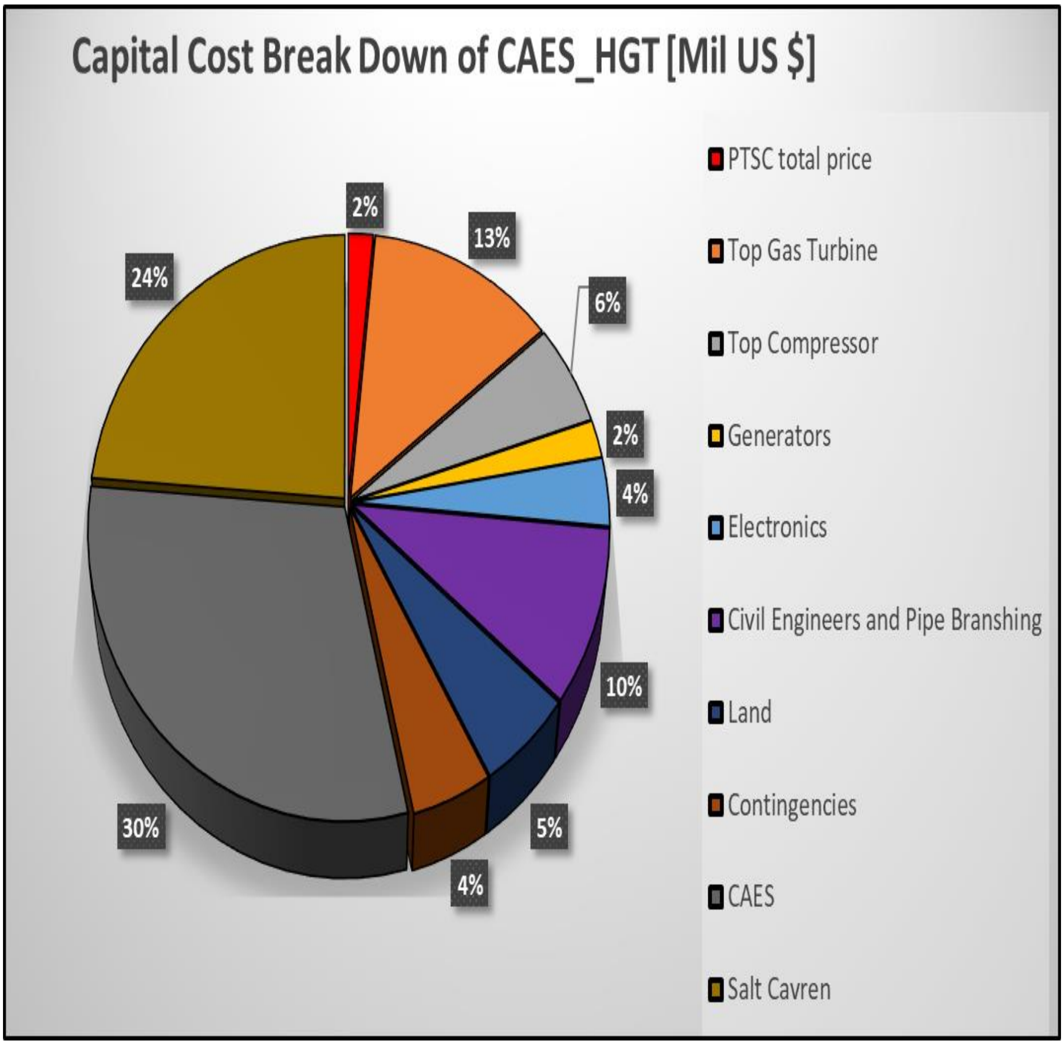

Figure 62: Capital Cost Breakdown of CAES_HGT

4.4.16. LCOE breakdown of power plants with storage. The levelized cost of electricity (LCOE) breakdown of CAES_ABHGT and CAES_HGT power plants are shown on Table 31. It can be noticed in both power plants that the annualized capital cost is the main share contributors to the LCOE. Moreover, the annualized fuel cost is not a major contributor anymore since the power plants depend more on annual solar Share. The annualized capital cost and fuel cost of CAES_ABHGT are 70.9 (USD/MWh) and 4 (USD/MWh) whereas the annualized capital cost and fuel cost of CAES_HGT are 79.8 (USD/MWh) and 7.15 (USD/MWh) respectively. Moreover, the additional annualized capital cost of bottoming cycle of ABHGT is remunerated by the annualized fuel cost reduction at the topping cycle.

Table 31: Levelized Cost Breakdown of Power Plants with storage

Levelized cost break down	**CAES_ABHGT**	**CAES_HGT**
Total capital cost [Mil US $]	272.4	234.8
Annualized Capital Cost [USD/MWh]	**70.9**	**79.8**
Annual Water cost [Mil US $]	0.04	0.033
Annualized water cost [USD/MWh]	**0.108**	**0.108**
Annual Fuel (NG) cost [Mil US $]	1.5	2.21
Annualized fuel cost [USD/MWh]	**4**	**7.15**
Annual Operation and Maintenance [Mil US $]	6	4.59
Annualized Operation and Maintenance [USD/MWh]	**16**	**14.8**
Total Decommissioning [Mil US $]	13.6	11.7
Annualized Decommissioning [USD/MWh]	**3.545**	**3.5**
Total LCOE [USD/MWh]	**94.5**	**105.4**

4.4.17. Comparative analysis with literature. Comparative analysis with literature is done to provide a general comparison between the simulated models and literature results.

Shams 1 is selected as a reference power plant for the comparative analysis since it is running with PTSC technology and located in UAE [93,94]. The simulated configurations are quite different than Shams 1. However, the simulated results will give a comparative analysis between the two technologies. The comparative analysis between the simulated result and the literature (Shams 1) will be illustrated in Table 32. It can be seen from Table 32 that Shams1 has a higher power output once it is compared to the simulated results. Consequently, the presented literature results can be comparatively analysed with the simulated configuration in certain aspects. It can be observed that CAES_ABHGT has the highest annual solar share with 87% at total capital cost of 234.8 (Mil USD) whereas Shams1 has an annual solar share of 75% at total capital cost of (350 Mil USD) .Moreover, It can be noticed at higher annual solar shares that the annual CO_2 emission avoided is increasing since less fuel content is used at the power plant.

Table 32: Comparative analysis with literature

Parameters	**Shams1[93]**	**HGT**	**ABHGT**	**CAES_ HGT**	**CAES_ ABHGT**
Power output (MW)	100	47	57	46	56
Integrated CSP technology	PTSC	PTSC	PTSC	PTSC	PTSC
Cycle configuration	Rankine	Brayton	Brayton	Brayton	Brayton
Heat transfer fluid	Oil	Air	Air	Air	Air
Annual solar share (%)	75%	20%	22%	85%	87%
Solar aperture Area(m^2)	627840	125000	127000	500000	508000
Annual operating Hours (Hrs)	2200	5475	5475	6570	6570
Annual CO_2 emission Avoided (tonne)	175000	20198	30742	117858	143481
Total Capital Cost (Mil USD)	350	66	100.5	272.6	234.8
Plant lifetime (Years)	30	25	25	25	25
LCOE (USD/MWh)	53	65.3	58.3	105.4	94.5

It can be observed that Shams1 has the lowest annual operating hours since its running only at daytime whereas the simulated CAES_ABHGT can be operated at flexible timings. Reducing the CO_2 emissions is one of the main objectives in the current thesis. The specific of CO_2 amount per unit of electricity emitted by the plant $\left(f_{CO_2}\right)$ is one of the key factors of the environmental indicators. Thus, reducing the CO_2 emission means less reliance on fossil fuels that have a large impact on climate change. Therefore, adding the advanced adiabatic CAES technology leads to an increase in the annual solar share and a large reduction in the CO_2 emissions.

Chapter 5. Conclusion and Recommendations

5.1. Conclusion

In this thesis, four different hybrid configurations of power plants are proposed. The first configuration is the hybrid gas-turbine power plant (HGT). In the second configuration, air-based bottoming cycle of hybrid gas turbine power plant is proposed to find the most optimum configuration with its corresponding optimal values to be implemented in the UAE. In the third configuration, the simple hybrid gas turbine cycle with advanced adiabatic compressed air energy storage (CAES_HGT) is introduced. In the fourth and final configuration, the model of the gas turbine using low temperature intercooled recuperated air bottoming cycle with advanced compressed air energy storage (CAES_ABHGT) is proposed. Initially, to be able to apply comparative thermo-economic and environmental optimization on HGT, ABHGT, CAES_HGT and CAES_ABHGT, nominal parameter selection and steady state results are illustrated at the beginning.

The steady state analyses are done through MATLAB and EES. It can be noticed that the main difference between HGT and ABHGT plants is adding a bottoming cycle. HGT is therefore conceptually the same plant as ABHGT but without its bottoming cycle. In order to know the accuracy of the simulated steady-state model of the power plant, the simulation results of HGT power plant without solar are compared with siemens gas turbine plant. Specifications and results of the HGT model without solar power are compared with Siemens SGT-800 and SGT-A45. These analyses are done under ISO conditions. HGT without solar power is analyzed by utilizing data of SGT-800 and SGT-A45 with the simulated MATLAB model. The results of the simulated model show a relative accurate analysis whilst comparing it with SGT-800 and SGT-A45. Power output is highly accurate with relative error of (1%).

Furthermore, the energy efficiency of the model has an acceptable relative inaccuracy of (2 %). Moreover, transient analysis is done to account for the change in solar radiation reaching the parabolic trough solar collector and account for the heat variation that is supplied to the gas turbine plant. To be able to simulate and account for the off-design condition that changes with time, a dynamic model is needed. This

Transient simulation is adopted with a meteorological year of Abu Dhabi. The Transient analyses are done through TRNSYS and MATLAB to account for parameters that change with time. The gas turbine power plants are operating from 6:30 am till 9:30 pm and turned off from 9:30 pm to 6:30 am.

An optimization convergence is needed to allocate the optimal design variables and parameters of the optimization problem. The power plant performance indicator results are illustrated, and a unified indicator is assigned to obtain an optimum configuration that satisfies the optimization problem. The multi objective algorithm method that is used in this project is the Pareto optimal front method. The advantages of using this method as it gives clear sign of the trade-off curve between the objective functions in the objective space. Using Pareto optimal front method on HGT and ABHGT power plants would illustrate a clear indication of the trade-off curve between the total capital cost and the cost of CO_2 emissions. The optimum solar shares for HGT and ABHGT are 20% and 22%, respectively. The LCOE of ABHGT and HGT are 58.35 (USD/MW) and 65.37(USD/MW) respectively. Both of the power plants have a positive NPV, where the NPV of HGT and ABHGT is 103.9 (Mil USD) and 151.8 (Mil USD) correspondingly. This is due to the fact that the fuel cost in UAE is cheap enough to make the investment profitable. The Specific CO_2 emissions of ABHGT is 22% lower than HGT. Reducing the CO_2 emissions is one of the main objectives in the current thesis. The specific of $\mathrm{CO_2}$ amount per unit of electricity emitted by the plant $\left(f_{CO_2}\right)$ is one of the key factors to the environmental indicators. Thus, reducing the CO_2 emission means less reliance on fossil fuel that has a large impact on climate change.

Sensitivity analysis is used to study the economic behavior of the power plant by varying the economic parameters to a certain extent. The sensitivity analysis is applied to ABHGT power plant to study its economic value and indicate the most sensitive parameters that have dominant effects on the economic analyses. Accordingly, LCOE and NPV are chosen as economic indicators for the sensitivity analysis. A uniform change in the economic parameters is implanted to analyze the effect on the economic performance indicators. One of the main problems that is facing the energy sector in the upcoming years is the risk of natural gas depletion. Among the high demand on natural gases these days, running the power plants with liquified petroleum gas (LPG) can be one of the promising alternative solutions to overcome the natural gas depletion threats. One of the main advantages of using LPG is its vast abundance due to the fact that LPG is mainly propane which can be chemically extracted. In fact, the lower heating value of LPG is lower than the natural gas where the lower heating value of LPG is about 46.6 (MJ/kg) while the natural gas is 50 (MJ/kg). Accordingly, to produce the same power output, more mass flow rate is needed for LPG to compensate for the difference in lower heating values. Moreover, LPG has more carbon content than natural gas. Therefore, it emits more specific CO_2 emissions than natural gas where LPG Specific CO_2 emissions (f_{CO_2}) is equal to 411 (Kg/MWh) and natural gas (f_{CO_2}) is equal to 351.5 (Kg/MWh).Additionally, it can be noticed that natural gas cost is cheaper than LPG by 5 USD /MWh. Consequently, annualized fuel cost of natural gas is cheaper by 8.8 (USD/MWh). Furthermore, ABHGT running with LPG will have a decrease on NPV by 32 (Mil US $). Although the natural gas is cheaper than LPG, it is not recommended to be used in the upcoming years due to the depletion effect. LPG will be more feasible in the future since it can be chemically extracted.

Moreover, the addition of advanced adiabatic CAES to ABHGT and HGT models increases the solar share. An advanced adiabatic CAES is integrated with power plants to enhance the annual optimal solar share with reasonable LCOE. Moreover, the additional annualized capital cost of bottoming cycle of ABHGT is remunerated by the annualized fuel cost reduction at the topping cycle. The performance of (CAES_ABHGT) is evaluated at 1, 3 and 7.5 hours of storage capacity. Thus, it can be seen that Mode C with a 7.5 hour storage capacity is the most promising model since it has the highest optimal annual solar share of 87% with reasonable LCOE of 94.5 (USD/MWh) and a reduction of CO_2 emissions by 83 %. Reducing the CO_2 emissions is one of the main objectives in the current thesis which is achieved at the end by the addition of compressed air energy storage. It can be noticed that the main share contribution to the LCOE for CAES _ABHGT and CAES_HGT is the annualized capital cost where the LCOE for the two model without thermal storage depends mainly on fuel. Moreover, the annualized fuel cost is not a major contributor anymore since the power plants depend more on the annual solar share. The annualized capital cost and fuel cost of CAES_ABHGT are 70.9 (USD/MWh) and 4 (USD/MWh) whereas the annualized capital cost and fuel cost of HGT are 79.8 (USD/MWh) and 7.15 (USD/MWh) respectively.

5.2. Recommendations

The proposed four power plants are flexible on different operating modes since they are hybrid power plants. So, running the system with latent thermal storages can be studied and compared with the sensible thermal storage systems. Additionally, Steam turbine power plants can be added and compared with the gas turbine power plant to evaluate the plants' performances and their drawbacks. Moreover, different CSP technologies such as heliostat field collector can be used to study the performance of the power plant. Different heat transfer fluids (HTF) can be studied to allocate the optimum heat transfer fluid for thermal storage. Furthermore, an experimental study can be implemented for a prototype system of 10 kW output with a thermal energy storage to validate the simulation results.

References

[1] M.Saghafifar. "Thermo-economic optimization of hybrid solar Maisotsenko bottoming cycles using heliostat field collector" M.Sc. thesis, American University of Sharjah, UAE, 2016.

[2] J. Spelling. "Hybrid Solar Gas-Turbine Power Plants*,"* *Thermoeconomic Analysis*. vol. 36, pp. 8-40, 2013.

[3] A. Alashkar. "Evaluation of an Integrated PTSC/Thermal Energy Storage System Using Nano-fluid particles." M.Sc. thesis, American University of Sharjah, UAE, 2016.

[4] D. Barlev and R. Vidu. "Innovation in Concentrated Solar Power." Solar Energy Materials and Solar power, vol. 95, no. 10, pp. 2705-2721, 2011.

[5] A. F. Ghoniem. " Hybrid Power Cycle: Performance Analysis and Comparison to Steam Redox Reforming," *International Journal of Energy,* vol. 40, no. 7, pp. 2970-2988, 2015.

[6] Z. Abbas. "Renewable Energy Policy Options for Abu Dhabi: Drivers and Barriers," *Energy Policy*, vol. 42, pp. 328-335, 2012.

[7] A. Kalogirou. "Parabolic Trough Collectors for Industrial Process Heat in Cyprus," *Energy*, vol. 27, no. 9, pp. 813-830, 2002.

[8] E. J. Sheu and A. F. Ghoniem. " Redox Reforming Based, Integrated Solar-Natural Gas Plants: Reforming and Thermodynamic Cycle Efficiency," *International Journal of Hydrogen Energy*, vol. 39, no. 27, pp. 1417-14833, 2014.

[9] E. J. Sheu, E. M. Mokheimer and A. F. Ghoniem. " Dry Redox Reforming Hybrid Power Cycle: Performance Analysis and Comparison to Steam Redox Reforming," *International Journal of Hydrogen Energy*, vol. 40, no. 7, pp. 2939-2949, 2015.

[10] D. Samulewicz and Y. Al-Saleh. "An Empirical Examination of the Development of a Solar Innovation System at the United Arab Emirates," *Energy for Sustainable Development*, vol. 16, no. 2, pp. 179-198, 2012.

[11] A. Poullikkas. "An Overview of Current and Future Sustainable Gas Turbine Technologies," *Renewable & Sustainable Energy Reviews*, vol. 9, pp. 409-443, 2005.

[12] A. F. Ghoniem. "Allocating electricity production from a hybrid fossil-renewable power plant among its multi primary resources," Energy, vol. 60, pp. 367-385, 2013.

[13] F. Khaldi. "Air Bottoming Cycle for Hybrid Solar-Gas Power Plants," *Proc. World Renew. Energy Congr. – Sweden, 8–13 May, 2011, Linköping, Sweden*, vol. 57, no. November 2011, pp. 3813–3820, 2011.

[14] K. Gairaa and S. Benkaciali. "Analysis of Solar Radiation Measurements at Ghardaia Area, South Algeria," *Energy Procedia*, vol. 6, pp. 122-129, 2011.

[15] M. A. Boles. *Thermodynamics: Engineering Approach.* New York, USA: McGraw-Hill, 2007, pp. 100-198.

[16] W. Farrell. "Air cycle thermodynamic conversion." New York, USA. U.S. patent 4.751.814A, 1988.

[17] T. Chmielniak, D. Czaja and S. Lepszy. "Thermal and economic analysis of the gas turbine air bottoming cycle," *in ASME Turbo Expo*, Copenhagen, 2012, pp. 100-198.

[18] J. Sathaye. "Renewable Energy in the Context of Sustainable Development," *Renewable Energy Sources and Climate Change Mitigation*, vol. 9, pp. 705-793, 2009.

[19] S. Lepszy. "Selection of Gas Turbine Air Bottoming Cycle for Polish Compressor Stations," *Journal of Power Technologies*, vol. 93, no. 2, pp. 63-79, 2013.

[20] H. U. Frutschi. "Closed-cycle gas turbines: operating experience and future potential," *New York: ASME Press*, 2005, pp. 70-120.

[21] A. Cabane. Fernandez. “Economic Study of Solar Thermal Plant based on Gas Turbines," M.Sc. thesis, LTH School of Engineering, Lund University, Lund, 2013.
[22] R. Goic. "A Review of Renewable Energy-Based Cogeneration Technologies," *Renewable and Sustainable Energy Reviews*, vol. 15, no. 8, pp. 3630-3654, 2011.
[23] F. Khaldi. "Air bottoming cycle solar-gas power plants," *World Renewable Energy Congress*, Sweden, 2011, pp. 70-150.
[24] H. Esen, M. Inalli and M. Esen. "Technoeconomic Appraisal Of A Ground Source Heat Pump System For A Heating Season In Eastern Turkey," *Energy Conversion and Management*, vol. 47, no. 9, pp. 1281-1297, 2006.
[25] S. Kuravi, J. Trahan, D. Goswami, M. Rahman and E. Stefanakos. “Thermal Energy Storage Technologies and Systems for Concentrating Solar Power Plants,” *Progress in Energy and Combustion Science*, vol. 39, no. 4, pp. 285-319, 2013.
[26] W. L. Gallo. "A Comparison Between the HAT Cycle and Other Gas-Turbine Based Cycles: Efficiency, Specific Power and Water Consumption," *Energy Conversion and Management*, vol. 38, no. 15, pp. 1595-1604, 1997.
[27] H. Rahmanifard. “Techno-Economic Assessment of CAES Technologies in Enhanced Geothermal Systems (EGS),” M.Sc. thesis, University of Calgary, Canada, 2018.
[28] T. Chmielniak, D. Czaja, S. Lepszy, and K. Stepczyńska-Drygas. “Thermodynamic and Economic Comparative Analysis of Air And Steam Bottoming Cycle,” *Energy*, vol. 92, pp. 189–196, 2015.
[29] M. Saghafifar, A. Omar, S. Erfanmoghaddam, and M. Gadalla. “Thermo-Economic Analysis of Recuperated Maisotsenko Bottoming Cycle Using Triplex Air Saturator: Comparative Analyses,” *Applied Thermal Engineering* , vol. 111, pp. 431–444, 2017.
[30] D. W. Keith. "Compressed Air Energy Storage with Waste Heat Export: an Alberta Case Study," *Energy Conversion and Management*, vol. 78, pp. 118-134, 2014.
[31] M. Ohadi and A. Alili. "Measurement of Solar Energy Radiation in Abu Dhabi, UAE,” *Applied Energy*, vol. 86, no. 4, pp. 511-515, 2009.
[32] M. Mecibah. "Parabolic Trough Solar Thermal Power Plant: Potential, And Projects Development in Algeria," *Renewable and Sustainable Energy Reviews*, vol. 21, pp. 290-297, 2013.
[33] M. Soltani and G. Valizadeh. "Technical and Economic Assessment of the Integrated Solar Combined Cycle Power Plants in Iran," *Renewable Energy*, vol. 30, no. 10, pp. 1541-1555, 2005.
[34] E. Bellos, C. Tzivanidis, and K. A. Antonopoulos. “A Detailed Working Fluid Investigation for Solar Parabolic Trough Collectors,” *Applied Thermal Engineering*, vol. 114, no. November 2016, pp. 374–386, 2017.
[35] A. Faghri. "Analysis of Thermal Energy Storage System with Conjugate Turbulence Forced Convection," *Journal of Thermophysics and Heat Transfer*, vol. 9, no. 4, pp. 722-726, 1995.
[36] J. Marin, L. Cabeza and H. Mehling. "Review on Thermal Energy Storage with Phase Change: Materials, Heat Transfer Analysis and Applications," *Applied Thermal Engineering*, vol. 23, no. 3, pp. 255-283, 2003.
[37] M. Passandideh-fard and M. Mousavi. "Two New High-Performance Cycles for Gas Turbine with Air Bottoming," *Energy*, vol. 32, pp. 294-304, 2011.
[38] M. Ahmad. "Optimization of Tilt Angle for Solar Collector to Receive Maximum Radiation," *The Open Renewable Energy Journal*, vol. 2, no. 1, pp. 20-27, 2009.
[39] M. Jonsson and J. Yan. "Humidified Gas Turbines—a Review of Proposed and Implemented Cycles," *Energy*, vol. 30, no. 7, pp. 1013-1078, 2005.

[40] A. R. Kovscek. "Solar-Generated Steam for Oil Recovery: Reservoir Simulation, Economic Analysis, and Life Cycle Assessment," *Energy Conversion and Management*, vol. 77, pp. 729-736, 2014.
[41] M. Shakeri and R. Ghorbani. "Investigating of Helmholtz wave energy converter," *Renewable Energy*, vol. 87, pp. 68-75, 2016.
[42] O. Ifedayo. "Determination of Optimum Tilt Angles for Solar Collectors in Low-Latitude Tropical Region," *International Journal of Energy Environment Eng*ineering, vol. 4, no. 1, p. 35, 2013.
[43] R. Padilla, G. Demirkaya, D. Goswami, E. Stefanakos and M. Rahman. "Heat Transfer Analysis of Parabolic Trough Solar Receiver," *Applied Energy*, vol. 88, no. 12, pp. 5097-5110, 2011.
[44] D. Goswami, E. Stefanakos and M. Rahman. " Heat Transfer Analysis of Parabolic Trough Solar Receiver, " *Applied Energy*, vol. 88, no. 12, pp. 5097-5110, 2011.
[45] K. Matrawy and J. Yassin. "Modelling and performance prediction of a solar powered rankine cycle/gas turbine cycle," *Challenges of Power Engineering and Environment*, 2007, pp. 103-107.
[46] H. Al-Ansary and O. Zeitoun, "Numerical Study of Conduction and Convection Heat Losses from a Half-Insulated Air-Filled Annulus of the Receiver of a Parabolic Trough Collector," *Solar Energy*, vol. 85, no. 11, pp. 3036-3045, 2011.
[47] E. J. Hu. "A Medium-Temperature Solar Thermal Power System and its Efficiency Optimisation," *Applied Thermal Engineering*, vol. 22, no. 4, pp. 357-364, 2002.
[48] M. Besarati and D. Y. Goswami. "A Computationally Efficient Method for the Design of the Heliostat Field for Solar Power Tower Plant," *Renewable Energy*, vol. 69, pp. 226-232, 2014.
[49] K. Shirai. "Reduction of heat loss from solar thermal collector by diminishing natural convection with high-porosity porous medium," *Solar Energy*, vol. 97, pp. 308-315, 2013.
[50] S. F. Wu. "Studies of the Direct Input of Solar Energy to a Fossil Central Station Steam Power Plant," *Solar Energy*, vol. 17, no. 5, pp. 298-308, 1975.
[51] M. Esen. "Technoeconomic Appraisal of a Ground Source Heat Pump System for a Heating Season In Eastern Turkey," *Energy Conversion and Management*, vol. 47, no. 9, pp. 1285-1297, 2006.
[52] B. R. Pai. "Augmentation of Thermal Power Stations with Solar Energy," *Sadhana*, vol. 16, no. 1, pp. 59-74, 1991.
[53] P. Schwarzbözl and F. Tellez. "Solar-Hybrid Gas Turbine-Based Power Tower Systems," *Journal of Solar Energy Engineering*, vol. 124, no. 1, pp. 6-9, 2002.
[54] Z. W. Z. Yao, Z. Lu and X. Wei. "Modeling and Simulation of the Pioneer 1MW Solar Thermal Central Receiver System in China," *Renewable Energy*, vol. 34, no. 11, pp. 2437-2446, 2009.
[55] J. E. Pacheco, H. E. Reilly, J. Gregory and C. E. Tyner. "Summary of the solar two: test and evaluation program," *SAND2000-0372C*, 2000, pp.1-13.
[56] J. Walker and J. Pittman."Overview of the Turbine Based Combined Cycle Discipline," *Ntrs.nasa.gov*,2009. [Online]. Available: http://ntrs.nasa.gov/search.jsp?R=20110012002. [Accessed: 16- Jun- 2017].
[57] J. Adeoye, Y. Amha, V. Poghosyan, K. Torchyan and H. Arafat. "Comparative LCA of Two Thermal Energy Storage Systems for Shams1 Concentrated Solar Power Plant: Molten Salt vs. Concrete," *Journal of Clean Energy Technologies*, vol. 2, pp. 274-281, 2014.

[58] F. J. Collado and J. Guallar. "A Review of Optimized Design Layouts for Solar Power Tower Plants with Campo Code," *Renewable and Sustainable Energy Reviews*, vol. 20, pp. 142-154, 2013.
[59] D. A. Sunter and V. P. Carey. "A Thermodynamic Similarity Framework for Assessment of Working Fluids for Solar Rankine Power Generation," *Journal of Solar Energy Engineering*, vol. 132, no. 4, pp. 410051-410058, 2010.
[60] O. Zeitoun. "Numerical Study of Conduction and Convection Heat Losses from a Half-Insulated Air-Filled Annulus of the Receiver of a Parabolic Trough Collector," *Solar Energy*, vol. 85, no. 11, pp. 3039-3045, 2011.
[61] J. Feldhoff, K. Schmitz, M. Eck, L. Schnatbaum-Laumann, D. Laing, F. Ortiz-Vives and J. Schulte-Fischedick. "Comparative System Analysis of Direct Steam Generation and Synthetic Oil Parabolic Trough Power Plants with Integrated Thermal Storage", *Solar Energy*, vol. 86, no. 1, pp. 520-530, 2012.
[62] S. C. Kaushik, V. S. Reddy and S. K. Tyagi. "Energy and Exergy Analyses of Thermal Power Plants," *Renewable and Sustainable Energy Reviews,* vol. 15, no. 4, pp. 1857-1872, 2011.
[63] A. Hepbasli. "A key Review on Exergetic Analysis and Assessment of Renewable Energy Resources for a Sustainable Future," *Renewable and Sustainable Energy Reviews*, vol. 12, no. 3, pp. 593-661, 2008.
[64] Solarintegrationworkshop.org. "Solar Integration Workshop - SIW 2015," 2015. [Online]. Available: http://www.solarintegrationworkshop.org/brussels2015/. [Accessed: 24- jun- 2018].
[65] G. B. Leyland. "Multi-Objective Optimization Applied to Industrial Energy Problems", EPFL Thesis, LENI, Lausanne, 2002.
[66] V. Modi. "Penetration of solar power without storage," *Energy Policy*, vol. 37, no. 11, pp. 4735-4738, 2009.
[67] L. V. Griffith and H. Brandt. "Solar-Fossil Hybrid System Analysis: Performance and Economics," *Solar Energy*, vol. 33, no. 3, pp. 265-276, 1984.
[68] V. Poghosyan, K. Torchyan and H. Arafat. "Comparative LCA of Two Thermal Energy Storage Systems for Shams1 Concentrated Solar Power Plant: Molten Salt vs. Concrete," *Journal of Clean Energy Technologies*, vol. 2, pp. 274-281, 2014.
[69] R. Madlener. "Cost-Effective Design of Ringwall Storage Hybrid Power Plants:Real Options Analysis," *Energy Conversion and Management*, vol. 103, pp. 871-885, 2015.
[70] Siemens Energy Sector. "SGT-800 Industrial Gas Turbine Gas Turbines Manufacturer Global." Germany, 2013.
Available: https://new.siemens.com/global/en/products/energy/power-generation/gas turbines/sgt-800.html#content=Technical Data (accessed Jul. 16, 2019).
[71] A. H. Slocum, D. S. Codd, J. Buongiorno, C. Forsberg, T. McKrell, J. Nave. "Concentrated Solar Power on Demand," *Solar Energy*, vol. 85, no. 7, pp. 1519-1529, 2011.
[72] Y. Hao, C.-K. Yang and S. M. Haile. "High-Temperature Isothermal Chemical Cycling for Solar-Driven Fuel Production," *Physical Chemistry Chemical Physics,* vol. 15, no. 40, pp. 17084-17092, 2013.
[73] U. Freschi. "Closed-cycle gas turbines: operating experience and future potential," New York, *ASME Press*, 2005, pp. 10-120.
[74] M. Badger and I. Karagali. "Satellite Winds as a Tool for Offshore Wind Resource Assessment: The Great Lakes Wind Atlas," *Remote Sensing of Environment*, vol. 168, pp. 345-369, 2015.

[75] Kolb. “Economic Evaluation of Solar-Only and Hybrid Power Towers Using Molten-Salt Technology," *Solar Energy*, vol. 62, no. 1, pp. 57-61, 1998.
[76] W. Pu and W. He. "Comparative Analysis of a Bottoming Cycle," *Energy Conversion and Management,* vol. 89, p. 764–774, 2015.
[77] U. Hellwig. "Concentrated Solar Power Hybrid Plants, Which Technologies are Best Suited for Hybridisation," *Renewable Energy,* vol. 57, pp. 536-562, 2013.
[78] M. Yaghoubi. "Exergy Analysis of an Integrated Solar Combined Cycle System," *Renewable Energy*, vol. 35, no. 10, pp. 2159-2161, 2010.
[79] B. Gray. " The Planet with Solar Fuel," *Nature Chemistry,* vol. 1, no. 1, pp. 202-250, 2009.
[80] M. Wietschel. "The Future of Hydrogen - Opportunities and Challenges," *International Journal of Hydrogen Energy*, vol. 34, no. 2, pp. 617-637, 2009.
[81] Y. Wang and Z. Wang. "Thermal Analysis and Design of Solid Energy Storage," *Applied Thermal Engineering*, vol. 75, pp. 216-223, 2015.
[82] R. J. Thomas, R. A. Ellison, K. M. Goodenough, N. M. W. Roberts, and P. A. Allen. “Salt Domes of the UAE and Oman: Probing eastern Arabia,” *Precambrian Research,* vol. 256, no. December 2017, pp. 1–16, 2015.
[83] M. Saghafifar, K. Mohammadi, and K. Powell. “Design and analysis of a dual-receiver direct steam generator solar power tower plant with a flexible heliostat field,” *Sustainable Energy Technology Assessments*, vol. 39, no. March, p. 100698, 2020.
[84] P. Johnson. “Assessment of compressed air energy storage system,” *Mechanical Engineering*, vol. 2, pp. 83-110, 2014.
[85] K. Rashid, S. M. Safdarnejad, K. Ellingwood, and K. M. Powell. “Techno-Economic Evaluation of Different Hybridization Schemes for a Solar Thermal/Gas Power Plant,” *Energy*, vol. 181, pp. 91–106, 2019.
[86] K. Ellingwood, K. Mohammadi, and K. Powell. “A novel means to flexibly operate a hybrid concentrated solar power plant and improve operation during non-ideal direct normal irradiation conditions,” *Energy Conversion and Management*, vol. 203, p. 112275, 2020.
[87] K. Mohammadi and J. G. McGowan. “Thermodynamic Analysis of Hybrid Cycles Based on a Regenerative Steam Rankine Cycle for Cogeneration and Trigeneration,” *Energy Conversion and Management*, vol. 158, pp. 460–475, 2018.
[88] S. Adibhatla and S. C. Kaushik. “Exergy and Thermoeconomic Analyses of 500mwe Sub Critical Thermal Power Plant with Solar Aided Feed Water Heating,” *Applied Thermal Engineering*, vol. 123, pp. 340–352, 2017.
[89] K. Mohammadi and H. Khorasanizadeh. “The Potential and Deployment Viability Of Concentrated Solar Power (CSP) In Iran,” *Energy Strategy Reviews*, vol. 24, pp. 358–369, 2019.
[90] M. Saghafifar and S. Gabra. “A Critical Overview of Solar Assisted Carbon Capture Systems: Is Solar Always the Solution?,” *International Journal of Greenhouse Gas Control*, vol. 92, p. 102852, 2020.
[91] Y. Liu, S. Deng, R. Zhao, J. He, and L. Zhao. “Energy-Saving Pathway Exploration of CCS Integrated with Solar Energy: A Review of Innovative Concepts,” *Renewable and Sustainable Energy Reviews*, vol. 77, pp. 652–669, 2017.
[92] S. Houssainy. “Hybrid Thermal and Compressed Air Energy Storage System (HT-CAES): Thermodynamic Analysis and Thermoeconomic Optimization.” PhD. thesis, University of California, USA, 2017.

[93] T. Mezher, D. Goldsmith and N. Choucri. "Renewable Energy in Abu Dhabi: Opportunities and Challenges," *Journal of Energy Engineering*, vol. 137, no. 4, pp. 169-176, 2011.

[94] V. Poghosyan and M. I. Hassan. "Techno-Economic Assessment of Substituting Natural Gas Based Heater with Thermal Energy Storage System in Parabolic Trough Concentrated Solar Power Plant," *Renewable Energy*, vol. 75, pp. 152-164, 2015.

Appendix A

Appendix A is used to calculate the steady state analysis of ABHGT model using MATLAB.

Matlab scribt for steady state

```
TTti=1673; %%%Inlet tempreture of top Turbin  in Kelvin%%%
TTto=848;  %%%outlet tempreture of top Turbin in Kelvin%%%
TTbi=798;  %%%Inlet tempreture of bottom Turbin in Kelvin%%%
TTbo=523;  %%%outlet tempreture of bottom  Turbin in Kelvin%%%
TC1ti=300;  %%%Inlet tempreture of top compressor 1 in
Kelvin%%%
TC1to=723;  %%%Outlet tempreture of top compressor 1 in
Kelvin%%%
TC2bi=300;  %%%Inlet tempreture of bottom compressor 2 in
Kelvin%%%
TC2bo=373;  %%%Outlet tempreture of bottom  compressor 2 in
Kelvin%%%
TC3bi=323;  %%%Inlet tempreture of bottom compressor 3  in
Kelvin%%%
TC3bo=423;  %%%Outlet tempreture of bottom compressor 3 in
Kelvin%%%
Tref=298;  %%% Reference tempreture in Kelvin%%%
Ticc=1173; %%%Inlet tempreture of Combusion chamber in
Kelvin%%
T0cc=1673; %%%Outlet tempreture of Combusion chamber in
Kelvin%%
LHV1=50142; %%%%lower heating value for Ch4%%5
mdotair=134;  %%% air mass flow rate in kg/s%%%%
nt=0.85;    %%%Turbine efficency%%%
nc=0.85;     %%%Compressor  efficency%%%
ncc=0.98;   %%% Combusion chamber efficency %%%
nMG=0.98;    %%%% mechanical gen eff %%%%
nele=0.99;   %%%%Electiacal gen eff  %%%%%%
TTtavg=(TTti+TTto)/2
TTbavg=(TTbi+TTbo)/2
TC1tavg=(TC1ti+TC1to)/2
TC2bavg=(TC2bi+TC2bo)/2
TC3bavg=(TC3bi+TC3bo)/2
Cpavg1=1.165;         %%%FOR CH4 IN top Turbine Table A-2  %%%
cpavg2=1.164;         %%%for LPG IN top Turbine  Table A-2 %%%
Cpavg3=1.063;          %%%for air in bottom turbine  Table A-2
%%%
Cpavg4=1.030;          %%%for air in top compresser 1  A-2 %%%
Cpavg5=1.006;         %%%for air  in bottom compresser 2 Table
A-2 %%%
Cpavg6=1.010;         %%%for air in compresser 3 Table A-2 %%%
Cpair=1.142;         %%for air in Combusion chamber  Table A-2
%%%
Wtt=(Cpavg1*(TTti-TTto))/nt    % specefic work of top Turbin %
```

```
Wbt=(Cpavg3*(TTbi-TTbo))/nt     % specefic work of bottom
Turbin%
Wtc1=(Cpavg4*(TC1ti-TC1to))/nc % specefic work of top
comressor1 %
Wbc2=(Cpavg5*(TC2bi-TC2bo))/nc % specefic work of bottom
comressor 2 %
Wbc3=(Cpavg6*(TC3bi-TC3bo))/nc % specefic work of bottom
comressor 3 %
mdotfuel=((mdotair*Cpavg1*(T0cc-Tref))-(mdotair*Cpair*(Ticc-
Tref)))/((ncc*LHV1)-(Cpavg1*(T0cc-Tref)))
mdotg=mdotair+mdotfuel
Wdotnet=((nMG*((mdotg*Wtt)+(mdotair*Wbt)))+((mdotair*(Wtc1+Wbc
2+Wbc3))/(nMG)))  %to calculate the net power ouput of the
system
```

Appendix B

Appendix B is used to calculate the steady state analysis of PTSC using Engineering Equation Solver (EES) and obtain the required useful energy.

<u>EES script 1</u>

$Dro = 0.05$

$Dri = 0.04$

$Dco = 0.09$

$w = 10$

$L_{para} = 15$

$Ti = 723$

$Kr = 15$

$Tr = 260$

$Er = 0.92$

$EFFr = 0.75$

$Ec = 0.87$

$\sigma = 5.67 \cdot 10^{-8}$

$Tc = 64$

$Ts = 5770$

$Tamb = 42$

$v = 5$

$Id = 800$

$DENair = 1.1$

$Kair = 2.875 \cdot 10^{-5}$

$cpair = 1.08$

$Fr = 1$

$Qin = Ib \cdot Aa$

$$To = 1173$$

$$To = Ti + \frac{Qu}{1000 \cdot mair \cdot cpair}$$

$$Qu = Fr \cdot (Ib \cdot Aa - Ar \cdot Ul \cdot (Ti - Tamb - 273))$$

$$Aa = (w - Dco) \cdot L_{para}$$

$$Ar = \pi \cdot Dro \cdot L_{para}$$

$$Ib = Id \cdot EFFr$$

$$F = \frac{Uo}{Ul}$$

$$Ul = \left[\frac{Ar}{(Hcca + Hrca) \cdot Ac} + \frac{1}{Hrcr}\right]^{-1}$$

$$Ac = \pi \cdot Dco \cdot L_{para}$$

$$Hcca = \frac{Nusca \cdot Kair}{Dco}$$

$$Nusca = 0.4 + 0.54 \cdot Re^{0.6}$$

$$Re = DENair \cdot v \cdot \frac{Dco}{KINVISair}$$

$$Hrca = Ec \cdot \sigma \cdot (Tc + 273 + Tamb + 273) \cdot ((Tc + 273) \cdot (Tc + 273) + (Tamb + 273) \cdot (Tamb + 273))$$

$$Hrcr = \frac{\sigma \cdot (Tc + 273 + Tr + 273) \cdot ((Tc + 273) \cdot (Tc + 273) + (Tr + 273) \cdot (Tr + 273))}{\left[\frac{1}{Er} + \frac{Ar}{Ac}\right] \cdot \left[\frac{1}{Ec} - 1\right]}$$

$$Uo = \left[\left(\frac{1}{Ul} + \frac{Dro}{Hcrin \cdot Dri} + \frac{Dro}{2 \cdot Kr}\right) \cdot \ln\left(\frac{Dro}{Dri}\right)\right]^{-1}$$

$$Hcrin = \frac{Nusr \cdot Kr}{Dri}$$

$$Nusr = 0.023 \cdot Rer^{0.8} \cdot Prr^{0.4}$$

$$Vair = 3.482 \cdot 10^{-5}$$

$$KINVISair = 1.7 \cdot 10^{-5}$$

$$Rer = \frac{v \cdot Dri}{Vair}$$

$$EFFen = \frac{Qu}{Aa \cdot Ib}$$

$$N_{ptc} = \frac{134}{mair}$$

$$Qu_{total} = N_{ptc} \cdot Qu$$

$$power = mair \cdot cpair \cdot (To - Ti)$$

$$power_t = power \cdot N_{ptc}$$

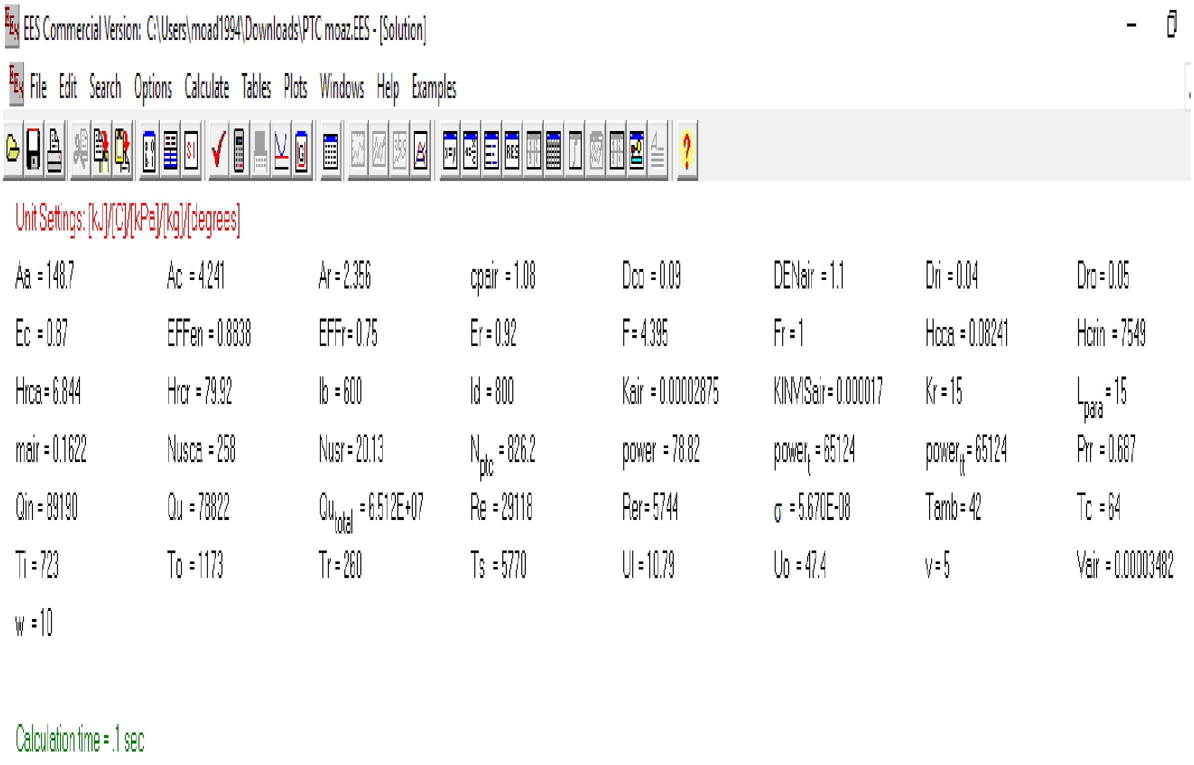
EES Commercial Version: C:\Users\moad1994\Downloads\PTC moaz.EES - [Solution]
File Edit Search Options Calculate Tables Plots Windows Help Examples
Unit Settings: [kJ]/[C]/[kPa]/[kg]/[degrees]
Aa = 148.7
Ac = 4.241
Ar = 2.356
cpair = 1.08
Dco = 0.09
DENair = 1.1
Dri = 0.04
Dro = 0.05
Ec = 0.87
EFFen = 0.8838
EFFr = 0.75
Er = 0.92
F = 4.395
Fr = 1
Hcca = 0.08241
Hcrin = 7549
Hrca = 6.844
Hrcr = 79.92
Ib = 600
Id = 800
Kair = 0.00002875
KINVISair = 0.000017
Kr = 15
Lpara = 15
mair = 0.1622
Nusca = 258
Nusr = 20.13
Nptc = 826.2
power = 78.82
powert = 65124
powertt = 65124
Prr = 0.687
Qin = 89190
Qu = 78822
Qutotal = 6.512E+07
Re = 29118
Rer = 5744
σ = 5.670E-08
Tamb = 42
Tc = 64
Ti = 723
To = 1173
Tr = 260
Ts = 5770
Ul = 10.79
Uo = 47.4
v = 5
Vair = 0.00003482
w = 10
Calculation time = .1 sec

EES script 2

```
T[1]=27+273
T[2]=450+273
T[3]=900+273
T[4]=1400+273
T[5]=575+273
T[6]=300+273
T[7]=27+273
T[8]=100+273
T[9]=50+273
T[10]=150+273
T[11]=525+273
T[12]=250+273
s[1]=6.830
s[2]=6.900
s[3]=7.500
s[4]=7.900
s[5]=7.850
s[6]=7.400
s[7]=7.350
s[8]=7.370
s[9]=7.150
s[10]=7.170
s[11]=7.840
s[12]=7.950
P[1]=PRESSURE(Air,T=T[1],s=s[1])
P[2]=PRESSURE(Air,T=T[2],s=s[2])
P[3]=PRESSURE(Air,T=T[3],s=s[3])
P[4]=PRESSURE(Air,T=T[4],s=s[4])
P[5]=PRESSURE(Air,T=T[5],s=s[5])
P[6]=PRESSURE(Air,T=T[6],s=s[6])
P[7]=PRESSURE(Air,T=T[7],s=s[7])
P[8]=PRESSURE(Air,T=T[8],s=s[8])
P[9]=PRESSURE(Air,T=T[9],s=s[9])
P[10]=PRESSURE(Air,T=T[10],s=s[10])
P[11]=PRESSURE(Air,T=T[11],s=s[11])
P[12]=PRESSURE(Air,T=T[12],s=s[12])
h[1]=ENTHALPY(Air,T=T[1])
h[2]=ENTHALPY(Air,T=T[2])
h[3]=ENTHALPY(Air,T=T[3])
h[4]=ENTHALPY(Air,T=T[4])
h[5]=ENTHALPY(Air,T=T[5])
h[6]=ENTHALPY(Air,T=T[6])
h[7]=ENTHALPY(Air,T=T[7])
h[8]=ENTHALPY(Air,T=T[8])
h[9]=ENTHALPY(Air,T=T[9])
h[10]=ENTHALPY(Air,T=T[10])
h[11]=ENTHALPY(Air,T=T[11])
h[12]=ENTHALPY(Air,T=T[12])
```

EES Commercial Version: C:\Users\moad1994\Desktop\thesis files\EES\Cycle data.EES - [Arr

File Edit Search Options Calculate Tables Plots Windows Help Examples

	1 P_i [kPa]	2 s_i [kJ/kg.K]	3 T_i [K]	4 h_i [kJ/kg]
[1]	1.988	6.83	300	300.4
[2]	36.5	6.9	723	738.1
[3]	30.07	7.5	1173	1246
[4]	32.88	7.9	1673	1846
[5]	2.449	7.85	848	875
[6]	2.705	7.4	573	578.8
[7]	0.3248	7.35	300	300.4
[8]	0.6506	7.37	373	374
[9]	0.8447	7.15	323	323.6
[10]	2.034	7.17	423	424.6
[11]	2.008	7.84	798	819.8
[12]	0.2862	7.95	523	526.9

Appendix C

Appendix C is used to validate my steady state analysis by comparing the steady state analyses with Siemens literature.

Power Generation	47.5 MW Version	50.5 MW Version
Simple Cycle		
Power output	ISO 47.5 MW(e)	ISO 50.5 MW(e)
Frequency	50/60 Hz	50/60 Hz
Electrical efficiency	37.7%	38.3%
Heat rate	9,557 kJ/kWh (9,058 Btu/kWh)	9,407 kJ/kWh (8,916 Btu/kWh)
Turbine speed	6,608 rpm	6,608 rpm
Compressor pressure ratio	20.4:1	21.1:1
Exhaust gas flow	132.8 kg/s (292.8 lb/s)	134.2 kg/s (295.8 lb/s)
Exhaust temperature	541 °C (1,006 °F)	553 °C (1,027 °F)
NO_x Emissions (with DLE, corrected to 15% O_2 dry)	≤ 15 ppmV	≤ 15 ppmV

Figure ***63***: Siemens gas turbine SGT 800 Performance

SGT-A45: Performance data for simple cycle power generation

	50 Hz, ISO conditions (15°C ambient)	50 Hz, hot climate (30°C ambient)	60 Hz, ISO conditions (15°C ambient)	60 Hz, hot climate (30°C ambient)
Power output	41.0 MW(e)	39.3 MW(e)	44.0 MW(e)	39.6 MW(e)
Fuel	Dual fuel (gas and liquid)			
Frequency	50 Hz	50 Hz	60 Hz	60 Hz
Electrical efficiency	38.9%	38.3%	40.4%	39.4%
Heat rate	9,260 kJ/kWh	9,405 kJ/kWh	8,944 kJ/kWh	9,137 kJ/kWh
Turbine speed	3,000 rpm	3,000 rpm	3,600 rpm	3,600 rpm
Pressure ratio	27.7 : 1	26.7 : 1	27.9 : 1	25.8 : 1
Exhaust mass flow	127 kg/s	120 kg/s	126 kg/s	116 kg/s
Exhaust temperature	477 °C (891 °F)	501 °C (934 °F)	483 °C (901 °F)	498 °C (928 °F)
NO_x emissions	≤ 15 ppmvd (gas fuel) / 42 ppvm (liquid fuel) with optional water injection			

Figure 64: Siemens gas turbine SGT-A45 Performance

Vita

Muad Mohamed Elgriw was born in 1994, in Tripoli, Libya. He received his primary and secondary education in Abu Dhabi, UAE. He received his B.Sc. degree in Mechanical engineering from American university of Sharjah in 2015. From 2015 to 2018, he worked as graduate teaching assistant at American university of Sharjah.

In September 2015, he joined the Mechanical engineering master’s program at the American University of Sharjah as a graduate teaching assistant. During his master's study, he published a conference paper and working on publishing two journal papers.